PhD Thesis

Magneto-optical and magnetic properties of two-dimensional materials

Fenda Rizky Pratama

Department of Physics, Graduate School of Science
Tohoku University

September 2021

Acknowledgments

I would like to use this opportunity to acknowledge all people whose direct supports have enable me to finish my doctor course and this thesis. First of all, I express my sincere gratitude to my supervisor Prof. R. Saito for his tutelage and guidance for the past five years. He educates me not only in scientific research, but also in many aspects of life as well. I am greatly indebted to Mr. M. Shoufie Ukhtary for his constant presence as a tutor in my study, and for his encouragement and countless help during difficult times. All of his kindness will remain in my memory as long as I live. I thank Dr. E. H. Hasdeo and Prof. A.R.T. Nugraha for various technical and mental supports. In particular, Dr. Hasdeo provided useful comments and suggestions during preparation of my thesis pre-defence. I thank fellow group members of Saito group: Prof. W. Izumida, Dr. N.T. Hung, Mr. T. Shirakura, Dr. Y. Tatsumi, Mr. K. Ghalamkari, Mr. Md. S. Islam, Mr. Y. Iwasaki, Mr. D. Sato, Mr. T. Shirosaki, Mr. M. Maruoka, Dr. S. Wang, Mr. T. Yuan, Ms. T. Wang, Ms. X. Pang, and Mr. T. Maeda for the time shared together and the sense of comradeship. I am grateful to Ms. J. Sasaki, Ms. Y. Wako, and Ms. N. Yamamoto for helping me to prepare many administrative documents, some of which are indispensable for my survival in Japan. I also thank my beloved mother and sister for their continuous care.

Last but not least, I address my gratitude to Tohoku University and Japanese Goverment (MEXT) for providing me a scholarship and a great experience of being a graduate student in Japan.

Abstract

The Faraday (Kerr) effect is a magneto-optical phenomenon in which polarization direction of a linearly-polarized incident light is rotated upon transmission through (reflection by) a material, in the presence of an external magnetic field parallel to the direction of propagation of the incident light. In a three-dimensional (3D) material, the magnitude of the Faraday rotation is proportional to thickness of the material and strength of the magnetic field. The origin of the Faraday effect in a 3D material is non-identical refraction indexes for left-handed and right-handed circularly polarized lights (which constitute a linearly-polarized light) when the magnetic field is applied. Because the reflection of light depends on the refractive index, the Kerr rotation is also generated. The discovery of graphene in 2004 have drawn researchers to investigate the Faraday and the Kerr effects in thin films and two-dimensional (2D) materials. A thin-film or a 2D material possesses a relatively large carrier density even though the thickness of the material is negligibly small (in the order of $10^{-6} - 10^{-9}$ m). In the 2D materials, the magnetic field generates the optical Hall conductivity which is proportional to the charge density, and gives rise to the Faraday and the Kerr rotations. The Faraday and the Kerr effects without magnetic field have been observed in a thin film topological insulator as a result of spin-orbit coupling and intrinsic magnetization. In particular, the spin-orbit coupling and intrinsic magnetization gives rise to the quantum anomalous Hall (QAH) state, where the Hall conductivity is quantized. However, a general description of the Faraday and the Kerr effects in 2D materials is not yet discussed. A general description of a 2D material in the QAH state is given by the Haldane model, which has been experimentally realized by using cold atoms in an optical lattice. Moreover, it is theoretically predicted that the Haldane model can be synthesized in the form of Fe-based ferromagnetic insulators in a honeycomb lattice, in which electrons in occupied bands are fully polarized in one spin direction owing to the strong Hund coupling in Fe. Therefore, it is meaningful to investigate the Faraday and the Kerr effects in the Haldane model, which is the first subject of this thesis.

The second subject of this thesis is orbital magnetization of graphene and the related 2D Dirac materials. It is known that undoped graphene possesses large diamagnetism, because in the presence of an external magnetic field, states of massless of electrons at the valence bands coalesce to the zeroth Landau level. As a result, the free energy of graphene increases with increasing magnetic field, which gives the orbital diamagnetism. Analytical formulas for orbital susceptibilities of graphene related materials, including monolayer transition-metal dichalcogenides and the Weyl semimetals, can be obtained by applying the Euler-Maclaurin formula in the calculation of thermodynamic potential. However, calculation of orbital magnetization with

the Euler-Maclaurin formula yields a divergent result. It is because we need to consider an infinite number of the Landau levels in the valence bands in the expression of the thermodynamic potential. Moreover, an experimental measurement of the orbital magnetization of graphene has been performed for wide ranges of magnetic field and temperature. Therefore, a method to derive analytical expression of magnetization of graphene is required to identify the origin of the magnetization behaviour for a given magnetic field and temperature.

The purposes of the thesis are: (1) to investigate the Faraday and the Kerr rotations in 2D materials without an external magnetic field in the Haldane model, and (2) to formulate analytical expressions for orbital magnetizations of graphene and related 2D materials, and thus to explain the origin of the dependences of magnetizations on the magnetic field and temperature.

In Chapter 2, we discuss calculation methods for the first purpose. Here, we derive energy dispersion of the Haldane model and optical conductivities of 2D material by using the linear response theory. The analytical formulas of absorption probability, as well as the angles of the Faraday and the Kerr rotations are derived by solving the Maxwell equations with boundary conditions at the 2D material.

In Chapter 3, we discuss calculation methods for the second purpose, in which we derive the Landau levels and thermodynamic potential of the 2D materials.

In Chapter 4, we derive analytical expressions for longitudinal and the Hall conductivities of the Haldane model, which are the origins of the Faraday and the Kerr rotations. Maximum Faraday and Kerr rotations are generated when the photon energy matches the energy band gap, due to the singularity in the real part of the Hall conductivity. Our treatment on the Faraday and the Kerr rotations is relevant to determine the topological phases in 2D materials. Moreover, our analytical formulas for optical conductivities can be applied to explain optical absorption of circularly-polarized lights in various 2D materials, such as silicene and monolayer transition-metal dichalcogenides.

In Chapter 5, we derive analytical expressions for orbital magnetizations of the 2D Dirac materials by using the zeta function to regularize infinite summation of the Landau levels. Our formula reproduces empirical fitting for orbital magnetization of undoped graphene in strong field/low temperature and weak field/high temperature limits. In the case of heavy Dirac fermions, we show that the magnetization is robust with respect to temperature and impurity scattering. Further, we demonstrate that the opening of band gap in the 2D materials can be detected from decreasing amplitude of the de Haas-van Alphen (dHvA) effect. Our results reproduce the experimental results without fitting procedure.

Contents

Chapter 1

Introduction

1.1 Purpose of study

The Faraday effect [1, 2, 3, 4] is a magneto-optical phenomenon in which polarization direction of light is rotated when the light propagates in a material, in the presence of an external magnetic field parallel to the propagation direction of light. For non-magnetic materials, the angle of Faraday rotation is proportional to thickness of the material and strength of the magnetic field. Similarly, rotation of the polarization direction also occurs for reflected light [1, 3], which is known as the Kerr effect. The first subject of this thesis is the Faraday and the Kerr effects for two-dimensional (2D) material, which does not have thickness.

The Faraday and the Kerr effects have been employed to analyse physical properties of materials (for examples band structure, density of states, charge mobility, effective mass of electron) and can also be applied in optical devices [4, 5, 6]. The Faraday and the Kerr rotations *without* magnetic field have been predicted [7] and observed [8] in a thin film topological insulators, as a result a large spin-orbit coupling and intrinsic magnetization. In particular, the interplay between the spin-orbit coupling and the intrinsic magnetization breaks time-reversal symmetry, and gives rise to the quantum anomalous Hall state [9, 10, 11, 12, 13], where σ_{xy} is integer multiple of e^2/h. In graphene-related materials, the Faraday and the Kerr rotations without magnetic field are predicted for bilayer graphene in the quantum anomalous Hall state [14, 15]. However, a general description of the Faraday and the Kerr effects in 2D materials without magnetic field is not yet discussed. A general description of a 2D material in the quantum Hall state is given by the Haldane model [16, 17, 18, 19, 20, 21], which has been experimentally realized by using cold atoms in an optical lattice [22]. Moreover, the Haldane model might be synthesized in a hexagonal ferromagnetic insulators [23]. Therefore, it is meaningful to investigate the Faraday and the Kerr effects in the Haldane model.

The second subject of this thesis is orbital magnetization of graphene and related 2D materials [24, 25, 26, 27, 28, 29, 30, 31, 32]. It is known that undoped graphene possesses large diamagnetism [24, 25, 30], because in the presence of an external magnetic field, electronic states of massless electrons at the valence band coalesce to the zeroth Landau level. As a result, the free energy of graphene increases with increasing magnetic field, which gives the orbital diamagnetism in graphene [24]. This explanation was first given by McClure [24] in 1956, who derived the analytical expression

for orbital susceptibility of graphene as a function of temperature and chemical potential. A method to derive the orbital susceptibility of graphene-related materials is developed by Koshino and Ando [33, 34]. In their method, the Euler-Maclaurin expansion formula is applied to calculate thermodynamic potential in the presence of magnetic field. The method has been employed to derive the orbital susceptibilities of gapped graphene [33, 34], monolayer transition-metal dichalcogenide [35], as well as the Weyl semimetal [36]. However, magnetization can not be obtained by using the Euler-Maclaurin expansion formula. It is because that the magnetization diverges due to an infinite number of the Landau levels formed in the valence bands that are included in the calculation of the thermodynamic potential.

The purposes of the thesis are: (1) to investigate the Faraday and the Kerr rotations in 2D materials without an external magnetic field in the Haldane model, and (2) to formulate analytical expressions for orbital magnetizations of graphene and related 2D materials, and thus to explain the origin of the dependences of magnetizations on magnetic field and temperature. For the first purpose, we derive optical conductivities of the Haldane with the linear response theory. In particular, we show that the material possesses an intrinsic, optical Hall conductivity when the time-reversal symmetry is broken. By solving the Maxwell equations with boundary conditions at the 2D material, we calculate the absorption probability in the Haldane model, as well as the angles for the Faraday and the Kerr rotations. For the second purpose, we adopt the method of the zeta function regularization [37] to obtain finite expressions of the thermodynamic potential and magnetization for the 2D materials. A classical example of the application of the zeta function regularization in physics is the formulation of the Casimir effect [38]. In the Casimir effect, the zeta function is used to regularize the infinite summation of vacuum energy levels between two parallel, perfectly conducting plates. As a result, an attractive force emerges between the plates. Since the Casimir force has been experimentally verified [39, 40, 41, 42], the zeta function regularization is thus physically justified for the Casimir effect.

1.2 Organization of thesis

In Section 1.3, we present some basic concepts for understanding the results of this thesis. For the first subject of the thesis, we begin by discussing the origin of the Faraday and the Kerr rotations in conventional 3D materials. Further, we introduce concepts of the Hall effect, anomalous Hall effect, quantum Hall effect, anomalous quantum Hall effect, in which materials possess a finite value of the Hall conductivity σ_{xy}, in the presence (or absence) of magnetic field. Next, we briefly describe the Haldane model which exhibits quantum anomalous Hall state. For the second subject, we discuss the Landau level formation in graphene, and basic concepts of magnetic responses, i.e. magnetization and susceptibility. Further, we also discuss the zeta function regularization in the Casimir effect. In Chapter 2, we discuss calculation methods for the first purpose. Here, we derive energy dispersion of the Haldane model and optical conductivities of 2D material by using the linear response theory. The analytical formulas of absorption probability, as well as the angles of the Faraday and the Kerr rotations are derived by solving the Maxwell equations with boundary conditions at the 2D material. In Chapter 3, we discuss calculation methods for the second purpose, in which we derive the Landau levels and thermodynamic potentials of 2D Dirac materials. In Chapter 4, results of the first purpose are given, which

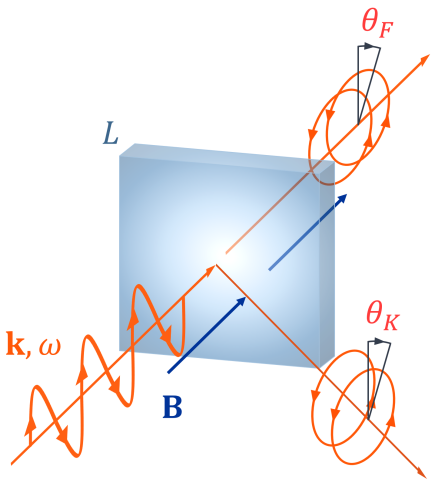

Figure 1.1 Schematic illustration of the Faraday and the Kerr effects, in which the angles of rotation for the transmitted and reflected lights are denoted by θ_F and θ_K, respectively. $\boldsymbol{k}$ and ω denote, respectively, wavevector and angular momentum of the incident light. The direction of magnetic field $\boldsymbol{B}$ is parallel to that of the incident light. Here, the transmitted and reflected lights become elliptically-polarized, because of circular dichroism.

include the analytical formulas for optical conductivities of the Haldane model, as well as the Faraday and the Kerr rotations in the Haldane model without magnetic field. In Chapter 4, we present the results of the second purpose. In Chapter 4, we present analytical expressions of magnetizations of the 2D Dirac materials as a function of magnetic field and temperature. In Chapter 6, we summarize and conclude our thesis.

1.3 Background

Here, we provide some basic concepts which are required to understand the contents of this thesis.

1.3.1 Faraday and Kerr effects

1.3.1.1 Faraday and Kerr effects in conventional 3D materials

The *Faraday (Kerr) effect* is a magneto-optical phenomenon where polarization direction of a linearly-polarized incident light is rotated upon transmission through (reflection by) a material, in the presence of an external magnetic field parallel to the direction of propagation of the incident light. A schematic illustration of the Faraday and the Kerr effects are depicted in Fig. 1.1. Hereafter, we denote the angle of rotation for the transmitted (reflected) light by θ_F (θ_K). It is noted that the transmitted and the reflected lights become elliptically polarized, too. The occurrence of ellipticity comes from *circular dichroism* (CD), that is the different optical absorption probabili-

Fig. 1.1: fig/ch1/faraday-kerr.eps

ties for left-handed and right-handed circularly-polarized (LCP and RCP, respectively) lights. The origin of the Farday and the Kerr effects will be explained shortly.

For non-magnetic materials, the angle of the Faraday rotation θ_F [1, 2] is given by

$$\theta_F = \mathcal{V}BL, \tag{1.1}$$

where B and L are the strength of the magnetic field and the thickness the material, respectively. The proportionality factor $\mathcal{V}$ is called the Verdet constant, which actually depends on temperature and wavelength of the light [1, 43]. In the terahertz (THz) regime, an example of material with a large Verdet constant is known for La:YIG (yttrium iron garnet), with $\mathcal{V} \approx 1745$ rad/(Tm) [44].

Let us discuss the origin of the Faraday effect by using arguments from the classical electrodynamics, and let us recall that a linearly-polarized light is a superposition of LCP and RCP lights with the same amplitudes. When we apply an external magnetic field $\boldsymbol{B}$, an electron with velocity $\boldsymbol{v}$ in the material experiences the Lorentz force from $\boldsymbol{B}$ and electric field $\boldsymbol{E}$ from light, as follows [1]:

$$\boldsymbol{F}_L = -e(\boldsymbol{E} + \boldsymbol{v} \times \boldsymbol{B}), \tag{1.2}$$

where e is the elementary charge. Here, we assume that the electron is bound by a restoring force from an atom, which keeps the electron around its original position $\boldsymbol{r}$ around the atomic nucleus. The restoring force can take the form of the Hooke law $\boldsymbol{F}_H = -k\boldsymbol{r}$, where k is a constant. Additionally, we also include a friction force $\boldsymbol{F}_\gamma = -\gamma m\boldsymbol{v}$, which is characterized by the damping constant γ. The total force acting on the electron is given by

$$\begin{aligned} m\frac{d^2\boldsymbol{r}}{dt^2} &= \boldsymbol{F}_H + \boldsymbol{F}_\gamma + \boldsymbol{F}_L \\ &= -k\boldsymbol{r} - \gamma m\frac{d\boldsymbol{r}}{dt} - e\Big(\boldsymbol{E} + \frac{d\boldsymbol{r}}{dt} \times \boldsymbol{B}\Big). \end{aligned} \tag{1.3}$$

Here, m is the effective mass of the electron. By assuming that the oscillation of electron follows the harmonic motion, $\boldsymbol{r} = \boldsymbol{r}_0 e^{-i\omega t}$ where ω is angular frequency of the light, we get

$$-m\omega^2\boldsymbol{r} = -k\boldsymbol{r} + i\gamma\omega m\boldsymbol{r} - e\boldsymbol{E} + ie\omega\boldsymbol{r} \times \boldsymbol{B}. \tag{1.4}$$

By expressing $\boldsymbol{r}_0 = x_0\hat{\boldsymbol{x}} + y_0\hat{\boldsymbol{y}}$, and set $\boldsymbol{B} = B\hat{\boldsymbol{z}}$, we obtain equation of motions in the x- and y-direction as follows:

$$\begin{cases} -m\omega^2 x = -kx + i\gamma\omega mx - eE_x + ie\omega yB \\ -m\omega^2 y = -ky + i\gamma\omega my - eE_y - ie\omega xB, \end{cases} \tag{1.5}$$

where $x = x_0 e^{-i\omega t}$ and where $y = y_0 e^{-i\omega t}$. A circularly-polarized light is given by $\boldsymbol{E} = (E/\sqrt{2})(\hat{\boldsymbol{x}} + i\hat{\sigma}\hat{\boldsymbol{y}}) = \boldsymbol{E}_x + \boldsymbol{E}_y$, where $\hat{\sigma}$ denotes helicity, and $\hat{\sigma} = +1$ (-1) for LCP (RCP) light (see Chapter 2 for more detail). Thus, we have the relation $E_y = i\hat{\sigma}E_x = i\hat{\sigma}E/\sqrt{2}$. Since the electron moves in the opposite direction to the electric field, we can write $x_0 = r_0/\sqrt{2}$ and $y_0 = -i\hat{\sigma}r_0/\sqrt{2}$. From Eq. (1.5), we get

$$\boldsymbol{r} = \frac{-e\boldsymbol{E}/m}{({\omega_0}^2 - \omega^2 - i\gamma\omega) - \hat{\sigma}eB\omega/m}. \tag{1.6}$$

In Eq. (1.6), we have defined $\omega_0 \equiv \sqrt{k/m}$. The electric displacement $\boldsymbol{D}$ is related to the relative dielectric constant of the material ε_m and polarization $\boldsymbol{P} = -Ne\boldsymbol{r}$ by $\boldsymbol{D} = \varepsilon_m\varepsilon_0\boldsymbol{E} = \varepsilon_0\boldsymbol{E} + \boldsymbol{P}$, where N is electron density [$1/\mathrm{m}^3$] and ε_0 is the permittivity of vacuum. By putting these relations into Eq. (1.6), ε_m is given by

$$\varepsilon_m(\omega) = 1 + \frac{Ne^2}{m\varepsilon_0}\frac{1}{({\omega_0}^2 - \omega^2 - i\gamma\omega) - \hat{\sigma}eB\omega/m}. \tag{1.7}$$

In term of ε_m, complex index of refraction is given as follows [45]:

$$\tilde{n}_{\hat{\sigma}}(\omega) = \sqrt{\varepsilon_m(\omega)} = n_{\hat{\sigma}}(\omega) + i\kappa_{\hat{\sigma}}(\omega), \tag{1.8}$$

where $n_{\hat{\sigma}}(\omega) \equiv \mathrm{Re}[\sqrt{\varepsilon_m(\omega)}]$ and $\kappa_{\hat{\sigma}}(\omega) \equiv \mathrm{Im}[\sqrt{\varepsilon_m(\omega)}]$. Therefore, from Eqs. (1.7) and (1.8), we can see that the velocity of light in the medium $v_{\hat{\sigma}} = c/n_{\hat{\sigma}}(\omega)$ for LCP and RCP lights are not the same in the case of $B \neq 0$. After traversing a distance L, the light accumulates a phase $\Phi_{\hat{\sigma}} = (\omega/c)n_{\hat{\sigma}}L$. The difference of phases between the transmitted LCP and RCP lights is the origin of the Faraday angle θ_F as follows [1]:

$$\theta_F = \frac{\Phi_+ - \Phi_-}{2} = \frac{\omega L}{2c}[n_+(\omega) - n_-(\omega)]. \tag{1.9}$$

By comparing Eqs. (1.9) with (1.1), the Verdet constant is given by

$$\mathcal{V} = \frac{\omega}{2cLB}[n_+(\omega) - n_-(\omega)], \tag{1.10}$$

which indeed depends on the frequency of light.

The imaginary part of $\tilde{n}_{\hat{\sigma}}(\omega)$, $\kappa(\omega)$ is related to the absorption of light [45], which means that the absorption probability for the LCP and RCP lights are not equal and thus CD occurs. The CD explains that the transmitted light is elliptically-polarized (a more detailed discussion on the ellipticity of light and CD is given in Chapters 2 and 4).

As for the Kerr effect in 3D materials, the derivation of θ_K requires the tensor form of ε_m [1]. Nevertheless, we can understand that the Kerr effect can occur because the reflection of light depends on $\tilde{n}_{\hat{\sigma}}(\omega)$, which as we have shown, are not equal of the LCP and RCP lights, either.

1.3.1.2 Faraday and Kerr effects in 2D materials and thin films

Here, we will briefly review the experimental observations of the Faraday and the Kerr effects for graphene with magnetic field and thin film topological insulator without magnetic field. This discussion will bring us to the concept of the Hall conductivity and the various Hall effects.

The discovery of graphene [46] in 2004, and the observations of its unusual properties [47, 48, 49, 50] have drawn researchers to investigate the Faraday and the Kerr effects in thin-film and 2D materials [6, 51, 52, 53], where the thickness is negligibly small. Graphene is a 2D material consisting carbon atoms which are arranged in a 2D honeycomb lattice. Near the Fermi energy, electron in graphene possesses a relativistic, linear energy dispersion obeying the Dirac equation [17, 48, 49], in contrast to the parabolic dispersion of electron gas in metals and semiconductors. Large Faraday and Kerr rotations [51, 52] (up to ~ 0.1 rad or $6°$) for light in terahertz (THz) regime has

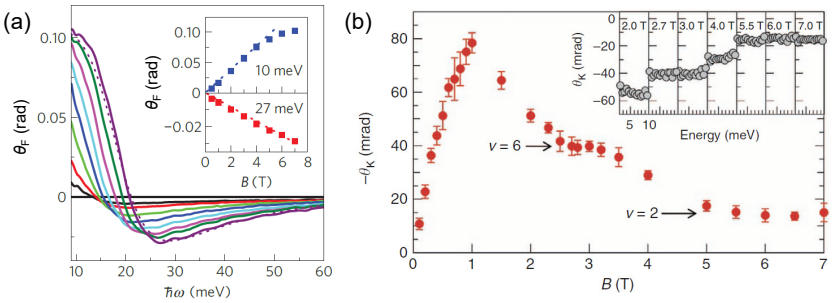

Figure 1.2 Experimental observations of the Faraday and the Kerr effects in doped graphene for light in the THz regime at temperature $T = 5$ K. (a) The Faraday rotation θ_F as a function of photon energy $\hbar\omega = 10 - 60$ meV ($2.42 - 14.51$ THz) in magnetic field $B = 0.5,\ 1,\ 2,\ 3,\ 4,\ 5,\ 6$ and 7 T. θ_F increases with increasing magnetic field, and the dashed line shows a fitting function. Inset: θ_F as a function of $B = 0 - 8$ T for $\hbar\omega = 10$ meV and 27 meV (adopted from ref. [51]). (b) The Kerr rotation θ_K as a function of $B = 1 - 7$ T at 1 THz. The arrows indicate the occurrence of the quantum Hall effect, where the Hall conductivity is quantized, i.e. $\sigma_{xy} = -\nu e^2/h$. Inset: θ_K as a function of $\hbar\omega = 0 - 10$ meV at $B = 2,\ 2.7,\ 3,\ 4,\ 5.5,\ 6$ and 7 T [52]. In (a) and (b), the values of the Fermi energy ϵ_F are -340 meV and 70 meV, respectively.

been experimentally observed for doped graphene with a magnetic field up to 7 T, even though the thickness of graphene is negligibly small. These phenomena occur because in the presence of the magnetic field, the optical Hall conductivity σ_{xy} is generated, which is proportional to carrier density in doped graphene.

In Fig. 1.2(a), we show an experimental measurement of the Faraday rotation [51] as a function of photon energy $\hbar\omega = 10 - 60$ meV ($2.42 - 14.51$ THz) for several values of magnetic field $B = 0.5 - 7$ T. Here, the angle θ_F increases with increasing magnetic field, and the dashed line shows a fitting function. The inset of Fig. 1.2(a) shows θ_F as a function of $B = 0 - 8$ T for $\hbar\omega = 10$ meV and 27 meV. It is observed that at $\hbar\omega = 10$ meV and $B = 7$ T, θ_F is around 0.1 rad, which corresponds to approximately $5.73°$. This value is large by considering the fact that the thickness of graphene is negligibly small. As a comparison, ~ 8 μm-thick La:YIG (material with large Verdet constant in the THz regime) is required to obtain $\theta_F = 5.73°$ for the given magnetic field. The origin of the large Faraday rotation in graphene is carrier density and surface current. To understand the mechanism of the Faraday rotation in graphene more clearly, let us consider graphene in the xy-plane, and let the electric field of the incident light oscillates in the x-direction, $\boldsymbol{E}_x(\omega)$, and therefore and alternating current density $\boldsymbol{J}_x(\omega)$ is generated. In the presence of the magnetic field $\boldsymbol{B} = B\hat{\boldsymbol{z}}$, the Lorentz force induce electrons to move in the direction perpendicular to the electric field of light, which generates a current density $\boldsymbol{J}_y(\omega)$ and radiates an electric field $\boldsymbol{E}_y(\omega)$. A fraction of $\boldsymbol{E}_y(\omega)$ is observed as an electric field component of transmitted light. The total electric field of the transmitted light possesses both x- and y- components, and therefore, the polarization direction of the transmitted light is rotated from that of the incident light, which is the origin of the Faraday rotation. Similarly, a fraction of

Fig. 1.2: fig/ch1/theta-exp.eps

the radiation generated by $\boldsymbol{J}_y$ also contributes to the total electric field of reflected light, which is the origin of the Kerr rotation.

In general, the currents $\boldsymbol{J}_x$, $\boldsymbol{J}_y$ are related to the electric fields $\boldsymbol{E}_x$, $\boldsymbol{E}_y$ by the conductivity tensor as as follows:

$$\begin{pmatrix} J_x \\ J_y \end{pmatrix} = \begin{pmatrix} \sigma_{xx} & \sigma_{xy} \\ \sigma_{yx} & \sigma_{yy} \end{pmatrix} \begin{pmatrix} E_x \\ E_y \end{pmatrix}. \tag{1.11}$$

In Eq. (1.11), σ_{xx} and σ_{yy} are called longitudinal conductivities, while σ_{xy} and σ_{yx} are called *transversal or Hall conductivities*. We shall show that $\sigma_{xx} = \sigma_{yy}$ and $\sigma_{xy} = -\sigma_{yx}$ if the 2D material is isotropic in the xy-plane. In the presence of an external magnetic field, a material with finite Hall conductivity exhibits the *Hall effect*. In doped graphene, the *optical* longitudinal and the Hall conductivities are given by [51]

$$\sigma_{xx}(\omega) = \frac{2D}{\pi} \frac{1/\tau - i\omega}{{\omega_c}^2 - (\omega + i/\tau)^2}, \tag{1.12}$$

and

$$\sigma_{xy}(\omega) = -\frac{2D}{\pi} \frac{\omega_c}{{\omega_c}^2 - (\omega + i/\tau)^2}, \tag{1.13}$$

respectively. Here, the term 'optical' refers to the dependence of the optical conductivities on light frequency ω, D is the Drude weight which is proportional to electron density [1/m^2]. τ is the scattering rate of an electron which is inverse of the damping constant γ, i.e. $\tau = 1/\gamma$. $\omega_c = e{v_F}^2 B/\epsilon_F$ is the cyclotron frequency of an electron in doped graphene, where v_F and ϵ_F are the Fermi velocity and the Fermi energy of graphene [51], respectively. The Faraday rotation is related to $\sigma_{xy}(\omega)$ as follows:

$$\theta_F \approx Z_0 f_s(\omega) \mathrm{Re}[\sigma_{xy}(\omega)], \tag{1.14}$$

where $Z_0 = 376.73$ is impedance of the vacuum and $f_s(\omega)$ is the spectral function which depends on the substrate in the experimental set-up of the Faraday effect. From the functional form of $\mathrm{Re}[\sigma_{xy}(\omega)]$, the Faraday rotation is maximum when the frequency of light match to the cyclotron frequency $\omega = \omega_c$, in the case of $\omega \gg \tau$. Moreover, from Eqs. (1.13) and (1.14), we can see that in a constant ω, θ_F linearly increases with increasing B, as shown in the inset of Fig. 1.14(a).

In Fig. 1.2(b), we show an experimental observation of the Kerr rotation as a function of $B = 1 - 7$ T at 1 THz [52]. It is noted that the sign of the Kerr angle θ_K is opposite to that of θ_F in Fig. (1.2)(a), because in the experimental set up of ref. [51] (ref. [52]), $\boldsymbol{B}$ is anti-parallel (parallel) to the direction of propagation of incident light. For small magnetic field up to ~ 1 T, the magnitude of θ_K linearly increases with increasing B, which suggests that the dependence of θ_K is well-described by the Drude model of the optical Hall conductivity [Eq. (1.13)]. Nevertheless, for $B > 2$ T, the Kerr rotation shows plateau structures. This phenomenon indicates the occurrence of the *quantum Hall effect* in graphene [54, 55, 56, 57, 58], where the value of the Hall conductivity is integer multiple of e^2/h, that is $\sigma_{xy} = -\nu e^2/h$, and $\sigma_{xx} = 0$. At $B \approx 2.5$ T and $B \approx 5$ T, $\nu = 6$ and $\nu = 2$, respectively. In the inset of Fig. 1.2(b) we show the Kerr rotation as a function of $\hbar\omega = 0 - 10$ meV at $B = 2,\ 2.7,\ 3,\ 4,\ 5.5,\ 6$

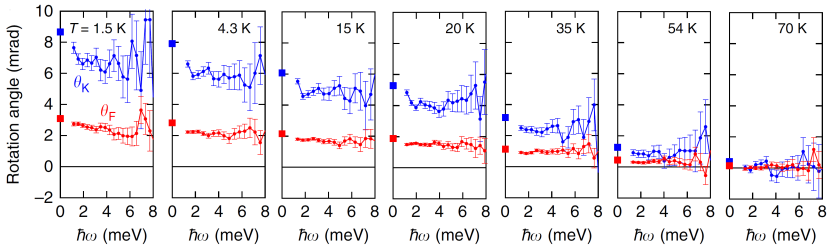

Figure 1.3 Experimental observations of the Faraday angle θ_F (red) and the Kerr angle θ_K (blue) in $Cr_x(Bi_{0.26}Sb_{0.74})_{2-x}Te_3$ thin film as a function of photon energy $\hbar\omega = 0 - 8$ meV for several values of temperature $T = 1.5,\ 4.3,\ 15,\ 20,\ 35,\ 54$ and 70 K. The angles θ_F and θ_K at $\hbar\omega = 0$ (closed squares) are extrapolated values [8].

and 7 T [52]. Here, the magnitude of the Kerr rotation decreases with increasing photon energy and magnetic field.

Finally, we discuss the Faraday and the Kerr effects for light in the THz regime without magnetic field [8]. In Fig. 1.3, we show an experimental measurement of the Faraday and the Kerr rotations a thin film, topological insulator $Cr_x(Bi_{0.26}Sb_{0.74})_{2-x}Te_3$ as a function of photon energy $\hbar\omega = 0 - 8$ meV for several values of temperature $T = 1.5,\ 4.3,\ 15,\ 20,\ 35,\ 54$ and 70 K. In this case, the role of Cr atoms ($x = 0.57$) is magnetic impurities in the topological insulator, and thus the topological insulator possesses intrinsic magnetization (or magnetic moment). Because of non-zero magnetization, the topological insulator possesses a quantized value of the Hall conductivity $\sigma_{xy} = e^2/h$, which we call the *quantum anomalous Hall state*. As $\hbar\omega$ approaches zero, it is observed that θ_F and θ_K tend to become constants. For example, at $T = 1.5$ K and $\hbar\omega = 0$, it is estimated that the values of θ_F and θ_K around 3.1 mrad (0.18°) and 8.7 mrad (0.5°), respectively. It is noted that the spectra of θ_F shows almost constant values, especially at low $\hbar\omega$, while the spectra of θ_K shows noisy structures.

We have seen that the origin of the Faraday and the Kerr rotations in 2D materials and thin films is the Hall conductivity σ_{xy}, which is generated by the Hall effect, the quantum Hall effect, and the quantum anomalous Hall effect. In the next section, we will briefly review the various Hall effects relevant to the content of this thesis. At the end, we discuss the 2D Haldane model as a material which exhibits the quantum anomalous Hall state.

1.3.2 Quantum Hall effect and Haldane model

1.3.2.1 Classical and quantum Hall effects

The Hall effect [59] is a transport phenomenon in a conductor, where the Hall voltage V_y is generated perpendicular to the current I_x and an external magnetic field $\boldsymbol{B} = B\hat{\boldsymbol{z}}$, as shown in Fig. 1.4(a). In order to understand the origin of the Hall effect, let us recall that in the presence of $\boldsymbol{B}$, electrons in conductor experience the Lorentz force given by Eq. (1.2). Since in conductor the electrons are free, we can use Eq. (1.3) and

Fig. 1.3: fig/ch1/theta-qah.eps

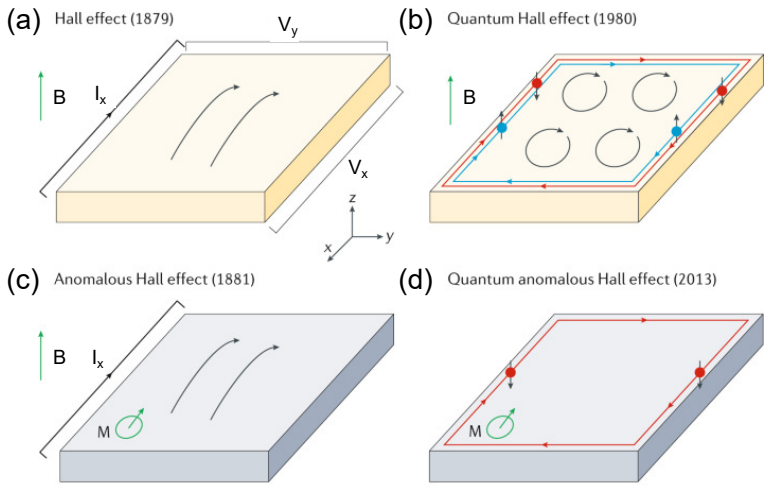

Figure 1.4 Schematic illustrations of various Hall effects. (a) The Hall effect, J_{xx} and V_y are the longitudinal current density and the Hall voltage, respectively. (b) The quantum Hall effect. The red (blue) sphere with downward (upward) arrow represents spin down (up) electron. (c) The anomalous Hall effect, M is intrinsic magnetization. (d) Quantum anomalous Hall effect. Adopted from ref. [13].

set the restoring force of an electron $\boldsymbol{F}_H = 0$ as follows:

$$m\frac{d\boldsymbol{v}}{dt} = -\frac{m}{\tau}\boldsymbol{v} - e(\boldsymbol{E} + \boldsymbol{v} \times \boldsymbol{B}), \tag{1.15}$$

where $\tau = 1/\gamma$ is the relaxation time, which is an average time between scattering of electrons by a defect in lattice or a phonon. It is noted that in this case, the electric field $\boldsymbol{E}$ is not the electric field of light, but instead it is generated by the voltages V_x and V_y. By considering the stationary case, i.e. $d\boldsymbol{v}/dt = 0$, we get

$$\frac{\tau e}{m}(\boldsymbol{v} \times \boldsymbol{B}) + \boldsymbol{v} = -\frac{e\tau}{m}\boldsymbol{E}. \tag{1.16}$$

The current density $\boldsymbol{J}$ is related to electron density N [1/m^2] by

$$\boldsymbol{J} = -Ne\boldsymbol{v}. \tag{1.17}$$

By substituting Eq. (1.17) to Eq. (1.16), the x- and y- components of $\boldsymbol{J}$ and $\boldsymbol{E}$ are given by

$$\frac{1}{\sigma_0}\begin{pmatrix} 1 & +\omega_c\tau \\ -\omega_c\tau & 1 \end{pmatrix}\begin{pmatrix} J_x \\ J_y \end{pmatrix} \equiv \begin{pmatrix} \rho_{xx} & \rho_{xy} \\ \rho_{yx} & \rho_{yy} \end{pmatrix}\begin{pmatrix} J_x \\ J_y \end{pmatrix} = \begin{pmatrix} E_x \\ E_y \end{pmatrix}, \tag{1.18}$$

where $\omega_c \equiv eB/m$ is the cyclotron frequency, which can be obtained by equating the Lorentz force ($E = 0$) with the centripetal force $F_c = mv^2/r$, and $\sigma_0 \equiv Ne^2\tau/m$ is

Fig. 1.4: fig/ch1/hall.eps

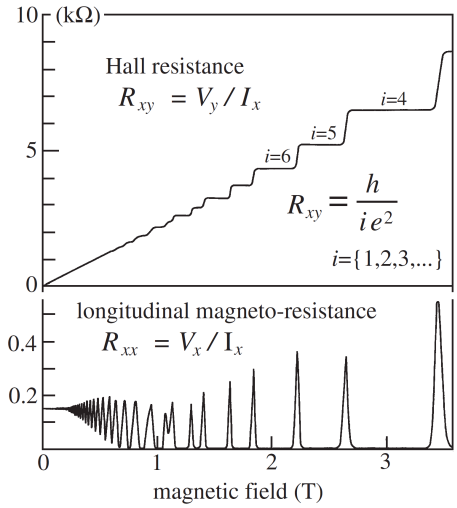

Figure 1.5 The quantum Hall effect in GaAs/(AlGa)As heterostructure. Experimental measurement of the longitudinal and the Hall resistances, R_{xx} and R_{xy}, respectively, as a function of magnetic field [62].

transport Drude conductivity. In the middle of Eq. (1.18), we define the resistivity tensor, from which we get

$$\rho_{xx} = \rho_{yy} = \frac{m}{Ne^2\tau}, \qquad \rho_{xy} = -\rho_{yx} = \frac{B}{Ne}. \tag{1.19}$$

By taking the inverse of the resistivity tensor to obtain the conductivity tensor in Eq. (1.11), the transport longitudinal and the Hall conductivities are given by

$$\sigma_{xx} = \sigma_{yy} = \sigma_0 \frac{1}{1+(\omega_c\tau)^2}, \qquad \sigma_{xy} = -\sigma_{yx} = -\sigma_0 \frac{\omega_c\tau}{1+(\omega_c\tau)^2}. \tag{1.20}$$

In terms of σ_{xx} and σ_{xy}, the longitudinal and the Hall resistivities are given by

$$\rho_{xx} = \frac{\sigma_{xx}}{{\sigma_{xx}}^2 + {\sigma_{xy}}^2}, \qquad \rho_{xy} = \frac{-\sigma_{xy}}{{\sigma_{xx}}^2 + {\sigma_{xy}}^2}. \tag{1.21}$$

The current I_x is given by $L_y J_x$, where L_y is the width of the conductor in the y-direction and J_x is the current density in 2D material [A/m]. The longitudinal and the Hall resistances are given by $R_{xx} = V_x/I_x$ and $R_{xy} = V_y/I_x$, respectively. By expressing $V_y = L_y E_y$, the Hall resistance is given by $R_{xy} = E_y/J_x$, therefore $R_{xy} = \rho_{yx} = -\rho_{xy}$. Similarly, $R_{xx} = L_x E_x/(L_y J_x) = (L_x/L_y)\rho_{xx}$, where L_x is the length of the conductor in the x-direction.

In Fig. 1.4(b), we show a schematic illustration for the quantum Hall effect [60, 61, 62, 63, 64], which was discovered by von Klitzing in 1980 [60]. Here, in the presence of a strong magnetic field, electrons in conductor move in closed orbits due to the Lorentz

Fig. 1.5: fig/ch1/klitzing.eps

force, which is known as the cyclotron motion. In Fig. 1.5, we show a measurement of R_{xx} and R_{xy} in GaAs/(AlGa)As heterostructure as a function of magnetic field. At a relatively low magnetic field, $R_{xx} \propto \rho_{xx}$ is constant, while $R_{xy} = -\rho_{xy}$ increases linearly with increasing magnetic field, in agreement with Eq. (1.19). Nevertheless, at strong magnetic field , it is observed that R_{xy} stays on plateau for a range of magnetic field, and exhibits a step-like increase between plateaus. R_{xx} becomes zero except when the transition between plateaus occurs for R_{xy}, where R_{xx} shows a sharp peak. At the plateau, $R_{xx} = 0$ and from Eq. (1.21), $\sigma_{xx} = 0$. On the contrary, $R_{xy} = h/(ie^2)$, where $i = 1,\ 2,\ 3, ...$, etc. Therefore, the Hall conductivity is quantized as follows:

$$\sigma_{xy} = \frac{1}{R_{xy}} = i\frac{e^2}{h}, \tag{1.22}$$

which we call the quantum Hall effect. The origin of the quantum Hall effect is that the energy dispersion of electron is quantized in a strong magnetic field, which is known as the *Landau levels* (see Chapter 3.1 for derivations of the Landau levels in 2D electron gas and 2D Dirac fermions). The number of electrons per unit area occupying each Landau level (the Landau degeneracy) is given by eB/h. i is called the filling factor, given by $i = Nh/(eB)$. When i is integer, all electron occupy the Landau levels and therefore, the are no states for the free carriers. As a result, the longitudinal resistivity and conductivity become zero [see Eq. (1.21)] and electrons are confined into closed orbits, except at the edges of the conductor. Thus, in the quantum Hall state, the 2D electron gas system only conducts electrons at the edges.

In Fig. 1.4(c), we show a schematic illustration for the *anomalous Hall effect* [65], in which the Hall voltage V_y is ten-times larger in ferromagnetic materials compared with those of non-magnetic conductors, because of the presence of intrinsic magnetization M in the ferromagnetic materials . In this case, V_y is proportional to M [11].

In Fig. 1.4(d), a schematic illustration for the quantum anomalous Hall effect [9, 10, 11, 12, 13] is shown. Here, without an external magnetic field, the material shows a quantized Hall conductivity due to interplay between strong orbit coupling and magnetic impurities, which gives the material intrinsic magnetization M. In the next section, we shall discuss a model of 2D hexagonal material in the quantum anomalous Hall state, which is known as the Haldane model.

1.3.2.2 Haldane model

The *Haldane model* [16, 17, 18, 19, 20, 21] is a model for spinless fermion in a 2D material which exhibits the quantum anomalous Hall effect, by introducing complex next-nearest-neighbour (NNN) interaction in a hexagonal lattice. In Fig. 1.6(a), we show the hexagonal lattice for the Haldane model, where a is the lattice constant and the strength of nearest-neighbour (NN) interaction between atom A and B is given by $-t_1$ ($t_1 > 0$). The NNN interaction is given by $t_2 e^{i\phi}$ ($t_2 e^{-i\phi}$) for clockwise (anticlockwise) direction, where we define $t_2 > 0$. The phase angle ϕ can be regarded as a virtual magnetic flux which breaks the time reversal symmetry, but since the signs of the phase angle are opposite for the clockwise and anticlockwise NNN hopping directions, the total magnetic flux in the honeycomb lattice is zero [16]. The on-site energy for the A and B atoms are given by $+M$ and $-M$, respectively. Experimentally, the Haldane model has been realized by using cold atoms in an optical lattice [22].

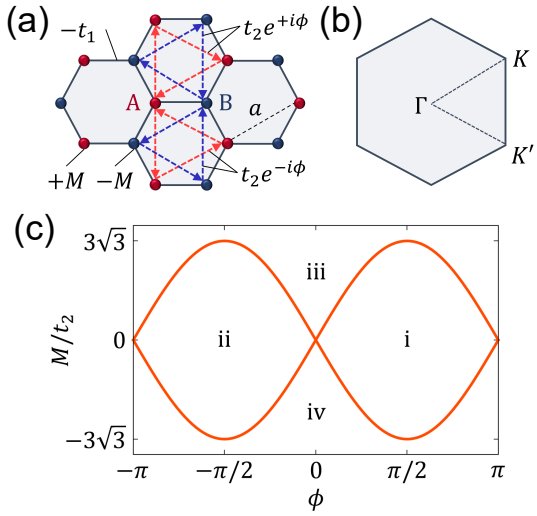

Figure 1.6 (a) The 2D hexagonal lattice of the Haldane model, with the lattice constant a. The strength of the NN hopping is given by $-t_1$. The complex NNN hopping is expressed by $t_2e^{+i\phi}$ ($t_2e^{-i\phi}$) for the clockwise (anticlockwise) direction. The on-site energy for A (B) sublattice is $+M$ ($-M$). (b) The Brillouin zone of the 2D hexagonal lattice with high symmetry points. (c) Topological phase diagram of the Haldane model. The topological (trivial) insulator phases are denoted by i and ii (iii and iv) (adopted from ref. [66]).

Moreover, it is theoretically suggested that the Haldane model can be synthesized in a hexagonal ferromagnetic insulators $AFe(PO_4)_2$, A = Ba, Cs, K, La [23].

In Fig. 1.6(b), we show the Brillouin zone of the Haldane model in the reciprocal lattice, where Γ, K, and K' are high symmetry points. In Chapter 2, we derive energy dispersion of the Haldane model especially near the K and K' points in the Brillouin zone.

In Fig. 1.6(c), we depict the so-called topological phase diagram for the Haldane model [16]. The phase of the Haldane is determined by the parameters t_2, ϕ, and M. The regions i and ii, where $M/t_2 < 3\sqrt{3}\sin\phi$, are called the topological phases [20] of the Haldane model. In the topological phases, the Haldane model shows the quantum Hall effect and the transport conductivity is quantized, i.e. $\sigma_{xy} = \pm e^2/h$. In the regions iii and iv ($M/t_2 < 3\sqrt{3}\sin\phi$) are called the tivial phases of the Haldane model, where $\sigma_{xy} = 0$.

We also mention optical properties of the Haldane model which are relevant for the results of this thesis in Chapter 4. The calculation of optical absorption in the Haldane model within the dipole approximation has been performed by Ghalamkari et al [67] . In the dipole approximation, the absorption in material is determined by polarization direction of electric field, and not the frequency of light. In the regions i and ii, the Haldane model shows the CD, where absorption probability of the LCP and RCP lights are not equal. On the other hand, in the regions iii and iv, the Haldane model shows the *valley polarization* (VP), in which LCP (RCP) light is only absorbed by electron at the K (K') valley, or vice versa. In Chapter 4, we derive the analytical

Fig. 1.6: fig/ch1/haldane.eps

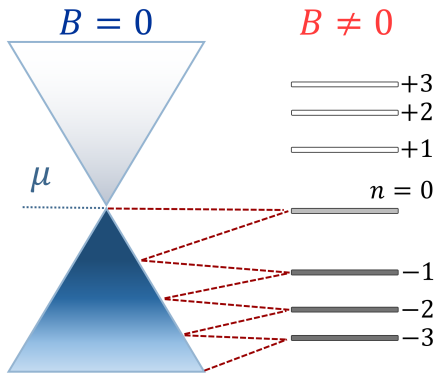

Figure 1.7 A schematic illustrate of the LLs formation ($n = -3$ to $n = +3$ are shown) in the Dirac cone of graphene. The level of chemical potential μ is given by the dotted line. Dashed lines represent the change of energy from $B = 0$ to $B \neq 0$. At $\mu = 0$, the $n = -3$ to $n = -1$ are fully occupied, while $n = 0$ is half-occupied.

expression of the optical Hall conductivity $\sigma_{xy}(\omega)$ of the Haldane model, in order to discuss the Faraday and the Kerr effects, as well as CD and VP in the Haldane model.

1.3.3 Magnetization in Dirac fermions

1.3.3.1 Landau level formations and diamagnetism in graphene

We have mentioned that in the presence of an external magnetic field, the Landau levels (LLs) formation takes place, as a result, the continuous energy dispersions of electrons are quantized into discrete energy levels. Here, we will discuss the LL formations in graphene and its implication on the magnetic properties of graphene.

In Fig. 1.7, we illustrate electronic states in undoped graphene (where we set the chemical potential $\mu = 0$), in the absence and presence of an external magnetic field B perpendicular to the graphene plane. In the absence of the magnetic field ($B = 0$), the electronic energy dispersion of graphene near the level of the chemical potential is given by [49]

$$\epsilon(k) = \mp \hbar v_F k, \tag{1.23}$$

where v_F is the Fermi velocity and the wave vector k is measured from the K and K' points in the 2D hexagonal Brillouin zone. The $-$ $(+)$ indicates the valence (conduction) band. Thus, near the K and K' point as shown in Fig. 1.6(b), an electron in graphene possesses linear energy dispersion, which is known as the *Dirac cone*. When we turn on magnetic field perpendicular to the graphene plane $B \neq 0$, the LLs are formed. The expression of the LL at the Dirac cone is given by [26, 68, 69, 70, 71, 72]:

$$\epsilon_n = \mathrm{sgn}(n)\sqrt{2\hbar {v_F}^2 eB|n|}, \tag{1.24}$$

Fig. 1.7: fig/ch1/landau.eps

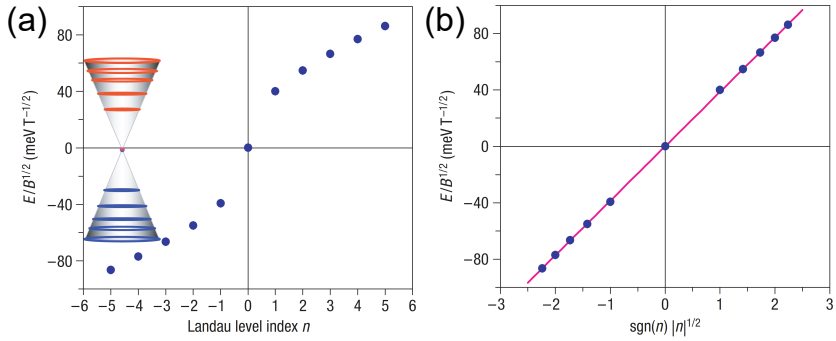

Figure 1.8 Experimental observation of the LLs in graphene at temperature $T = 4.4$ K. The energy of the LLs are plotted as a function of (a) the LL index n and (b) $\mathrm{sgn}(n)|n|^{1/2}$. Inset in (a) shows the LLs superposed on the Dirac cone. Adopted from ref. [69].

where the sign function $\mathrm{sgn}(n) = -1$ for $n < 0$ and $\mathrm{sgn}(n) = +1$ for $n > 0$ (derivation of the LL in the Dirac fermions is given in Chapter 3.1). The $\sqrt{B}$ and $\sqrt{|n|}$ dependences of the LL of graphene has been confirmed by experiments [68, 69, 70, 71, 72]. In Fig. 1.8(a), we show an observation of the energy of the LL scaled by $\sqrt{B}$, $E/B^{1/2}$ as a function of the LL index n, where we can see a square-root dependence of $E/B^{1/2}$ on n. In Fig. 1.8(b), $E/B^{1/2}$ is plotted as a function of $\mathrm{sgn}(n)|n|^{1/2}$. Here, the experimental data are aligned into a straight line, which evidently shows the $\sqrt{|n|}$-dependence of the LL energy.

In the process of the LL formations, the states of electrons in the Dirac cone coalesce to the LLs as shown by Fig. 1.7. Let us determine the number of electron occupation in each. At $B = 0$ the number of electrons in graphene per unit area for each spin and valley is given by

$$N_{2D} = \frac{1}{(2\pi)^2}\pi k^2 = \frac{1}{4\pi}\frac{\epsilon^2}{(\hbar v_F)^2}. \tag{1.25}$$

At $B \neq 0$, the density of electron occupying the LL $n \leqslant -1$ is given by

$$\int_{\epsilon_{n+1/2}}^{\epsilon_{n-1/2}} d\epsilon\; g(\epsilon) = \frac{eB}{h}, \tag{1.26}$$

where

$$g(\epsilon) = \frac{dN_{2D}}{d\epsilon} = \frac{1}{2\pi}\frac{\epsilon}{(\hbar v_F)^2} \tag{1.27}$$

is the density of states of electron in per unit area. The right-hand side of Eq. (1.26) is known as the LL degeneracy. On the other hand, the number of electrons which coalesce to the zeroth LL ($n = 0$) is given by

$$\int_{0}^{\epsilon_{-1/2}} d\epsilon\; g(\epsilon) = \frac{eB}{2h}. \tag{1.28}$$

Fig. 1.8: fig/ch1/Landaulvl1.eps

Therefore, it is concluded that the zeroth is half-occupied for undoped graphene. The half-occupancy of the zeroth LL plays an important role in the diamagnetism of graphene especially at low temperature, as we will show in Chapter 5.

Now, let us discuss the magnetic properties of graphene. As indicated by Fig. 1.7, when electronic states are quantized to the LLs, the internal energy of graphene increases at the zeroth LL, while at the $n \neq 0$ LLs the changes of energy are negligibly small. At $T = 0$ K, the change of internal energy ΔE only depends on the change of magnetic field ΔB as follows:

$$\Delta E = -\boldsymbol{M} \cdot \Delta \boldsymbol{B}. \tag{1.29}$$

M is called *orbital magnetization*, which is a linear response of material in magnetic field. Physically, M represents the number of magnetic moments per unit area. In a non-magnetic material, the magnetic moment is given by $I\mathcal{A}$, where I is current and $\mathcal{A}$ is the area enclosed by the cyclotron motion of electron. Because in graphene the internal energy increases by increasing magnetic field, the sign of M in Eq. (1.29) is negative, which means that the direction of magnetic moment is anti-parallel to the direction of the magnetic field. The orbital susceptibility of graphene is given by

$$\chi = \frac{\partial M}{\partial B} < 0, \tag{1.30}$$

which indicates the orbital diamagnetism in graphene. It is noted that the orbital diamagnetism is much larger than the Pauli paramagnetism due to the spin of electron.

The calculation of χ for graphene at $T \neq 0$ K requires the concept of the thermodynamic potential defined by $\Omega \equiv E - TS - \mu N$, where S is entropy and N is excess carrier density due to the doping. By assuming electron doping ($\mu > 0$), Ω is expressed by the summations of all occupied LLs as follows [33]:

$$\Omega(B,T) = -4k_B T \frac{eB}{h} \sum_{n=-\infty}^{\nu} \ln\left[1 + e^{-\frac{\epsilon_n - \mu}{k_B T}}\right], \tag{1.31}$$

where the factor 4 represent the valley and spin degeneracies, k_B is the Boltzmann constant, and ν is the index of the highest occupied LL [derivation of Eq. (1.31) will be given in Chapter 3]. By considering the cut-off of the LL at the conduction band, the analytical expression of zero-field susceptibility as a function of μ and T is derived by McClure [24] as follows:

$$\chi(\mu,T) = -\left(\frac{\partial^2 \Omega}{\partial B^2}\right)_{B=0} = -\frac{e^2 {v_F}^2}{6\pi k_B T} \mathrm{sech}^2\left(\frac{\mu}{2k_B T}\right). \tag{1.32}$$

Therefore, at $T \to 0$ K, the orbital susceptibility in graphene diverges to $-\infty$. The divergence of the orbital susceptibility of graphene is known as the *anomalous diamagnetism*, and has been recently confirmed by an experiment [73].

A method to calculate the orbital susceptibility of massive Dirac fermions, which include gapped graphene and monolayer transition-metal dichalcogenides, are developed by Koshino and Ando [33, 34] by applying the Euler-Maclaurin formula in the calculation of $\Omega(B,T)$. The Euler-Maclaurin formula states that a summation of a function $f(n)$ from $n = a$ to $n = b$ can be transformed into an integral with some

additional terms as follows [74]:

$$\sum_{n=a}^{b} f_n \approx \int_a^b dn f(n) + \frac{1}{2}\Big[f(b)+f(a)\Big] + \frac{1}{12}\Big[f'(b)+f'(a)\Big], \tag{1.33}$$

which is valid for $f_{n+1} - f_n \ll f_n$. The $\Omega(B,T)$ in Eq. (1.31) can be calculated analytically with the Euler Maclaurin formula by choosing $f_n = [1+\exp\{-(\epsilon_n - \mu)/(k_BT)\}]$, as performed by Landau [75, 76] to demonstrate the orbital susceptibility in conventional metals, which is known as the *Landau diamagnetism*. Nevertheless, in metals we usually need to consider the LLs only in the the conduction bands, i.e $\epsilon_n > 0$ for $n = 0,\ 1,\ 2, ...$ (see Chapter 3), thus $f(n=\infty)$ and $f(n=0)$ converge. On the other hand, for the massive 2D Dirac materials, we need to consider the contribution of the LLs at the valence bands ($\epsilon_n < 0$ for $n \leqslant -1$), which implies that $\Omega(B,T)$ will be divergent in the summation from $n = -\infty$ to $n = -1$ [77]. In fact, the expression of M calculated by the Euler-Maclaurin formula takes the form

$$M = C_1 - C_2 B, \tag{1.34}$$

where $C_2 > 0$ and $|C_1| \to \infty$ because we include an infinite LLs at the valence bands. The susceptibility of gapped graphene at $T \to 0$ K is given by [33, 34]:

$$\chi = -\frac{2}{3\pi}\frac{(ev_F)^2}{\Delta}\Theta(|\Delta/2| - |\mu|), \tag{1.35}$$

where Δ is the energy band gap and $\Theta(x) = 1$ (0) for $x \geqslant 0$ (< 0) is the Heaviside step function. We can see that when the chemical potential enters the conduction or valence bands, i.e. $\mu > \Delta/2$, the orbital susceptibility suddenly becomes zero. This phenomenon is called the *pseudospin paramagnetism* in the massive Dirac fermions. At the limit of $\Delta \to 0$, the anomalous orbital susceptibility is recovered.

An experimental measurement on the orbital magnetization M of undoped graphene ($\mu = 0$) for wide ranges of magnetic field B and temperature T has been performed by Li. et al. [78]. In Fig. 1.9(a), we show M as a function of $B = 0 - 8$ T for $T = 50,\ 100,\ 150,\ 200,\ 250$ and 300 K. For low temperature temperature, we can see that M exhibits $\sqrt{B}$-dependence due to the LLs of graphene [see Eq. (1.24)]. As temperature increases, the magnitude of M decreases, and M becomes linearly depends on B. In Fig. 1.9(b), we show M as a function of $T = 0-300$ K for $B = 0.5,\ 1,\ 1.5,\ 2,\ 2.5$ and 3 T.

In order to capture the empirical dependences of M on B and T, the experimental data in Fig. 1.9 are fitted into a Langevin function $L(x) \equiv \coth(x) - 1/x$ as follows [78]:

$$M = -\frac{0.882}{\pi}\frac{e^{3/2}v_F\sqrt{B}}{\hbar^{1/2}} L\left(\frac{\sqrt{\hbar v_F^2 eB\alpha(T)}}{\sqrt{2}k_BT}\right). \tag{1.36}$$

Here, $\alpha(T)$ is a phenomenological function defined by $\alpha(T) \equiv C/(C+\sqrt{T})$, where $C = 45\ \mathrm{K}^{1/2}$. Since $L(x) \sim x/3$ as $x \to 0$ and saturated to 1 as $x \to \infty$, the magnetization of graphene for strong field/low temperature ($\hbar\omega_c \gg k_BT$) and weak

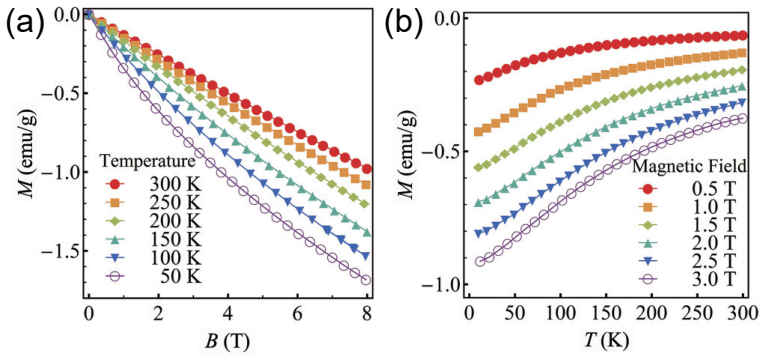

Figure 1.9 Experimental measurement of magnetization M as a function of magnetic field B and temperature T. M as a function of (a) $B = 0 - 8$ T for $T = 50,\ 100,\ 150,\ 200,\ 250$ and 300 K, (b) $T = 0 - 300$ K for $B = 0.5,\ 1,\ 1.5,\ 2,\ 2.5$ and 3 T (adopted from ref. [78]).

field/high temperature ($\hbar\omega_c \ll k_B T$) limits are given by

$$M \approx \begin{cases} -\dfrac{0.882}{\pi}\dfrac{e^{3/2}v_F}{\hbar^{1/2}}\sqrt{B} + \dfrac{0.882\sqrt{2}}{\pi}\dfrac{e}{\hbar}k_B T, \ (\hbar\omega_c \gg k_B T), \\ -\dfrac{0.882}{3\sqrt{2}}\dfrac{e^2 {v_F}^2}{\pi}\dfrac{B}{k_B T}, \ (\hbar\omega_c \ll k_B T). \end{cases} \tag{1.37}$$

Thus, for $\hbar\omega_c \gg k_B T$, the magnetization is proportional to the square-root of the magnetic field and diminishes linearly with increasing temperature ($M \propto -\sqrt{B} +$ constant $\times\, T$), while for $\hbar\omega_c \ll k_B T$, it is observed that the magnetization is proportional to B and inversely proportional to T ($M \propto -B/T$). This behaviour should be reproduced by theory, which is the second subject of this thesis.

Another magnetic property of the 2D Dirac materials discussed in this thesis is the *de Haas-van Alphen (dHvA) effect* [79, 80, 81, 82, 83, 84, 85]. The dHvA effect is oscillation of magnetization or susceptibility in metallic materials with respect to magnetic field, which is observed at low temperatures. An example of experimental observation of the dHvA oscillation in quasi-2D graphite at $T = 2$ K [79] is given by Fig. 1.10, where we can see that the susceptibility χ oscillates as a function of inverse magnetic field $1/H$ ($H \approx B/\mu_0$ for non-magnetic material, where μ_0 is the permeability of vacuum). Fig. 1.10 also shows a related phenomenon called Shubnikov-de Haas effect [79], in which oscillations is observed for resistance R.

To understand the origin of the dHvA effect in a material, let us recall that with increasing magnetic field, the energy of the LL also increases. By assuming that the level of chemical potential is kept constant (which can be realized by applying a gate voltage), the energy of the material increases discretely when the highest LL match to the chemical potential. On the other hand, the energy continuously decreases when the chemical potential is located between two consecutive LLs. Therefore, for a given range of magnetic field, the energy of the material is alternately increasing and decreasing. This phenomenon is manifested as the oscillation of magnetization and susceptibility.

Fig. 1.9: fig/ch1/M-exp.eps

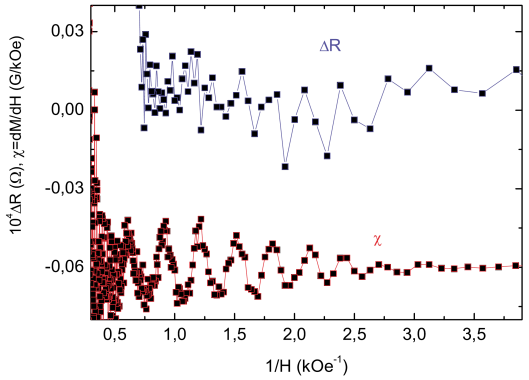

Figure 1.10 Oscillations of susceptibility χ (dHvA effect) and resistance R (Shubnikov-de Haas effect) in quasi-2D graphite at $T = 2$ K as a function of $1/H$ [79].

It is noted that when we apply the gate voltage, number of carriers in the material is not constant. By turning off the gate voltage, we get a fixed number of carriers. In this scenario, the dHvA oscillation originates from the oscillation of the chemical potential.

Most of the theoretical studies on the magnetic oscillations in the 2D systems [79, 80, 81, 82, 83, 84, 85] have been carried out within the framework of a generalized Lifshitz-Kosevich (LK) [85] theory, which was originally proposed to account the magnetic oscillations in metals. In the LK theory, the dHvA effect is expressed by adding an oscillatory term to the Euler-Maclaurin formula (also known as the Poisson summation formula) for calculating the thermodynamic potential. Onsager [86] demonstrated that the period P of the dHvA oscillation (the distance of $1/B$ between neighbouring amplitude peaks) is related to the cross section of the Fermi surface A_F in the normal direction of the magnetic field, as follows:

$$P = \frac{2\pi e}{\hbar A_F}. \tag{1.38}$$

Therefore, the dHvA oscillation can be utilized to reconstruct the Fermi surface of metallic materials by changing the direction of the magnetic field.

We have seen that the Euler-Maclaurin formula can not reproduce the experimentally observed behaviour of magnetization of undoped graphene. In order to derive analytical formula for $M(B, T, \mu)$ which agrees with the experimental observation, and thus to explain the origin of the magnetization behaviour, we will adopt the method of zeta function regularization in the calculation of the dHvA effect, too. In the context of quantum field theory, this method was used by Cangemi and Dunne [87] to calculate the energy of relativistic fermions in magnetic field. In graphene-related topics, the zeta function regularization was employed by Ghosal et al. [88] to explain the anomalous orbital diamagnetism of graphene at $T = 0$ K and by Slizovskiy and Betouras [89] to show the non-linear magnetization of graphene in a strong B. In the next Section, we will briefly discuss a classical example of the application of zeta function regularization on physics, that is the Casimir effect.

Fig. 1.10: fig/ch1/q-osc.eps

1.3.3.2 Zeta function regularization: Casimir effect

The *Casimir effect* (first predicted by H. Casimir [38] in 1948) is an attraction between two parallel, uncharged, and perfectly conducting plates, which are separated by a distance d. The attractive force F [41, 42] is given by

$$F_C = -\frac{\pi^2 \hbar c \mathcal{A}}{240 d^4}, \tag{1.39}$$

where $\mathcal{A}$ is the area of the plates and c is the speed of light in the vacuum. Thus, the Casimir force follows an inverse quartic dependence of the distance, in contrast to the inverse quadratic dependences of gravitational and electromagnetic forces. The origin of the Casimir effect is that according to the quantum field theory, the vacuum space consists of electromagnetic fluctuations of all wavelengths, that is, the electromagnetic modes are constantly created and annihilated in the vacuum. On the other hand, the number of the electromagnetic modes in the space between the plates are restricted, because only the modes with wavelengths half integer of d are allowed to exist by boundary conditions, to form standing waves between the plates. The illustration of the modes in the Casimir effect is illustrated by Fig. 1.11(a). Therefore, the energy density of electromagnetic modes inside the cavity is smaller than that outside it. The difference of the energy densities produces an attractive force between the plates.

Let us calculate the energy inside the cavity, which is summation of all possible modes with frequency ω_n as follows [38]:

$$\langle E \rangle = \frac{\hbar}{2} \sum_{n=1}^{\infty} \omega_n, \tag{1.40}$$

where by the boundary conditions, ω_n is given by

$$\omega_n = c\sqrt{{k_x}^2 + {k_y}^2 + \frac{n^2\pi^2}{d^2}}. \tag{1.41}$$

Here, k_x and k_y are wave vectors components perpendicular to d. By the integrations of k_x and k_y, the energy is given by [37]

$$\langle E \rangle = 2\mathcal{A}\frac{\hbar}{2} \int_0^{\infty} dk_x \int_0^{\infty} dk_y \sum_{n=1}^{\infty} \omega_n = \frac{\hbar c}{6d^3} \sum_{n=1}^{\infty} n^3. \tag{1.42}$$

Here, we multiply the energy by 2 to account two possible direction of polarizations. In the right-most side of Eq. (1.42), we get a divergent summation of n^3. In order to avoid the divergence, we express the summation in term of the Riemann zeta function as follows [74]:

$$\zeta(s) \equiv \sum_{k=1}^{\infty} \frac{1}{k^s}, \tag{1.43}$$

for $s \in \mathbb{C}$. The Riemann zeta function converges for any $s \neq 1$ by the method of analytic continuation in the complex plane (see Appendix A for derivation). For example, the infinite summation in Eq. (1.42) is expressed by $\zeta(-3) = -1/120$ [37]. By taking the derivation $-\partial\langle E \rangle/\partial d$, we obtain the Casimir force in Eq. (1.39). A possible

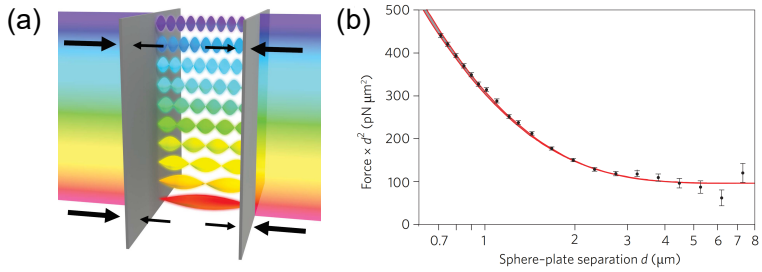

Figure 1.11 (a) Schematic illustration of electromagnetic modes inside and outside two conducting plates [42], which gives different zero point energy densities of photon. (b) Experimental measurement of the Casimir force between a gold-coated spherical surface (radius $R = 15.6$ cm and a gold-coated plate, multiplied by square of distance between surface d. The experimental data are compared with the Lifshitz theory (red lines) [41].

physical explanation of the convergence is that the zeta function regularization only takes the difference of energy between plates, and therefore we get a finite attractive force [42].

Theoretical calculation of the Casimir effect has been extended to include forces in different geometries, for example, between a sphere and a plate, partly due to experimental difficulties in measuring the Casimir force in the parallel-plate geometry 39, 40, 41]. Moreover, Lifshitz [42] have provided theoretical prediction of the Casimir forces between metallic and dielectric materials, which also takes into account the roughness of surface and allow some penetration by electric fields. The Casimir force between a conducting sphere and a plate is independent of the area of the plate, as follows [41, 42]:

$$F = -\frac{\pi^3 \hbar c R}{360 d^3}, \tag{1.44}$$

which is valid for $d \ll R$, where d is the distance between the sphere and the plate, and R is the radius of the sphere. In Fig. 1.11(b), we show an experimental measurement of the Casimir force between a gold-coated spherical surface (radius $R = 15.6$ cm and a gold-coated plate, multiplied by d^2. We can see that the experimental data confirm the validity of the Lifshitz theory.

As a summary, we have seen that the zeta function provides a useful tool to regularize a divergent summation which appears in theoretical formulation of some physical problems. In Chapter 5, we apply the zeta function regularization to derive analytical expressions for magnetization of the Dirac fermions.

Fig. 1.11: fig/ch1/casimir.eps

Chapter 2

Methods to calculate Faraday and Kerr rotations in 2D materials

In this chapter, we describe methods of calculations to obtain the results in Chapter 4. First, we derive electronic energy dispersion of the Haldane model by using the second-quantization formalism. Next, we discuss the linear response theory and derive the optical conductivity of 2D material. And finally, we discuss methods to obtain optical spectra of the 2D material, which include absorption probability, as well as the Faraday and the Kerr rotations.

2.1 Energy dispersion of Haldane model

In the second-quantization, Hamiltonian of a 2D material is expressed by the creation and annihilation operators. In particular, we will derive the energy dispersion of the Haldane model around the Dirac points, which is useful to describe low-energy excitations. Hamiltonian of the Haldane model [16, 17, 18] is given by

$$\hat{H} = -t_1 \sum_{\langle i,j \rangle} c_i^\dagger c_j + t_2 \sum_{\langle\langle i,j \rangle\rangle} e^{i\nu_{ij}\phi} c_i^\dagger c_j + M \sum_i \tau_i c_i^\dagger c_i \equiv \hat{H}_1 + \hat{H}_2 + \hat{H}_3, \tag{2.1}$$

where $c_i(c_i^\dagger)$ is the annihilation (creation) operator on the i-th atomic site. The first term $\hat{H}_1$ describes the nearest-neighbor (NN) interactions with the hopping integral $t_1 > 0$. The second term $\hat{H}_2$ denotes the next-nearest-neighbor (NNN) interactions with the hopping integral $t_2 > 0$. ν_{ij} denotes either $+1$ or -1 depending on the hopping direction. Due to a non-zero phase angle ϕ in $e^{i\nu_{ij}\phi}$, time-reversal ($\mathcal{T}$) symmetry is broken. The third term $\hat{H}_3$ denotes on-site energy difference between the A and B atoms, where we define $\tau_i = +1$ (-1) for the A (B) site. The $\hat{H}_3$ breaks inversion ($\mathcal{I}$) symmetry between the A and B atoms, and gives rise to the band gap $2M$ between valence and conduction bands.

To obtain the dispersion relation, we adopt the Fourier transform of c_i and $c_i^\dagger$ in the reciprocal space as follows:

$$c_i = \frac{1}{\sqrt{N}} \sum_{\boldsymbol{k}} e^{i\boldsymbol{k}\cdot\boldsymbol{R}_i} c_{\boldsymbol{k}}, \quad c_i^\dagger = \frac{1}{\sqrt{N}} \sum_{\boldsymbol{k}} e^{-i\boldsymbol{k}\cdot\boldsymbol{R}_i} c_{\boldsymbol{k}}^\dagger, \tag{2.2}$$

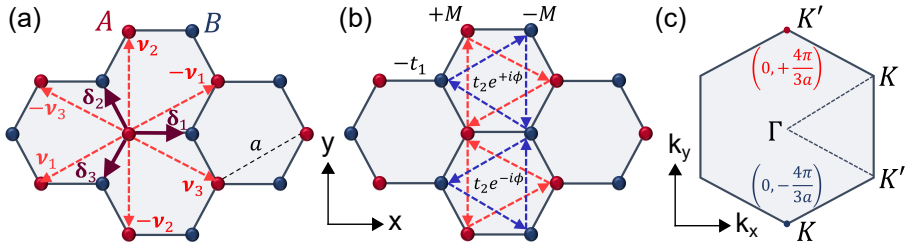

Figure 2.1 The Haldane model on hexagonal lattice. (a) The schematic definitions of NN vectors $\boldsymbol{\delta}_1$, $\boldsymbol{\delta}_2$, and $\boldsymbol{\delta}_3$ and NNN vectors $\pm\boldsymbol{\nu}_1$, $\pm\boldsymbol{\nu}_2$, and $\pm\boldsymbol{\nu}_3$. Here, a is the lattice constant of hexagonal lattice. (b) Illustration of the sign for the phase angle ϕ in the NNN interactions: ϕ is positive (negative) for clockwise (anticlockwise) hopping direction. (c) The Brillouin zone of the hexagonal lattice.

where N is the number of the atomic sites. By defining c_i and $c_i^\dagger$ for the A (B) site, $a_i(b_i)$ and $a_i^\dagger(b_i^\dagger)$, respectively, $\hat{H}_1$ as a function of $\boldsymbol{k}$ is given by

$$\begin{aligned}
\hat{H}_1(\boldsymbol{k}) &= -t_1 \sum_{\langle i,j\rangle} (a_i^\dagger b_j + b_j^\dagger a_i) \\
&= \frac{-t_1}{N} \sum_{\langle i,j\rangle} \sum_{\boldsymbol{k},\boldsymbol{k'}} (e^{-i\boldsymbol{k}\cdot\boldsymbol{R}_i} e^{i\boldsymbol{k'}\cdot\boldsymbol{R}_j} a_{\boldsymbol{k}}^\dagger b_{\boldsymbol{k'}} + e^{-i\boldsymbol{k'}\cdot\boldsymbol{R}_j} e^{i\boldsymbol{k}\cdot\boldsymbol{R}_i} b_{\boldsymbol{k'}}^\dagger a_{\boldsymbol{k}}) \\
&= \frac{-t_1}{N} \sum_{n=1}^{3} \sum_{i}^{N} \sum_{\boldsymbol{k},\boldsymbol{k'}} [e^{i(\boldsymbol{k'}-\boldsymbol{k})\cdot\boldsymbol{R}_i} e^{i\boldsymbol{k'}\cdot\boldsymbol{\delta}_n} a_{\boldsymbol{k}}^\dagger b_{\boldsymbol{k'}} + e^{i(\boldsymbol{k}-\boldsymbol{k'})\cdot\boldsymbol{R}_i} e^{-i\boldsymbol{k'}\cdot\boldsymbol{\delta}_n} b_{\boldsymbol{k'}}^\dagger a_{\boldsymbol{k}}] \\
&= -t_1 \sum_{n=1}^{3} \sum_{\boldsymbol{k},\boldsymbol{k'}} [\delta_{\boldsymbol{k},\boldsymbol{k'}} e^{i\boldsymbol{k'}\cdot\boldsymbol{\delta}_n} a_{\boldsymbol{k}}^\dagger b_{\boldsymbol{k'}} + \delta_{\boldsymbol{k},\boldsymbol{k'}} e^{-i\boldsymbol{k'}\cdot\boldsymbol{\delta}_n} b_{\boldsymbol{k'}}^\dagger a_{\boldsymbol{k}}] \\
&= -t_1 \sum_{n=1}^{3} \sum_{\boldsymbol{k}} [e^{i\boldsymbol{k}\cdot\boldsymbol{\delta}_n} a_{\boldsymbol{k}}^\dagger b_{\boldsymbol{k}} + e^{-i\boldsymbol{k}\cdot\boldsymbol{\delta}_n} b_{\boldsymbol{k}}^\dagger a_{\boldsymbol{k}}].
\end{aligned} \tag{2.3}$$

In the third line of Eq. (2.3), we substitute $\boldsymbol{R}_j = \boldsymbol{R}_i + \boldsymbol{\delta}_n$, where $\boldsymbol{\delta}_n$, $(n = 1,\ 2,\ 3)$ are the vectors connecting an A atom to the three nearest B atoms [see Fig. 2.1(a)] given by

$$\boldsymbol{\delta}_1 = a\Big(\frac{1}{\sqrt{3}}, 0\Big), \quad \boldsymbol{\delta}_2 = a\Big(-\frac{1}{2\sqrt{3}}, \frac{1}{2}\Big), \quad \boldsymbol{\delta}_3 = a\Big(-\frac{1}{2\sqrt{3}}, -\frac{1}{2}\Big), \tag{2.4}$$

where a is the constant of hexagonal lattice. The summation on index i is carried in the fourth line, where $\sum_i^N e^{\pm i(\boldsymbol{k'}-\boldsymbol{k})\cdot\boldsymbol{R}_i} = N\delta_{\boldsymbol{k},\boldsymbol{k'}}$ and $\delta_{\boldsymbol{k},\boldsymbol{k'}}$ is the Kronecker delta. In the fifth line, the summation on $\boldsymbol{k'}$ selects $\boldsymbol{k'} = \boldsymbol{k}$.

In the NNN interactions, it is noted that each atom at $\boldsymbol{R}_i$ is connected by the vectors $\pm\boldsymbol{\nu}_n$, $(n = 1,\ 2,\ 3)$ to the six next-nearest atoms, as illustrated by Fig. 2.1(a).

Fig. 2.1: fig/ch2/haldane-latt.eps

The NNN vectors are given by

$$\boldsymbol{\nu}_1 = \boldsymbol{\delta}_3 - \boldsymbol{\delta}_1 = a\Big(-\frac{\sqrt{3}}{2}, -\frac{1}{2}\Big), \quad \boldsymbol{\nu}_2 = \boldsymbol{\delta}_2 - \boldsymbol{\delta}_3 = a(0,1), \quad \boldsymbol{\nu}_3 = \boldsymbol{\delta}_1 - \boldsymbol{\delta}_2 = a\Big(\frac{\sqrt{3}}{2}, -\frac{1}{2}\Big). \tag{2.5}$$

Following the convention by Haldane [16], we take $\nu_{ij} = +1$ (-1) for clockwise (anticlockwise) hopping direction, as shown in Fig. 2.1(b). With the same procedure to derive Eq. (2.3), $\hat{H}_2(\boldsymbol{k})$ is given by

$$\begin{aligned}
\hat{H}_2(\boldsymbol{k}) &= t_2 \sum_{\langle\langle i,j\rangle\rangle} (e^{i\nu_{ij}\phi} a_i^\dagger a_j + e^{i\nu_{ij}\phi} b_i^\dagger b_j) \\
&= \frac{t_2}{N} \sum_{\langle\langle i,j\rangle\rangle} \sum_{\boldsymbol{k},\boldsymbol{k'}} (e^{i\nu_{ij}\phi} e^{-i\boldsymbol{k}\cdot\boldsymbol{R}_i} e^{i\boldsymbol{k'}\cdot\boldsymbol{R}_j} a_{\boldsymbol{k}}^\dagger a_{\boldsymbol{k'}} + e^{i\nu_{ij}\phi} e^{-i\boldsymbol{k}\cdot\boldsymbol{R}_i} e^{i\boldsymbol{k'}\cdot\boldsymbol{R}_j} b_{\boldsymbol{k}}^\dagger b_{\boldsymbol{k'}}) \\
&= \frac{t_2}{N} \sum_{i}^{N} \sum_{n=1}^{3} \sum_{\boldsymbol{k},\boldsymbol{k'}} [e^{i(\boldsymbol{k'}-\boldsymbol{k})\cdot\boldsymbol{R}_i} a_{\boldsymbol{k}}^\dagger a_{\boldsymbol{k'}} \{e^{i\boldsymbol{k'}\cdot\boldsymbol{\nu}_n} e^{i\phi} + e^{-i\boldsymbol{k'}\cdot\boldsymbol{\nu}_n} e^{-i\phi}\} + \\
&\quad e^{i(\boldsymbol{k'}-\boldsymbol{k})\cdot\boldsymbol{R}_i} b_{\boldsymbol{k}}^\dagger b_{\boldsymbol{k'}} \{e^{-i\boldsymbol{k'}\cdot\boldsymbol{\nu}_n} e^{i\phi} + e^{i\boldsymbol{k'}\cdot\boldsymbol{\nu}_n} e^{-i\phi}\}] \\
&= t_2 \sum_{n=1}^{3} \sum_{\boldsymbol{k},\boldsymbol{k'}} [2\cos(\boldsymbol{k'}\cdot\boldsymbol{\nu}_n + \phi)\delta_{\boldsymbol{k},\boldsymbol{k'}} a_{\boldsymbol{k}}^\dagger a_{\boldsymbol{k'}} + 2\cos(-\boldsymbol{k'}\cdot\boldsymbol{\nu}_n + \phi)\delta_{\boldsymbol{k},\boldsymbol{k'}} b_{\boldsymbol{k}}^\dagger b_{\boldsymbol{k'}}] \\
&= 2t_2 \sum_{n=1}^{3} \sum_{\boldsymbol{k}} [\cos(\boldsymbol{k}\cdot\boldsymbol{\nu}_n + \phi) a_{\boldsymbol{k}}^\dagger a_{\boldsymbol{k}} + \cos(\boldsymbol{k}\cdot\boldsymbol{\nu}_n - \phi) b_{\boldsymbol{k}}^\dagger b_{\boldsymbol{k}}].
\end{aligned} \tag{2.6}$$

Similarly, $\hat{H}_3(\boldsymbol{k})$ is derived as follows:

$$\begin{aligned}
\hat{H}_3(\boldsymbol{k}) &= M \sum_{i}^{N} (a_i^\dagger a_j - b_i^\dagger b_j) \\
&= \frac{M}{N} \sum_{i}^{N} \sum_{\boldsymbol{k},\boldsymbol{k'}} [e^{-i(\boldsymbol{k}-\boldsymbol{k'})\cdot\boldsymbol{R}_i} a_{\boldsymbol{k}}^\dagger a_{\boldsymbol{k'}} - e^{-i(\boldsymbol{k}-\boldsymbol{k'})\cdot\boldsymbol{R}_i} b_{\boldsymbol{k}}^\dagger b_{\boldsymbol{k'}}] \\
&= M \sum_{\boldsymbol{k},\boldsymbol{k'}} [\delta_{\boldsymbol{k},\boldsymbol{k'}} a_{\boldsymbol{k}}^\dagger a_{\boldsymbol{k'}} - \delta_{\boldsymbol{k},\boldsymbol{k'}} b_{\boldsymbol{k}}^\dagger b_{\boldsymbol{k'}}] \\
&= M \sum_{\boldsymbol{k}} [a_{\boldsymbol{k}}^\dagger a_{\boldsymbol{k}} - b_{\boldsymbol{k}}^\dagger b_{\boldsymbol{k}}].
\end{aligned} \tag{2.7}$$

By combining the results from Eqs. (2.3)-(2.7), the Hamiltonian $\hat{H}(\boldsymbol{k})$ can be expressed by a matrix as follows:

$$\begin{aligned}
\hat{H}(\boldsymbol{k}) &= \sum_{\boldsymbol{k}} \begin{bmatrix} a_{\boldsymbol{k}}^\dagger & b_{\boldsymbol{k}}^\dagger \end{bmatrix} \begin{bmatrix} M + 2t_2 \sum_{n=1}^{3} \cos(\boldsymbol{k}\cdot\boldsymbol{\nu}_n + \phi) & -t_1 \sum_{n=1}^{3} e^{i\boldsymbol{k}\cdot\boldsymbol{\delta}_n} \\ -t_1 \sum_{n=1}^{3} e^{-i\boldsymbol{k}\cdot\boldsymbol{\delta}_n} & -M + 2t_2 \sum_{n=1}^{3} \cos(\boldsymbol{k}\cdot\boldsymbol{\nu}_n - \phi) \end{bmatrix} \begin{bmatrix} a_{\boldsymbol{k}} \\ b_{\boldsymbol{k}} \end{bmatrix} \\
&\equiv \sum_{\boldsymbol{k}} \begin{bmatrix} a_{\boldsymbol{k}}^\dagger & b_{\boldsymbol{k}}^\dagger \end{bmatrix} \hat{\mathcal{H}}(\boldsymbol{k}) \begin{bmatrix} a_{\boldsymbol{k}} \\ b_{\boldsymbol{k}} \end{bmatrix}.
\end{aligned} \tag{2.8}$$

The matrix $\hat{\mathcal{H}}(\boldsymbol{k})$ in Eq. (2.8) can be expressed in term of the identity matrix $\hat{\sigma}_0$ and the Pauli matrices $\hat{\sigma}_x$, $\hat{\sigma}_y$, and $\hat{\sigma}_z$ as follows [16]:

$$\begin{aligned}\hat{\mathcal{H}}(\boldsymbol{k}) &= 2t_2\cos\phi\sum_{n=1}^{3}\cos(\boldsymbol{k}\cdot\boldsymbol{\nu}_n)\hat{\sigma}_0 - t_1\sum_{n=1}^{3}\cos(\boldsymbol{k}\cdot\boldsymbol{\delta}_n)\hat{\sigma}_x + t_1\sum_{n=1}^{3}\sin(\boldsymbol{k}\cdot\boldsymbol{\delta}_n)\hat{\sigma}_y \\ &\quad + \Big[M - 2t_2\sin\phi\sum_{n=1}^{3}\sin(\boldsymbol{k}\cdot\boldsymbol{\delta}_n)\Big]\hat{\sigma}_z \\ &\equiv \mathcal{H}_0(\boldsymbol{k})\hat{\sigma}_0 + \mathcal{H}_x(\boldsymbol{k})\hat{\sigma}_x + \mathcal{H}_y(\boldsymbol{k})\hat{\sigma}_y + \mathcal{H}_z(\boldsymbol{k})\hat{\sigma}_z.\end{aligned} \tag{2.9}$$

By solving the secular equation $\det[\hat{\mathcal{H}}(\boldsymbol{k}) - \epsilon(\boldsymbol{k})\hat{\sigma}_0] = 0$, the energy dispersion $\epsilon(\boldsymbol{k})$ is given by

$$\epsilon(\boldsymbol{k}) = \mathcal{H}_0(\boldsymbol{k}) \mp \sqrt{\mathcal{H}_x(\boldsymbol{k})^2 + \mathcal{H}_y(\boldsymbol{k})^2 + \mathcal{H}_z(\boldsymbol{k})^2}, \tag{2.10}$$

where the sign $-(+)$ corresponds to the valence (conduction) band. In Fig. 2.2, we plot $\epsilon(\boldsymbol{k})$ in the whole Brillouin zone by using $t_1 = 1$ eV, $t_2 = 0.05$ eV, $\phi = \pi/2$, and $M = 0.2$ eV. We can see that the band gap at the K point has a smaller value than that of the K' point.

In order to understand the effect of t_2 and ϕ on the band gap, let us define wave vector $\boldsymbol{q} = (q_x, q_y)$ measured from the $\boldsymbol{K} = (0, -4\pi/(3a))$ and $\boldsymbol{K}' = (0, +4\pi/(3a))$ points [see Fig. 2.1(c)], and derive the low-energy dispersion of the Haldane model. The terms in Eq. (2.9) which depend on $\boldsymbol{k}$ become

$$\begin{aligned}&\sum_{n=1}^{3}\cos(\boldsymbol{k}\cdot\boldsymbol{\delta}_n) = \pm\frac{\sqrt{3}}{2}q_y a, \qquad \sum_{n=1}^{3}\sin(\boldsymbol{k}\cdot\boldsymbol{\delta}_n) = \frac{\sqrt{3}}{2}q_x a, \\ &\sum_{n=1}^{3}\cos(\boldsymbol{k}\cdot\boldsymbol{\nu}_n) = -\frac{3}{2} + \mathcal{O}(\boldsymbol{q}^2), \quad \sum_{n=1}^{3}\sin(\boldsymbol{k}\cdot\boldsymbol{\nu}_n) = \pm\frac{3\sqrt{3}}{2} + \mathcal{O}(\boldsymbol{q}^2),\end{aligned} \tag{2.11}$$

where the sign $+(-)$ corresponds to the K (K') point. Let us rotate the Hamiltonian in Eq. (2.9) around the K and K' points by $+\pi/2$, which transforms $(q_x, q_y) \to (q_y, -q_x)$, in order to couple q_x and q_y with $\hat{\sigma}_x$ and $\hat{\sigma}_y$, respectively. Thus, we obtain effective Hamiltonian of the Haldane model as a function of $\boldsymbol{q}$, which is given by

$$\hat{\mathcal{H}}(\boldsymbol{q}) = -3t_2\cos\phi\hat{\sigma}_0 + \hbar v_F(\kappa q_x\hat{\sigma}_x + q_y\hat{\sigma}_y) + (M - \kappa 3\sqrt{3}\sin\phi)\hat{\sigma}_z, \tag{2.12}$$

where the Fermi velocity $v_F = \sqrt{3}at_1/(2\hbar)$ and we define the valley index $\kappa = +1(-1)$ for the K (K') valley. The energy dispersion of the Haldane model as a function of $\boldsymbol{q}$ is given by

$$\begin{aligned}\epsilon(\boldsymbol{q}) &= -3t_2\cos\phi \mp \sqrt{|\hbar v_F\boldsymbol{q}|^2 + (M - \kappa 3\sqrt{3}t_2\sin\phi)^2} \\ &\equiv -\zeta \mp \sqrt{(\hbar v_F q)^2 + {\Gamma_\kappa}^2},\end{aligned} \tag{2.13}$$

where we define $\zeta \equiv 3t_2\cos\phi$ and $\Gamma_\kappa \equiv M - \kappa 3\sqrt{3}t_2\sin\phi$. From Eq. (2.13), the energy dispersion at the valence band $\epsilon_v(\boldsymbol{q})$ and the conduction band $\epsilon_c(\boldsymbol{q})$ are related by

$$\epsilon_v(\boldsymbol{q}) + \zeta = -[\epsilon_c(\boldsymbol{q}) + \zeta]. \tag{2.14}$$

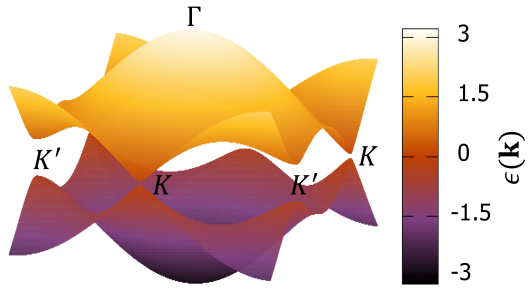

Figure 2.2 Energy dispersion of the Haldane model in the Brillouin zone. Here, we use $t_1 = 1$ eV, $t_2 = 0.05$ eV, $\phi = \pi/2$, and $M = 0.2$ eV.

The energy gap at the K ($\kappa = +1$) and the K' points ($\kappa = -1$) is given by

$$\epsilon_g^{(\kappa)} \equiv 2|\Gamma_\kappa|. \tag{2.15}$$

We can see that the energy gaps for the K and the K' points have different values when the $\mathcal{T}$ and the $\mathcal{I}$ symmetries are simultaneously broken ($t_2 \neq 0$, $\phi \neq 0$, and $M \neq 0$). In particular, in the case of $M = 3\sqrt{3}t_2 \sin\phi$, the energy gap only opens at the K' (K) valley for a positive (negative) ϕ.

By solving the eigenvalue of Eq. (2.12), the normalized wavefunctions of the Haldane model at the band $b = v, c$ is given as follows:

$$|b, \boldsymbol{q}\rangle = \frac{1}{\sqrt{2[\epsilon_b(\boldsymbol{q}) + \zeta]}} \begin{bmatrix} \sqrt{\epsilon_b(\boldsymbol{q}) + \zeta + \Gamma_\kappa} \\ \sqrt{\epsilon_b(\boldsymbol{q}) + \zeta - \Gamma_\kappa} e^{i\varphi/\kappa} \end{bmatrix}, \tag{2.16}$$

where we define $\varphi \equiv \arctan(q_y/q_x)$.

2.2 Linear response theory

In this section, we discuss the linear response theory [90, 91] and its application to the optical conductivity of 2D materials. The linear response means that the response of a weak perturbation is proportional to the strength of the perturbation. Therefore, the response can be obtained from the proportionality factor, which we generally call susceptibility. First, we derive the quantum mechanical expression of the linear response theory, which is known as the Kubo formula. Then, we apply the Kubo formula to derive the optical conductivity, where the perturbation is the electric field of an electromagnetic wave.

2.2.1 Kubo formula

We will briefly explain representations or 'pictures' of state vector and operator in the quantum mechanics, especially on their dependence on time. There are three pictures: the Schrödinger picture, the Heisenberg picture, and the interaction picture. The Kubo formula is derived by using the interaction picture.

Fig. 2.2: fig/ch2/haldane-disp.eps

In the Schrödinger picture, the state vector $|\psi(t)\rangle$ depends on time. The solution of the time-dependent Schrödinger equation,

$$i\hbar\partial_t|\psi(t)\rangle = \hat{H}|\psi(t)\rangle, \tag{2.17}$$

is given by

$$|\psi(t)\rangle = e^{-\frac{i}{\hbar}\hat{H}t}|\psi_0\rangle, \tag{2.18}$$

where the Hamiltonian $\hat{H}$ and the state vector at $t = 0$ $|\psi_0\rangle$ are time-independent. It is noted that any operator O may explicitly depend on time [90].

In the Heisenberg picture, on the other hand, all the time-dependence is assigned to operator O [90], thus the state vector and Hamiltonian do not depend on time. By using Eqs. (2.17) and (2.18), the expectation value of operator O is given by

$$\langle\psi'(t)|O|\psi'(t)\rangle = \langle\psi'_0|e^{+\frac{i}{\hbar}\hat{H}t}Oe^{-\frac{i}{\hbar}\hat{H}t}|\psi'_0\rangle \equiv \langle\psi'_0|O(t)|\psi'_0\rangle. \tag{2.19}$$

where $|\psi'_0\rangle \equiv e^{+\frac{i}{\hbar}\hat{H}t}|\psi'(t)\rangle$. By taking the time-derivative of $O(t)$, we obtain the Heisenberg equation of motion as follows:

$$\begin{aligned}\frac{d}{dt}O(t) &= e^{+\frac{i}{\hbar}\hat{H}t}\left(\frac{i}{\hbar}\hat{H}O + \partial_t O - \frac{i}{\hbar}O\hat{H}\right)e^{-\frac{i}{\hbar}\hat{H}t} \\ &= \frac{i}{\hbar}[\hat{H}, O(t)] + (\partial_t O)(t).\end{aligned} \tag{2.20}$$

As in the Schrödinger picture, the original operator $\hat{O}$ may be time-dependent. It is noted that both in the Schrödinger and the Heisenberg pictures, the Hamiltonian $\hat{H}$ is time-independent. In the case of time-dependent Hamiltonian, we have to adopt the interaction picture.

The interaction picture is useful to describe a perturbation of a time-independent state $|n_0\rangle$ with a time-dependent interaction [90], such as an interaction between electron and electric field of light. Hamiltonian in the interaction picture is given by

$$\hat{H}(t) = \hat{H}_0 + \hat{V}(t). \tag{2.21}$$

Here, $\hat{H}_0$ is time-independent part, which satisfies $\hat{H}_0|n_0\rangle = \epsilon_0|n_0\rangle$, and ϵ_0 is the energy eigenstate of $|n_0\rangle$. The perturbation is represented by the $\hat{V}(t)$ part. The state vector and operator in the interaction picture are given by

$$|\hat{\psi}(t)\rangle = e^{+\frac{i}{\hbar}\hat{H}_0 t}|\psi(t)\rangle, \tag{2.22}$$

and

$$\hat{O}(t) = e^{+\frac{i}{\hbar}\hat{H}_0 t}Oe^{-\frac{i}{\hbar}\hat{H}_0 t}, \tag{2.23}$$

respectively. Therefore, the interaction picture reduces to the Heisenberg picture when $\hat{V}(t) = 0$. The Schrödinger equation for the interaction picture is given by

$$i\hbar\partial_t|\hat{\psi}(t)\rangle = (-\hat{H}_0 + \hat{H})|\hat{\psi}(t)\rangle = \hat{V}(t)|\hat{\psi}(t)\rangle. \tag{2.24}$$

Therefore, the Schrödinger equation in the interaction picture only contains $\hat{V}(t)$. Let us consider the time-evolution of the state vector from t_0 to t in term of a unitary operator $\hat{U}(t,t_0)$, which satisfies

$$|\hat{\psi}(t)\rangle = \hat{U}(t,t_0)|\hat{\psi}(t_0)\rangle. \tag{2.25}$$

By using Eqs. (2.18) and (2.22), Eq. (2.25) becomes

$$e^{+\frac{i}{\hbar}\hat{H}_0 t}e^{-\frac{i}{\hbar}\hat{H}t}|\psi_0\rangle = \hat{U}(t,t_0)e^{+\frac{i}{\hbar}\hat{H}_0 t_0}e^{-\frac{i}{\hbar}\hat{H}t_0}|\psi_0\rangle. \tag{2.26}$$

Therefore, the explicit expression of $\hat{U}(t,t_0)$ is given by

$$\hat{U}(t,t_0) = e^{+\frac{i}{\hbar}\hat{H}_0 t}e^{-\frac{i}{\hbar}\hat{H}(t-t_0)}e^{-\frac{i}{\hbar}\hat{H}_0 t_0}. \tag{2.27}$$

The relation between $\hat{U}(t,t_0)$ and $\hat{V}(t)$ is given by the Schrödinger equation as follows:

$$i\hbar\partial_t\hat{U}(t,t_0) = \hat{V}(t)\hat{U}(t,t_0). \tag{2.28}$$

By integrating Eq. (2.28) from t_0 to t, we get

$$\hat{U}(t,t_0) - \hat{U}(t_0,t_0) = \frac{1}{i\hbar}\int_{t_0}^{t} dt'\hat{V}(t')\hat{U}(t',t_0). \tag{2.29}$$

From Eq. (2.25), it is clear that $\hat{U}(t_0,t_0) = \hat{1}$ is the identity operator. The integral equation in Eq. (2.29) can be solved iteratively as follows:

$$\begin{aligned}\hat{U}(t,t_0) &= \hat{1} + \frac{1}{i\hbar}\int_{t_0}^{t} dt'\hat{V}(t')\hat{U}(t',t_0) \\ &= \hat{1} + \frac{1}{i\hbar}\int_{t_0}^{t} dt'\hat{V}(t') + \frac{1}{(i\hbar)^2}\int_{t_0}^{t} dt'\hat{V}(t')\int_{t_0}^{t'} dt''\hat{V}(t'') + \dots .\end{aligned} \tag{2.30}$$

In the case that the perturbation $\hat{V}(t')$ is weak compared with $\hat{H}_0$, the expression of $\hat{U}(t,t_0)$ in Eq. (2.30) is approximated by the first order of $\hat{V}(t)$. This approximation corresponds to the linear response theory.

Let us consider the expectation value of operator O for a given temperature T. If we adopt the canonical distribution in statistical physics [90], $\langle O\rangle$ is given by

$$\langle O\rangle = \frac{1}{Z}\sum_n \langle n|O|n\rangle e^{-\beta\epsilon_n}, \tag{2.31}$$

where $Z \equiv \sum_n e^{-\beta\epsilon_n}$ is the partition function, ϵ_n is the eigenvalue of $\hat{H}_0$ in Eq. (2.21), and $\beta \equiv 1/(k_B T)$, where k_B is the Boltzmann constant. Suppose that a perturbation $\hat{V}(t)$ is applied at $t = t_0$ on the system. Since the eigenstate now depends on time and evolves according to Eq. (2.25), Eq. (2.31) becomes

$$\begin{aligned}\langle O\rangle(t) &= \frac{1}{Z}\sum_n \langle n(t)|O|n(t)\rangle e^{-\beta\epsilon_n} \\ &= \frac{1}{Z}\sum_n \langle \hat{n}(t)|e^{+\frac{i}{\hbar}\hat{H}_0 t}Oe^{-\frac{i}{\hbar}\hat{H}_0 t}|\hat{n}(t)\rangle e^{-\beta\epsilon_n}.\end{aligned} \tag{2.32}$$

In the second line of Eq. (2.32), we express $|n(t)\rangle$ in term of the state vector in the interaction picture according to Eq. (2.22). By using Eq. (2.25) to express the state vector at t_0, we get

$$\langle O\rangle(t) = \frac{1}{Z}\sum_n \langle \hat{n}(t_0)|\hat{U}^\dagger(t,t_0)e^{+\frac{i}{\hbar}\hat{H}_0 t}Oe^{-\frac{i}{\hbar}\hat{H}_0 t}\hat{U}(t,t_0)|\hat{n}(t_0)\rangle e^{-\beta\epsilon_n}. \tag{2.33}$$

By using the expression of $\hat{U}(t,t_0)$ in Eq. (2.30), and by keeping the linear order of $\langle V\rangle(t')$, we obtain

$$\begin{aligned}\langle O\rangle(t) &= \frac{1}{Z}\sum_n \Bigg\{ \langle \hat{n}(t_0)|e^{+\frac{i}{\hbar}\hat{H}_0 t}Oe^{-\frac{i}{\hbar}\hat{H}_0 t}|\hat{n}(t_0)\rangle \\ &\quad - \frac{i}{\hbar}\int_{t_0}^{t} dt' \langle \hat{n}(t_0)|\hat{O}(t)\hat{V}(t') - \hat{V}(t')\hat{O}(t)|\hat{n}(t_0)\rangle \Bigg\} e^{-\beta\epsilon_n} \\ &= \frac{1}{Z}\sum_n \left\{ \langle n(t_0)|\hat{O}|n(t_0)\rangle - \frac{i}{\hbar}\int_{t_0}^{t} dt' \langle \hat{n}(t_0)|[\hat{O}(t),\hat{V}(t')]|\hat{n}(t_0)\rangle \right\} e^{-\beta\epsilon_n}.\end{aligned} \tag{2.34}$$

It is noted that in first line of Eq. (2.34), the factors which depend on t in the second term are absorbed into the operator O [see Eq. (2.23)]. By definition, $|\hat{n}(t_0)\rangle = e^{+\frac{i}{\hbar}\hat{H}_0 t_0}|n(t_0)\rangle = |n\rangle$ [90]. Eq. (2.34) can be expressed in a simplified form as follows:

$$\langle O\rangle(t) = \langle O\rangle_0 - \frac{i}{\hbar}\int_{t_0}^{t} dt' \langle [\hat{O}(t),\hat{V}(t')]\rangle_0. \tag{2.35}$$

Eq. (2.35) is known as the Kubo formula. Here, the notation $\langle ...\rangle_0$ means average with respect to $\hat{H}_0$. Therefore, in a perturbed system, we only require the information of state vector before the perturbation is applied. In the next subsection, we derive the optical conductivity of 2D material by considering the expectation value of the current density $\langle \boldsymbol{J}\rangle(t)$.

2.2.2 Kubo formula for optical conductivity

Next, let us consider the Kubo formula for obtaining the optical conductivity. In the linear response theory, the operator for current density [90, 92] is given by

$$\begin{aligned}\hat{\boldsymbol{J}}(\boldsymbol{r},t) &= -e\Psi^\dagger(\boldsymbol{r},t)\hat{\boldsymbol{v}}\Psi(\boldsymbol{r},t) - \frac{e^2}{m}\Psi^\dagger(\boldsymbol{r},t)\Psi(\boldsymbol{r},t)\boldsymbol{A}(\boldsymbol{r},t) \\ &\equiv \hat{\boldsymbol{J}}^{(P)}(\boldsymbol{r},t) + \hat{\boldsymbol{J}}^{(D)}(\boldsymbol{r},t),\end{aligned} \tag{2.36}$$

where e is the elementary charge, m is effective mass of electron, $\hat{\boldsymbol{v}}$ is the velocity operator, $\boldsymbol{A}(\boldsymbol{r},t)$ is the vector potential from an electromagnetic wave, and $\Psi(\boldsymbol{r},t)$ is the field operator. The terms $\hat{\boldsymbol{J}}^{(P)}(\boldsymbol{r},t)$ and $\hat{\boldsymbol{J}}^{(D)}(\boldsymbol{r},t)$ are called the paramagnetic and diamagnetic current operators, respectively. The perturbation Hamiltonian due to the vector potential A_j is given by

$$\begin{aligned}\hat{V}(t') &= -\Theta(t-t')\int d\boldsymbol{r}'\hat{\boldsymbol{J}}(\boldsymbol{r}',t')\cdot\boldsymbol{A}(\boldsymbol{r}',t') \\ &\approx -\Theta(t-t')\int d\boldsymbol{r}'\hat{J}_j^{(P)}(\boldsymbol{r}',t')A_j(\boldsymbol{r}',t').\end{aligned} \tag{2.37}$$

The step function of time $\Theta(t-t')$ is used because we assume that the perturbation from the electromagnetic wave reaches the 2D material at $t = t'$. We neglect the perturbation from $\hat{\boldsymbol{J}}^{(D)}$ for a relatively small A_j because it consists of non-linear term ${A_j}^2$. By substituting Eq. (2.37) into the Kubo formula [Eq. (2.35)], the expectation value of current in the i-direction becomes

$$\langle J_i(\boldsymbol{r})\rangle(t) = \langle J_i\rangle_0 - \int_{t_0}^{t} dt' \int d\boldsymbol{r}' C^R_{J_iJ_j}(\boldsymbol{r},\boldsymbol{r}',t-t')A_j(\boldsymbol{r}',t'), \tag{2.38}$$

where we define the retarded current-current correlation function as follows:

$$C^R_{J_iJ_j}(\boldsymbol{r},\boldsymbol{r}',t-t') \equiv -\frac{i}{\hbar}\Theta(t-t')\left\langle\left[\hat{J}_i^{(P)}(\boldsymbol{r},t),\hat{J}_j^{(P)}(\boldsymbol{r}',t')\right]\right\rangle_0. \tag{2.39}$$

By assuming that the electromagnetic wave is a plane wave with angular frequency ω, and by expressing $A_j(\boldsymbol{r}',t') = A_j(\boldsymbol{r}')e^{-i\omega t'}$ in term of electric field $E_j(\boldsymbol{r}',t') = -\partial_{t'}A_j(\boldsymbol{r}',t') = i\omega A_j(\boldsymbol{r}',t')$, Eq. (2.38) becomes

$$\langle J_i(\boldsymbol{r})\rangle(t) = -\frac{1}{i\omega}\int_{t_0}^{t} dt' \int d\boldsymbol{r}' C^R_{J_iJ_j}(\boldsymbol{r},\boldsymbol{r}',t-t')E_j(\boldsymbol{r}',t'). \tag{2.40}$$

Here, we set $\langle J_i\rangle_0 = 0$ because we assume that there is no current in the unperturbed system. By considering that the perturbation is applied for a long time, we let $t \to +\infty$ and $t_0 \to -\infty$. The integral with respect to t' is solved by the convolution theorem, as follows:

$$\int_{-\infty}^{+\infty} dt' f(t-t')g(t') = f(\omega)g(\omega). \tag{2.41}$$

Therefore, by applying Eq. (2.41) to Eq. (2.40), the expectation value of the current in frequency domain is given by

$$\langle J_i(\boldsymbol{r})\rangle(\omega) = -\frac{1}{i\omega}\int d\boldsymbol{r}' C^R_{J_iJ_j}(\boldsymbol{r},\boldsymbol{r}',\omega)E_j(\boldsymbol{r}',\omega). \tag{2.42}$$

By comparing Eq. (2.42) with the Ohm law,

$$\langle J_i(\boldsymbol{r})\rangle(\omega) = \int d\boldsymbol{r}'\sigma_{ij}(\boldsymbol{r},\boldsymbol{r}',\omega)E_j(\boldsymbol{r}',\omega), \tag{2.43}$$

the optical conductivity is related by the current-current correlation function by

$$\sigma_{ij}(\boldsymbol{r},\boldsymbol{r}',\omega) = -\frac{1}{i\omega}C^R_{J_iJ_j}(\boldsymbol{r},\boldsymbol{r}',\omega). \tag{2.44}$$

The next step for obtaining σ_{ij} is to find the explicit formula for $C^R_{J_iJ_j}(\boldsymbol{r},\boldsymbol{r}',\omega)$. Let us return to the expression of the correlation function in time domain. By expressing the current operator in Eq. (2.39) by the Fourier transform,

$$\hat{\boldsymbol{J}}^{(P)}(\boldsymbol{r},t) = \frac{1}{\sqrt{L^2}}\sum_{\boldsymbol{k}}\hat{\boldsymbol{J}}^{(P)}(\boldsymbol{k},t)e^{i\boldsymbol{k}\cdot\boldsymbol{r}}, \tag{2.45}$$

we get

$$C^R_{J_iJ_j}(\boldsymbol{r},\boldsymbol{r}',t-t') = -\frac{i}{\hbar}\Theta(t-t')\frac{1}{L^2}\sum_{\boldsymbol{k},\boldsymbol{k}'}\left\langle\left[\hat{J}^{(P)}_i(\boldsymbol{k},t),\hat{J}^{(P)}_j(\boldsymbol{k}',t')\right]\right\rangle_0 e^{i\boldsymbol{k}\cdot\boldsymbol{r}}e^{i\boldsymbol{k}'\cdot\boldsymbol{r}'}$$
$$= -\frac{i}{\hbar}\Theta(t-t')\frac{1}{L^2}\sum_{\boldsymbol{k},\boldsymbol{k}'}\left\langle\left[\hat{J}^{(P)}_i(\boldsymbol{k},t),\hat{J}^{(P)}_j(\boldsymbol{k}',t')\right]\right\rangle_0 e^{i(\boldsymbol{k}+\boldsymbol{k}')\cdot\boldsymbol{r}'}e^{i\boldsymbol{k}\cdot(\boldsymbol{r}-\boldsymbol{r}')}, \tag{2.46}$$

where L^2 is the area of the 2D material. In the second line of Eq. (2.46), we multiply the right-hand side with $e^{i\boldsymbol{k}\cdot\boldsymbol{r}'}e^{-i\boldsymbol{k}\cdot\boldsymbol{r}'}$ and rearrange the terms inside the exponential function in order to determine the relation between $\boldsymbol{k}$ and $\boldsymbol{k}'$. By defining a translational vector $\boldsymbol{R}$, and transform $\boldsymbol{r}\to\boldsymbol{r}+\boldsymbol{R}$ and $\boldsymbol{r}'\to\boldsymbol{r}'+\boldsymbol{R}$, Eq. (2.46) becomes

$$C^R_{J_iJ_j}(\boldsymbol{r}+\boldsymbol{R},\boldsymbol{r}'+\boldsymbol{R},t-t') = -\frac{i}{\hbar}\Theta(t-t')\frac{1}{L^2}\sum_{\boldsymbol{k},\boldsymbol{k}'}\left\langle\left[\hat{J}^{(P)}_i(\boldsymbol{k},t),\hat{J}^{(P)}_j(\boldsymbol{k}',t')\right]\right\rangle_0$$
$$\times\, e^{i(\boldsymbol{k}+\boldsymbol{k}')\cdot\boldsymbol{r}'}e^{i(\boldsymbol{k}+\boldsymbol{k}')\cdot\boldsymbol{R}}e^{i\boldsymbol{k}\cdot(\boldsymbol{r}-\boldsymbol{r}')}. \tag{2.47}$$

Because of the translational invariance, $C^R_{J_iJ_j}(\boldsymbol{r},\boldsymbol{r}',t-t') = C^R_{J_iJ_j}(\boldsymbol{r}+\boldsymbol{R},\boldsymbol{r}'+\boldsymbol{R},t-t')$ must be satisfied, which implies $e^{i(\boldsymbol{k}+\boldsymbol{k}')\cdot\boldsymbol{R}}=1$ and thus $\boldsymbol{k}'=-\boldsymbol{k}$. Eq. (2.46) becomes

$$C^R_{J_iJ_j}(\boldsymbol{r},\boldsymbol{r}',t-t') = \frac{1}{L^2}\sum_{\boldsymbol{k}}C^R_{J_iJ_j}(\boldsymbol{k},t-t')e^{i\boldsymbol{k}\cdot(\boldsymbol{r}-\boldsymbol{r}')}, \tag{2.48}$$

where we define

$$C^R_{J_iJ_j}(\boldsymbol{k},t-t') \equiv -\frac{i}{\hbar}\Theta(t-t')\left\langle\left[\hat{J}^{(P)}_i(\boldsymbol{k},t),\hat{J}^{(P)}_j(-\boldsymbol{k},t')\right]\right\rangle_0. \tag{2.49}$$

Let us find the explicit form of the current operator in Eqs. (2.49). Eq. (2.36) states that $\boldsymbol{J}^{(P)}$ is expressed in term of the field operators $\Psi(\boldsymbol{r},t)$ and $\Psi^\dagger(\boldsymbol{r},t)$. The definition of $\Psi(\boldsymbol{r},t)$ ($\Psi^\dagger(\boldsymbol{r},t)$) is an operator which annihilates (creates) an electron at position $\boldsymbol{r}$ [91], as follows:

$$\Psi(\boldsymbol{r},t) = \sum_\nu\langle\boldsymbol{r}|\nu\rangle c_\nu(t), \qquad \Psi^\dagger(\boldsymbol{r},t) = \sum_\nu\langle\boldsymbol{r}|\nu\rangle^* c^\dagger_\nu(t), \tag{2.50}$$

where the state vector $|\nu\rangle$ does not depend on time, and the time-dependence is assigned to annihilation operator $c_\nu(t)$. The state of electron in solid depends on the band index β and wave vector $\boldsymbol{\kappa}$. By choosing $\langle\boldsymbol{r}|\nu\rangle = (1/\sqrt{L^2})|\beta,\boldsymbol{\kappa}\rangle e^{i\boldsymbol{\kappa}\cdot\boldsymbol{r}}$, $\Psi(\boldsymbol{r},t)$ and $\Psi^\dagger(\boldsymbol{r},t)$ are given by

$$\Psi(\boldsymbol{r},t) = \frac{1}{\sqrt{L^2}}\sum_{\beta,\boldsymbol{\kappa}}|\beta,\boldsymbol{\kappa}\rangle c_{\beta\boldsymbol{\kappa}}(t)e^{i\boldsymbol{\kappa}\cdot\boldsymbol{r}}, \quad \Psi^\dagger(\boldsymbol{r},t) = \frac{1}{\sqrt{L^2}}\sum_{\beta',\boldsymbol{\kappa}'}\langle\beta',\boldsymbol{\kappa}'|c^\dagger_{\beta'\boldsymbol{\kappa}'}(t)e^{-i\boldsymbol{\kappa}'\cdot\boldsymbol{r}}. \tag{2.51}$$

By substituting Eq. (2.51) to Eq. (2.36), the current operator is given by

$$\hat{\boldsymbol{J}}^{(P)}(\boldsymbol{r},t) = -\frac{e}{L^2}\sum_{\beta,\beta'}\sum_{\boldsymbol{\kappa},\boldsymbol{\kappa}'}\langle\beta',\boldsymbol{\kappa}'|\hat{\boldsymbol{v}}|\beta,\boldsymbol{\kappa}\rangle c^\dagger_{\beta'\boldsymbol{\kappa}'}(t)c_{\beta\boldsymbol{\kappa}}(t)e^{i(\boldsymbol{\kappa}-\boldsymbol{\kappa}')\cdot\boldsymbol{r}}. \tag{2.52}$$

By letting $\boldsymbol{\kappa} - \boldsymbol{\kappa}' = \boldsymbol{k}$, and by using the Fourier transform of the current operator in Eq. (2.45), $\hat{J}_i^{(P)}(\boldsymbol{k})$ and $\hat{J}_j^{(P)}(-\boldsymbol{k})$ in Eq. (2.49) are given by

$$\begin{aligned}\hat{J}_i^{(P)}(\boldsymbol{k},t) &= \frac{-e}{\sqrt{L^2}}\sum_{B,B'}\sum_{\boldsymbol{Q}}\langle B',\boldsymbol{Q}-\boldsymbol{k}|\hat{v}_i|B,\boldsymbol{Q}\rangle c^\dagger_{B'\boldsymbol{Q}-\boldsymbol{k}}(t)c_{B\boldsymbol{Q}}(t),\\ \hat{J}_j^{(P)}(-\boldsymbol{k},t') &= \frac{-e}{\sqrt{L^2}}\sum_{b,b'}\sum_{\boldsymbol{q}}\langle b',\boldsymbol{q}+\boldsymbol{k}|\hat{v}_j|B,\boldsymbol{q}\rangle c^\dagger_{b'\boldsymbol{q}+\boldsymbol{k}}(t')c_{b\boldsymbol{q}}(t').\end{aligned} \tag{2.53}$$

By substituting Eq. (2.53) to Eq. (2.49), we get

$$\begin{aligned}C^R_{J_iJ_j}(\boldsymbol{k},t-t') = &-\frac{ie^2}{\hbar L^2}\Theta(t-t')\sum_{B,B',b,b'}\sum_{\boldsymbol{Q},\boldsymbol{q}}\langle B',\boldsymbol{Q}-\boldsymbol{k}|\hat{v}_i|B,\boldsymbol{Q}\rangle\langle b',\boldsymbol{q}+\boldsymbol{k}|\hat{v}_j|b,\boldsymbol{q}\rangle\\ &\times\left\langle\left[c^\dagger_{B'\boldsymbol{Q}-\boldsymbol{k}}(t)c_{B\boldsymbol{Q}}(t),c^\dagger_{b'\boldsymbol{q}+\boldsymbol{k}}(t')c_{b\boldsymbol{q}}(t')\right]\right\rangle_0.\end{aligned} \tag{2.54}$$

The commutator $\langle[...]\rangle_0$ in Eq. (2.54) can be expanded by a formula in which for given operators A, B, C and D, the commutator $[AB,CD]$ is expressed by anti-commutators as follows:

$$[AB,CD] = -AC\{D,B\} + A\{C,B\}D - C\{D,A\}B + \{C,A\}DB. \tag{2.55}$$

By applying Eq. (2.55) to on the commutator in Eq. (2.54), we get

$$\begin{aligned}\left[c^\dagger_{B'\boldsymbol{Q}-\boldsymbol{k}}(t)c_{B\boldsymbol{Q}}(t),c^\dagger_{b'\boldsymbol{q}+\boldsymbol{k}}(t')c_{b\boldsymbol{q}}(t')\right] = &-c^\dagger_{B'\boldsymbol{Q}-\boldsymbol{k}}(t)c^\dagger_{b'\boldsymbol{q}+\boldsymbol{k}}(t')\left\{c_{b\boldsymbol{q}}(t'),c_{B\boldsymbol{Q}}(t)\right\}\\ &+c^\dagger_{B'\boldsymbol{Q}-\boldsymbol{k}}(t)\left\{c^\dagger_{b'\boldsymbol{q}+\boldsymbol{k}}(t'),c_{B\boldsymbol{Q}}(t)\right\}c_{b\boldsymbol{q}}(t')\\ &-c^\dagger_{b'\boldsymbol{q}+\boldsymbol{k}}(t')\left\{c_{b\boldsymbol{q}}(t'),c^\dagger_{B'\boldsymbol{Q}-\boldsymbol{k}}(t)\right\}c_{B\boldsymbol{Q}}(t)\\ &+\left\{c^\dagger_{b'\boldsymbol{q}+\boldsymbol{k}}(t'),c^\dagger_{B'\boldsymbol{Q}-\boldsymbol{k}}(t)\right\}c_{b\boldsymbol{q}}(t')c_{B\boldsymbol{Q}}(t).\end{aligned} \tag{2.56}$$

To simplify the left-hand side of Eq. (2.56), first we need to consider the time-dependence of the creation and annihilation operators [90]. Let us define a Hamiltonian which is diagonal in the $|\nu\rangle$ basis, $\hat{H} \equiv \sum_\nu \epsilon_\nu c^\dagger_\nu c_\nu$, where ϵ_ν is the energy of state $|\nu\rangle$. By applying the Heisenberg picture [Eq. (2.19)] on operator c_ν, we get

$$c_\nu(t) = e^{+\frac{i}{\hbar}\hat{H}t}c_\nu e^{-\frac{i}{\hbar}\hat{H}t}. \tag{2.57}$$

By using the Heisenberg equation of motion [Eq. (2.20)], the time derivative of $c(t)$ is given by

$$\frac{d}{dt}c_\nu(t) = \frac{i}{\hbar}e^{+\frac{i}{\hbar}\hat{H}t}\sum_{\nu'}\epsilon_{\nu'}[c^\dagger_{\nu'}c_{\nu'},c_\nu]e^{-\frac{i}{\hbar}\hat{H}t}. \tag{2.58}$$

By using the identity

$$[AB,C] = A\{B,C\} - \{A,C\}B, \tag{2.59}$$

Eq. (2.58) becomes

$$\frac{d}{dt}c_\nu(t) = \frac{i}{\hbar}\sum_{\nu'}\epsilon_{\nu'}\Big(c^\dagger_{\nu'}(t)\Big\{c_{\nu'}, c_\nu\Big\} - \Big\{c^\dagger_{\nu'}, c_\nu\Big\}c_{\nu'}(t)\Big). \tag{2.60}$$

The anti-commutator for fermions satisfies the following relations:

$$\Big\{c_\nu, c_{\nu'}\Big\} = 0,\ \Big\{c^\dagger_\nu, c^\dagger_{\nu'}\Big\} = 0,\ \Big\{c^\dagger_\nu, c_{\nu'}\Big\} = \Big\{c_\nu, c^\dagger_{\nu'}\Big\} = \delta_{\nu,\nu'}. \tag{2.61}$$

By using Eq. (2.61), only the second term in the left-hand side of Eq. (2.60) survives. By integrating Eq. (2.60) with respect to t, $c_\nu(t)$ and its conjugate $c^\dagger_\nu(t)$ are given by

$$c_\nu(t) = e^{-i\epsilon_\nu t/\hbar}c_\nu, \qquad c^\dagger_\nu(t) = e^{+i\epsilon_\nu t/\hbar}c^\dagger_\nu. \tag{2.62}$$

Now, let us apply Eq. (2.61) to the left-hand side of Eq. (2.56). Here, only the second and third terms in the left-hand side of Eq. (2.56) survive. Because of $\delta_{\nu,\nu'}$, we get $B = b'$, $B' = b$, and $\boldsymbol{Q} = \boldsymbol{q} + \boldsymbol{k}$. Thus, Eq. (2.56) becomes

$$\begin{aligned}\Big[c^\dagger_{B'\boldsymbol{Q}-\boldsymbol{k}}(t)c_{B\boldsymbol{Q}}(t), c^\dagger_{b'\boldsymbol{q}+\boldsymbol{k}}(t')c_{b\boldsymbol{q}}(t')\Big] &= e^{+\frac{i}{\hbar}\epsilon_{b\boldsymbol{q}}t}c^\dagger_{b\boldsymbol{q}}\Big[e^{-\frac{i}{\hbar}\epsilon_{b'\boldsymbol{q}+\boldsymbol{k}}(t-t')}\Big]e^{-\frac{i}{\hbar}\epsilon_{b\boldsymbol{q}}t'}c_{b\boldsymbol{q}} \\ &\quad - e^{+\frac{i}{\hbar}\epsilon_{b'\boldsymbol{q}+\boldsymbol{k}}t'}c^\dagger_{b'\boldsymbol{q}+\boldsymbol{k}}\Big[e^{+\frac{i}{\hbar}\epsilon_{b\boldsymbol{q}}(t-t')}\Big]e^{-\frac{i}{\hbar}\epsilon_{b'\boldsymbol{q}+\boldsymbol{k}}t}c_{b'\boldsymbol{q}+\boldsymbol{k}} \\ &= \Big[c^\dagger_{b\boldsymbol{q}}c_{b\boldsymbol{q}} - c^\dagger_{b'\boldsymbol{q}+\boldsymbol{k}}c_{b'\boldsymbol{q}+\boldsymbol{k}}\Big]e^{+\frac{i}{\hbar}(\epsilon_{b\boldsymbol{q}}-\epsilon_{b'\boldsymbol{q}+\boldsymbol{k}})(t-t')} \\ &= [n_{b\boldsymbol{q}} - n_{b'\boldsymbol{q}+\boldsymbol{k}}]e^{+\frac{i}{\hbar}(\epsilon_{b\boldsymbol{q}}-\epsilon_{b'\boldsymbol{q}+\boldsymbol{k}})(t-t')},\end{aligned} \tag{2.63}$$

where $n_\nu = c^\dagger_\nu c_\nu$ is the number operator. By substituting Eq. (2.63) into Eq. (2.54), we get

$$\begin{aligned}C^R_{J_iJ_j}(\boldsymbol{k}, t-t') &= -\frac{ie^2}{\hbar L^2}\Theta(t-t')\sum_{b,b'}\sum_{\boldsymbol{q}}\langle b,\boldsymbol{q}|\hat{v}_i|b',\boldsymbol{q}+\boldsymbol{k}\rangle\langle b',\boldsymbol{q}+\boldsymbol{k}|\hat{v}_j|b,\boldsymbol{q}\rangle \\ &\quad\times\langle n_{b\boldsymbol{q}} - n_{b'\boldsymbol{q}+\boldsymbol{k}}\rangle_0 e^{+\frac{i}{\hbar}(\epsilon_{b\boldsymbol{q}}-\epsilon_{b'\boldsymbol{q}+\boldsymbol{k}})(t-t')} \\ &= -\frac{ie^2}{\hbar L^2}\Theta(t-t')\sum_{b,b'}\sum_{\boldsymbol{q}}\langle b,\boldsymbol{q}|\hat{v}_i|b',\boldsymbol{q}+\boldsymbol{k}\rangle\langle b',\boldsymbol{q}+\boldsymbol{k}|\hat{v}_j|b,\boldsymbol{q}\rangle \\ &\quad\times[f(\epsilon_{b\boldsymbol{q}}) - f(\epsilon_{b'\boldsymbol{q}+\boldsymbol{k}})]e^{+\frac{i}{\hbar}(\epsilon_{b\boldsymbol{q}}-\epsilon_{b'\boldsymbol{q}+\boldsymbol{k}})(t-t')}.\end{aligned} \tag{2.64}$$

In the second line of Eq. (2.64), we use the fact that the average of number operator is the Fermi-Dirac distribution function, i.e. $\langle n_\nu - n_{\nu'}\rangle_0 = \langle n_\nu\rangle_0 - \langle n_{\nu'}\rangle_0 = f(\epsilon_\nu) - f(\epsilon_{\nu'})$.

The retarded correlation function in the k and frequency domains is obtained by the Fourier transform of Eq. (2.64), as follows [90]:

$$C^R_{J_iJ_j}(\boldsymbol{k},\omega) = \int_{-\infty}^{+\infty} dt\ C^R_{J_iJ_j}(\boldsymbol{k}, t-t')e^{i(\omega+i\gamma)(t-t')}. \tag{2.65}$$

Here, we include $\gamma > 0$ to make the Fourier transform converges. Physically, γ is a damping constant, which is the inverse of the relaxation time of electron. By substi-

tuting Eq. (2.64) to Eq. (2.65), we get

$$C^R_{J_iJ_j}(\boldsymbol{k},\omega) = -\frac{ie^2}{\hbar L^2}\sum_{b,b'}\sum_{\boldsymbol{q}}\langle b,\boldsymbol{q}|\hat{v}_i|b',\boldsymbol{q}+\boldsymbol{k}\rangle\langle b',\boldsymbol{q}+\boldsymbol{k}|\hat{v}_j|b,\boldsymbol{q}\rangle[f(\epsilon_{b\boldsymbol{q}}) - f(\epsilon_{b'\boldsymbol{q}+\boldsymbol{k}})] \times \int_{-\infty}^{+\infty} dt\Theta(t-t')e^{+\frac{i}{\hbar}(\epsilon_{b\boldsymbol{q}}-\epsilon_{b'\boldsymbol{q}+\boldsymbol{k}}+\hbar\omega+i\hbar\gamma)(t-t')}. \tag{2.66}$$

The integral in Eq. (2.66) is given by

$$\begin{aligned}\int_{-\infty}^{+\infty} dt\Theta(t-t')e^{+\frac{i}{\hbar}(\epsilon_{b\boldsymbol{q}}-\epsilon_{b'\boldsymbol{q}+\boldsymbol{k}}+\hbar\omega+i\hbar\gamma)(t-t')} &= \int_0^{+\infty} dte^{+\frac{i}{\hbar}(\epsilon_{b\boldsymbol{q}}-\epsilon_{b'\boldsymbol{q}+\boldsymbol{k}}+\hbar\omega+i\hbar\gamma)(t-t')} \\ &= \frac{i\hbar}{\epsilon_{b\boldsymbol{q}}-\epsilon_{b'\boldsymbol{q}+\boldsymbol{k}}+\hbar\omega+i\hbar\gamma}.\end{aligned} \tag{2.67}$$

By substituting Eq. (2.67) into Eq. (2.66), $C^R_{J_iJ_j}(\boldsymbol{k},\omega)$ is given as follows:

$$C^R_{J_iJ_j}(\boldsymbol{k},\omega) = \frac{e^2}{L^2}\sum_{b,b'}\sum_{\boldsymbol{q}}\langle b,\boldsymbol{q}|v_i|b',\boldsymbol{q}+\boldsymbol{k}\rangle\langle b',\boldsymbol{q}+\boldsymbol{k}|v_j|b,\boldsymbol{q}\rangle\frac{f(\epsilon_{b\boldsymbol{q}}) - f(\epsilon_{b'\boldsymbol{q}+\boldsymbol{k}})}{\epsilon_{b\boldsymbol{q}}-\epsilon_{b'\boldsymbol{q}+\boldsymbol{k}}+\hbar\omega+i\hbar\gamma}. \tag{2.68}$$

Let us return back to Eq. (2.43), in which optical conductivity in the real-space is given in term of the current-current correlation function. The same relation also holds in the k-space. Nevertheless, we need to exclude the contribution of the direct current (dc) which is given by setting $\omega = 0$ [92] in Eq. (2.68), because when $\omega = 0$, the vector potential is constant, which means that the electric field and current become zero. The optical conductivity is therefore given by

$$\sigma_{ij}(\boldsymbol{k},\omega) = -\frac{1}{i\omega}[C^R_{J_iJ_j}(\boldsymbol{k},\omega) - C^R_{J_iJ_j}(\boldsymbol{k},0)]. \tag{2.69}$$

By substituting Eq. (2.69) into Eq. (2.68), and by transforming the summation of $\boldsymbol{q}$ into an integral, $L^{-2}\sum_{\boldsymbol{q}} \to (2\pi)^{-2}\int d^2\boldsymbol{q}$ for 2D materials, we derive the final expression of the optical conductivity as follows:

$$\sigma_{ij}(\boldsymbol{k},\omega) = -ie^2\hbar\sum_{b,b'}\int\frac{d^2\boldsymbol{q}}{(2\pi)^2}\frac{f[\epsilon_b(\boldsymbol{q})] - f[\epsilon_{b'}(\boldsymbol{q}+\boldsymbol{k})]}{\epsilon_b(\boldsymbol{q}) - \epsilon_{b'}(\boldsymbol{q}+\boldsymbol{k})} \times \frac{\langle b,\boldsymbol{q}|\hat{v}_i|b',\boldsymbol{q}+\boldsymbol{k}\rangle\langle b',\boldsymbol{q}+\boldsymbol{k}|\hat{v}_j|b,\boldsymbol{q}\rangle}{\epsilon_b(\boldsymbol{q}) - \epsilon_{b'}(\boldsymbol{q}+\boldsymbol{k}) + \hbar\omega + i\hbar\gamma}, \tag{2.70}$$

where $i,j = x,y$, $\epsilon_b(\boldsymbol{q}) \equiv \epsilon_{b\boldsymbol{q}}$ and $\epsilon_{b'}(\boldsymbol{q}) \equiv \epsilon_{b'\boldsymbol{q}}$ are the energy dispersions of electrons. It is noted that $\boldsymbol{k}$ is the momentum of photon in the electronic transition from the b-th to the b'-th band. In Chapter 4, we use Eq. (2.70) to calculate longitudinal ($i = j$) and transversal/Hall ($i \neq j$) conductivities of the Haldane model for both intraband ($b = b'$) and interband ($b \neq b'$) contributions.

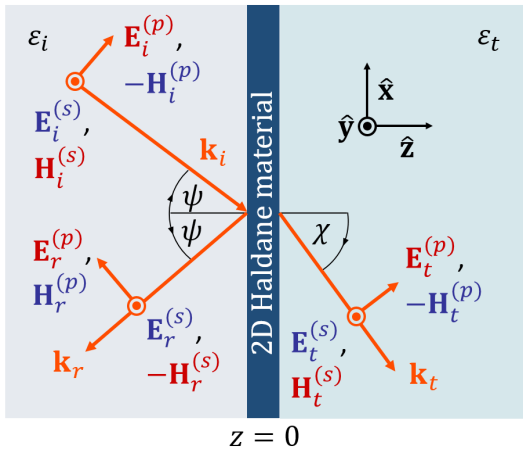

Figure 2.3 Electric and magnetic fields of light in the geometry consisting of the 2D Haldane material between two dielectric media, whose relative permittivities are given by ε_i and ε_t. The angles of incidence and transmission are given by ψ and χ, respectively. The red (blue) color indicates that the components of the electric and magnetic fields depend on p_m (s'_m).

2.3 Optical spectra 2D material

In this section, we describemethods to calculate the optical properties, which include optical absorption probability, as well as the Faraday and the Kerr rotations in the 2D Haldane material. We begin discussion by introducing notations for electromagnetic fields. The notations are adopted to express the absorption probability, as well as rotation and ellipticity angles of the electric field.

2.3.1 Optical absorption probability

In this thesis, the 2D Haldane material is treated as a conducting interface between two dielectric media as shown in Fig. 2.3. We assume that the thickness of the 2D material is negligible, and therefore we need to solve the boundary conditions of the Maxwell equations at the interface. In Fig. 2.3, we show the geometry for solving the boundary conditions. Here, the 2D material is placed in the xy plane at $z = 0$, and the propagation direction of light exists in the xz plane. The relative permittivity of the medium for incident (transmitted) light is denoted by ε_i (ε_t). The incident light comes with an angle of incidence ψ and is refracted by angle χ. The angles ψ and χ are related by the Snell law,

$$\sqrt{\varepsilon_i}\sin\psi = \sqrt{\varepsilon_t}\sin\chi. \tag{2.71}$$

The electric field in each medium is denoted by $\boldsymbol{E}_m$, where $m = i,\ t,\ r$ indicates the incident, transmitted, and reflected lights, respectively. In general, $\boldsymbol{E}_m$ can be decomposed into independent fields with p- and s-polarizations, $\boldsymbol{E}_m^{(p)}$ and $\boldsymbol{E}_m^{(s)}$, respectively,

Fig. 2.3: fig/ch2/fresnel2.eps

as follows:

$$\boldsymbol{E}_m = \boldsymbol{E}_m^{(p)} + \boldsymbol{E}_m^{(s)} = E_m^{(p)}\hat{\boldsymbol{p}}_m + E_m^{(s)}\hat{\boldsymbol{s}}_m, \tag{2.72}$$

where $\hat{\boldsymbol{p}}_m$ ($\hat{\boldsymbol{s}}_m$) is unit vector in the direction of the p- (s-) component of electric field. When we assume a plane wave of light with wave vector $\boldsymbol{k}_m$ and angular of momentum ω_m, $E_m^{(p)}$ and $E_m^{(s)}$ can be expressed by

$$E_m^{(p)} = E_0 p_m e^{i(\boldsymbol{k}_m\cdot\boldsymbol{r}-\omega_m t)}, \quad E_m^{(s)} = E_0 s_m e^{i(\boldsymbol{k}_m\cdot\boldsymbol{r}-\omega_m t+\Phi_m)}, \tag{2.73}$$

where E_0 and Φ_m are a common amplitude and the phase difference between p- and s-polarized fields, respectively. In the representation of the Jones vector, $\boldsymbol{E}_m$ is given as follows:

$$\boldsymbol{E}_m = E_0 \begin{pmatrix} p_m \\ s_m e^{i\Phi_m} \end{pmatrix} \equiv E_0 \begin{pmatrix} p_m \\ s'_m \end{pmatrix}, \tag{2.74}$$

Hence, the amplitude of electric field in the medium m is given by $E_0\sqrt{|p_m|^2+|s'_m|^2}$. To make sure that the incident light has magnitude E_0, we choose p_i and s_i such that $|p_i|^2 + |s'_i|^2 = 1$. In particular, for incident left-handed (right-handed) circularly-polarized lights, $\Phi_i = +\pi/2$ ($\Phi_i = -\pi/2$), $p_i = 1/\sqrt{2}$ ($p_i = 1/\sqrt{2}$), and $s'_i = +i/\sqrt{2}$ ($-i/\sqrt{2}$).

The direction and magnitude of magnetic field are given by applying the Faraday law on Eq. (2.73) as follows:

$$i\boldsymbol{k}_m \times \boldsymbol{E}_m = i\omega_m\mu_m\mu_0\boldsymbol{H}_m, \tag{2.75}$$

where $\mu_m \approx 1$ is the relative permeability of the dielectric medium m. Because of the cross product $\boldsymbol{k}_m \times \boldsymbol{E}_m$, $\boldsymbol{E}_m^{(p)}$ and $\boldsymbol{E}_m^{(s)}$ give rise to $\boldsymbol{H}_m^{(s)}$ and $\boldsymbol{H}_m^{(p)}$, respectively, as illustrated in Fig. 2.3. By using Eq. (2.75), we get

$$H_m^{(s)} = \frac{E_m^{(p)}}{Z_m}, \quad H_m^{(p)} = \frac{E_m^{(s)}}{Z_m}, \tag{2.76}$$

where $Z_m = \omega_m\mu_0/k_m$ is the impedance of electromagnetic wave. For convenience, we express $Z_m = Z_0/\sqrt{\varepsilon_m}$, where $Z_0 = \sqrt{\mu_0/\varepsilon_0} = 376.73\ \Omega$ is impedance of the vacuum.

The boundary conditions at $z = 0$ are obtained by using the Faraday and the Ampere laws. Here, the electric fields are continuous at the interface, while the magnetic field are discontinuous because of the induced current in the 2D materials. The relations between the p- and s- components of the electromagnetic fields are given by

$$E_i^{(p)}\cos\psi + E_r^{(p)}\cos\psi = E_t^{(p)}\cos\chi, \tag{2.77}$$

$$H_t^{(s)} - [H_i^{(s)} - H_r^{(s)}] = -[\sigma_{xx}(\omega)E_t^{(p)}\cos\chi + \sigma_{xy}(\omega)E_t^{(s)}], \tag{2.78}$$

$$E_i^{(s)} + E_r^{(s)} = E_t^{(s)}, \tag{2.79}$$

and

$$-H_t^{(p)}\cos\chi - [-H_i^{(p)}\cos\psi + H_r^{(p)}\cos\psi] = \sigma_{yy}(\omega)E_t^{(s)} + \sigma_{yx}(\omega)E_t^{(p)}\cos\chi. \tag{2.80}$$

From Eqs. (2.78) and (2.80), we can see that s- and p-components of the electric field are mixed each other by non-zero Hall conductivities $\sigma_{xy}(\omega)$ and $\sigma_{yx}(\omega)$. By expressing the dependence of the electric fields $E_m^{(p)}$ and $E_m^{(s)}$ as well as the magnetic fields $H_m^{(p)}$ and $H_m^{(s)}$ in Eqs. (2.77)-(2.80) in terms of p_m and ${s'}_m$, we have

$$p_i \cos\psi + p_r \cos\psi = p_t \cos\chi, \tag{2.81}$$

$$\frac{p_i}{Z_i} - \frac{p_r}{Z_i} = p_t \left[\frac{1}{Z_t} + \sigma_{xx}(\omega)\cos\chi \right] + {s'}_t \sigma_{xy}(\omega), \tag{2.82}$$

$${s'}_i + {s'}_r = {s'}_t, \tag{2.83}$$

and

$${s'}_i \frac{\cos\psi}{Z_i} - {s'}_r \frac{\cos\psi}{Z_i} = {s'}_t \left[\frac{\cos\chi}{Z_t} + \sigma_{yy}(\omega) \right] + p_t \sigma_{yx}(\omega)\cos\chi. \tag{2.84}$$

Therefore, there are four unknown variables (p_r, p_t, s'_r, and s'_t) to be solved in Eqs.(2.81)-(2.84) for given p_i and s'_i from the incoming light. Let us define a variable ξ_m as the ratio of s'_m to p_m as follows:

$$\xi_m \equiv \frac{s'_m}{p_m} = \frac{s_m}{p_m} e^{i\Phi_m}. \tag{2.85}$$

By defining ξ_m, we only will solve two variables (ξ_r and ξ_t) in the boundary conditions. The relations between ξ_r, ξ_t and ξ_i will be given in Chapter 4. Furthermore, we will discuss how the variable ξ_m is useful in obtaining the absorption spectra as well as the Faraday and the Kerr rotations in the 2D material.

The power of an electromagnetic wave per unit area is represented by the Poynting vector as follows:

$$\boldsymbol{S}_m = \frac{1}{2}[\boldsymbol{E}_m \times \boldsymbol{H}_m^*], \tag{2.86}$$

where the prefactor 1/2 is given because we consider the averaged intensity over the period of an oscillation. The direction of $\boldsymbol{S}_m$ is the same as that of the wavevector $\boldsymbol{k}_m$. Let us derive the intensity of an electromagnetic wave in the direction normal to the 2D material. Intensity for the incoming wave $I_i = \boldsymbol{S}_i \cdot \hat{\boldsymbol{z}}$ is given by

$$\begin{aligned} I_i &= \frac{1}{2}[\{\boldsymbol{E}_i^{(p)} + \boldsymbol{E}_i^{(s)}\} \times \{\boldsymbol{H}_i^{(p)*} + \boldsymbol{H}_i^{(s)*}\}] \cdot \hat{\boldsymbol{z}} \\ &= \frac{{E_0}^2}{2Z_i}[p_i \hat{\boldsymbol{p}}_i \times p_i^* \hat{\boldsymbol{s}}_i + s'_i \hat{\boldsymbol{s}}_i \times s_i'^* (-\hat{\boldsymbol{p}}_i)] \cdot \hat{\boldsymbol{z}} \\ &= \frac{{E_0}^2}{2Z_i}(|p_i|^2 + |s'_i|^2)\cos\psi. \end{aligned} \tag{2.87}$$

Here, $\cos\psi$ comes from the dot product $(\hat{\boldsymbol{p}}_i \times \hat{\boldsymbol{s}}_i) \cdot \hat{\boldsymbol{z}} = \hat{\boldsymbol{k}}_i \cdot \hat{\boldsymbol{z}}$, where $\hat{\boldsymbol{k}}_i$ is the unit vector in the direction of $\boldsymbol{k}_i$ (see Fig. 2.3). Similarly, intensity for the transmitted

wave, $I_t = \boldsymbol{S}_t \cdot \hat{\boldsymbol{z}}$ is derived as follows:

$$\begin{aligned} I_t &= \frac{1}{2}[\{\boldsymbol{E}_t^{(p)} + \boldsymbol{E}_t^{(s)}\} \times \{\boldsymbol{H}_t^{(p)*} + \boldsymbol{H}_t^{(s)*}\}] \cdot \hat{\boldsymbol{z}} \\ &= \frac{{E_0}^2}{2Z_t}[p_t \hat{\boldsymbol{p}}_t \times p_t^* \hat{\boldsymbol{s}}_t + s_t' \hat{\boldsymbol{s}}_i \times s_t'^* (-\hat{\boldsymbol{p}}_t)] \cdot \hat{\boldsymbol{z}} \\ &= \frac{{E_0}^2}{2Z_t}(|p_t|^2 + |s_t'|^2)\cos\chi. \end{aligned} \tag{2.88}$$

Intensity of the reflected wave is $I_r = \boldsymbol{S}_r \cdot (-\hat{\boldsymbol{z}})$, because the z-component of $\boldsymbol{k}_r$ has the opposite sign of those $\boldsymbol{k}_i$ and $\boldsymbol{k}_t$. I_r is given by

$$\begin{aligned} I_r &= \frac{1}{2}[\{\boldsymbol{E}_r^{(p)} + \boldsymbol{E}_r^{(s)}\} \times \{\boldsymbol{H}_r^{(p)*} + \boldsymbol{H}_r^{(s)*}\}] \cdot (-\hat{\boldsymbol{z}}) \\ &= \frac{{E_0}^2}{2Z_i}[p_r \hat{\boldsymbol{p}}_r \times p_r^* (-\hat{\boldsymbol{s}}_r) + s_r' \hat{\boldsymbol{s}}_r \times s_r'^* \hat{\boldsymbol{p}}_r] \cdot (-\hat{\boldsymbol{z}}) \\ &= \frac{{E_0}^2}{2Z_i}(|p_r|^2 + |s_r'|^2)\cos\psi. \end{aligned} \tag{2.89}$$

The transmission (reflection) probability T (R), are defined by the ratios of I_t (I_r) with I_i. T and R are given by

$$T = \frac{I_t}{I_i} = \frac{|p_t|^2(1+|\xi_t|^2)}{|p_i|^2(1+|\xi_i|^2)} \frac{Z_i \cos\chi}{Z_t \cos\psi} \tag{2.90}$$

and

$$R = \frac{I_r}{I_i} = \frac{|p_r|^2(1+|\xi_r|^2)}{|p_i|^2(1+|\xi_i|^2)}, \tag{2.91}$$

respectively. Because the 2D material possesses non-zero optical conductivities, it will absorb a fraction the electromagnetic wave. The absorption probability is given by

$$A = 1 - R - T. \tag{2.92}$$

2.3.2 Rotation and ellipticity angles of electric field

In this subsection, first we discuss how the phase difference between the p- and s-components of $\boldsymbol{E}_m$, Φ_m [see Eq. (2.73)], determines rotation and ellipticity angles of light. This discussion is required to derive formulas for the Faraday and the Kerr effects in 2D materials. We shall show that the ellipticity and the tilt angles of light are given as a function of ξ_m.

First, let us take the real part of $E_m^{(p)}$ and $E_m^{(s)}$ in Eq. (2.73), $\mathcal{E}_m^{(p)} \equiv \mathrm{Re}[E_m^{(p)}]$, and $\mathcal{E}_m^{(s)} \equiv \mathrm{Re}[E_m^{(s)}]$ as follows:

$$\mathcal{E}_m^{(p)} = E_0 p_m \cos(\boldsymbol{k}_m \cdot \boldsymbol{r} - \omega_m t), \tag{2.93}$$

and

$$\begin{aligned} \mathcal{E}_m^{(s)} &= E_0 s_m \cos(\boldsymbol{k}_m \cdot \boldsymbol{r} - \omega_m t + \Phi_m) \\ &= E_0 s_m \Big[\cos(\boldsymbol{k}_m \cdot \boldsymbol{r} - \omega_m t)\cos\Phi_m - \sin(\boldsymbol{k}_m \cdot \boldsymbol{r} - \omega_m t)\sin\Phi_m \Big]. \end{aligned} \tag{2.94}$$

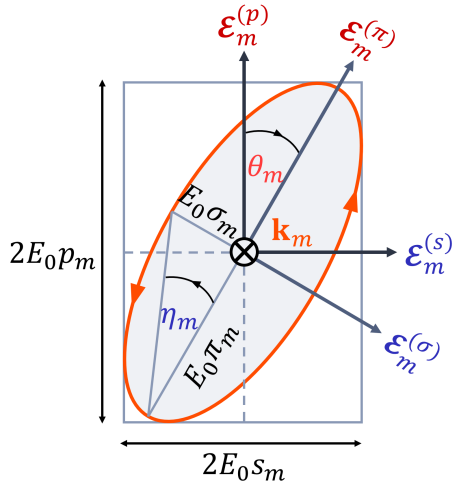

Figure 2.4 An elliptically polarized light in $(\mathcal{E}_m^{(p)}, \mathcal{E}_m^{(s)})$ and $(\mathcal{E}_m^{(\pi)}, \mathcal{E}_m^{(\sigma)})$ coordinates. $E_0\pi_m$ and $E_0\sigma_m$ are major and minor axes of the ellipse, respectively. Rotation and ellipticity angles are denoted by θ_m and η_m, respectively.

From Eqs. (2.93) and (2.94), we obtain two relations as follows:

$$\left[\frac{\mathcal{E}_m^{(s)}}{E_0 s_m} - \frac{\mathcal{E}_m^{(p)}}{E_0 p_m}\cos\Phi_m\right]^2 = \sin^2(\boldsymbol{k}_m\cdot\boldsymbol{r} - \omega_m t)\sin^2\Phi_m, \tag{2.95}$$

and

$$\left[1 - \left(\frac{\mathcal{E}_m^{(p)}}{E_0 p_m}\right)^2\right]\sin^2\Phi_m = \sin^2(\boldsymbol{k}_m\cdot\boldsymbol{r} - \omega_m t)\sin^2\Phi_m. \tag{2.96}$$

Since the right-hand sides of Eqs. (2.95) and (2.96) are identical, we get [2, 93]

$$\frac{1}{\sin^2\Phi_m {E_0}^2}\left[\frac{{\mathcal{E}_m^{(p)}}^2}{{p_m}^2} + \frac{{\mathcal{E}_m^{(s)}}^2}{{s_m}^2} - \frac{2\cos\Phi}{p_m s_m}\mathcal{E}_m^{(p)}\mathcal{E}_m^{(s)}\right] \equiv A{\mathcal{E}_m^{(p)}}^2 + B{\mathcal{E}_m^{(s)}}^2 + C\mathcal{E}_m^{(p)}\mathcal{E}_m^{(s)} = 1. \tag{2.97}$$

Eq. (2.97) is a general equation of an ellipse for $\mathcal{E}_m^{(p)}$ and $\mathcal{E}_m^{(s)}$. Thus, the phase difference Φ_m between $\mathcal{E}_m^{(p)}$ and $\mathcal{E}_m^{(p)}$ gives rise to an elliptically-polarized light. It is noted that linear and circular polarizations are special cases of elliptical polarization.

Now, let us consider elliptically-polarized light whose components are denoted by $\mathcal{E}_m^{(\pi)}$ and $\mathcal{E}_m^{(\sigma)}$, as shown in Fig. 2.4. Here, $\mathcal{E}_m^{(\pi)}$ is rotated clockwise by an angle θ_m with respect to $\mathcal{E}_m^{(p)}$. The relations between $(\mathcal{E}_m^{(p)}, \mathcal{E}_m^{(s)})$ and $(\mathcal{E}_m^{(\pi)}, \mathcal{E}_m^{(\sigma)})$ coordinates

Fig. 2.4: fig/ch2/elliptical.eps

are given by the rotation matrix by an angle θ_m and its inverse as follows:

$$\begin{bmatrix} \mathcal{E}_m^{(p)} \\ \mathcal{E}_m^{(s)} \end{bmatrix} = \begin{bmatrix} \cos\theta_m & -\sin\theta_m \\ \sin\theta_m & \cos\theta_m \end{bmatrix} \begin{bmatrix} \mathcal{E}_m^{(\pi)} \\ \mathcal{E}_m^{(\sigma)} \end{bmatrix}, \tag{2.98}$$

and

$$\begin{bmatrix} \mathcal{E}_m^{(\pi)} \\ \mathcal{E}_m^{(\sigma)} \end{bmatrix} = \begin{bmatrix} \cos\theta_m & \sin\theta_m \\ -\sin\theta_m & \cos\theta_m \end{bmatrix} \begin{bmatrix} \mathcal{E}_m^{(p)} \\ \mathcal{E}_m^{(s)} \end{bmatrix}. \tag{2.99}$$

Let us express $\mathcal{E}_m^{(\pi)}$ and $\mathcal{E}_m^{(\sigma)}$ by cosine waves as follows:

$$\mathcal{E}_m^{(\pi)} = E_0\pi_m \cos\left(\boldsymbol{k}_m \cdot \boldsymbol{r} - \omega_m t\right), \quad \mathcal{E}_m^{(\sigma)} = E_0\sigma_m \cos\left(\boldsymbol{k}_m \cdot \boldsymbol{r} - \omega_m t\right), \tag{2.100}$$

It is noted that $E_0\pi_m$ and $E_0\sigma_m$ are the major and minor axes of the ellipse as shown by Fig. 2.4, which satisfy

$$\left(\frac{\mathcal{E}_m^{(\pi)}}{E_0\pi_m}\right)^2 + \left(\frac{\mathcal{E}_m^{(\sigma)}}{E_0\sigma_m}\right)^2 = 1. \tag{2.101}$$

By using Eq. (2.99), we can express $\mathcal{E}_m^{(\pi)}$ and $\mathcal{E}_m^{(\sigma)}$ by $\mathcal{E}_m^{(p)}$ and $\mathcal{E}_m^{(s)}$, respectively. Thus Eq. (2.101) becomes

$$\begin{aligned} &\frac{1}{{E_0}^2}\left[\left(\frac{\cos^2\theta_m}{{\pi_m}^2} + \frac{\sin^2\theta_m}{{\sigma_m}^2}\right){\mathcal{E}_m^{(p)}}^2 + \left(\frac{\sin^2\theta_m}{{\pi_m}^2} + \frac{\cos^2\theta_m}{{\sigma_m}^2}\right){\mathcal{E}_m^{(s)}}^2\right. \\ &\left. + 2\sin\theta_m\cos\theta_m\left(\frac{1}{{\pi_m}^2} - \frac{1}{{\sigma_m}^2}\right)\mathcal{E}_m^{(p)}\mathcal{E}_m^{(s)}\right] \\ \equiv &A'{\mathcal{E}_m^{(p)}}^2 + B'{\mathcal{E}_m^{(s)}}^2 + C'\mathcal{E}_m^{(p)}\mathcal{E}_m^{(s)} \\ = &1 \end{aligned} \tag{2.102}$$

By comparing Eq. (2.97) with Eq. (2.102), we find that $A = A'$, $B = B'$ and $C = C'$. This fact is important to determine the ellipticity angle η_m and the tilt angle θ_m.

Now, let us perform some algebraic manipulations to determine the relations between p_m and s_m and π_m and σ_m. From Eqs. (2.97) and (2.102), we get

$$A + B = \frac{1}{\sin^2\Phi_m {E_0}^2}\left[\frac{1}{{p_m}^2} + \frac{1}{{s_m}^2}\right] = \frac{1}{\sin^2\Phi_m {E_0}^2}\left[\frac{{p_m}^2 + {s_m}^2}{{p_m}^2{s_m}^2}\right], \tag{2.103}$$

and

$$A' + B' = \frac{1}{{E_0}^2}\left[\frac{1}{{\pi_m}^2} + \frac{1}{{\sigma_m}^2}\right] = \frac{1}{{E_0}^2}\left[\frac{{\pi_m}^2 + {\sigma_m}^2}{{\pi_m}^2{\sigma_m}^2}\right], \tag{2.104}$$

respectively. Because $A + B = A' + B'$, we get

$${p_m}^2 + {s_m}^2 = {\pi_m}^2 + {\sigma_m}^2, \qquad p_m s_m \sin\Phi_m = \pi_m\sigma_m. \tag{2.105}$$

It is noted that because we define that π_m and σ_m are positive, the sign of s_m is the same as the sign of Φ_m from Eq. (2.105). Now, by referring to Fig. (2.4), we get

$$2\frac{\pi_m\sigma_m}{{\pi_m}^2+{\sigma_m}^2} = 2\cos\eta_m \sin\eta_m = \sin(2\eta_m). \tag{2.106}$$

On the other hand, the left-hand side of Eq. (2.106) can be obtained by

$$\frac{2}{{E_0}^2\pi_m\sigma_m}\frac{1}{A'+B'} = \frac{2p_m s_m}{{p_m}^2+{s_m}^2}\sin\Phi_m. \tag{2.107}$$

Thus, we show that the ellipticity angle η_m is given by the imaginary part of ξ_m as follows:

$$\sin(2\eta_m) = \frac{2\mathrm{Im}[\xi_m]}{1+|\xi_m|^2}. \tag{2.108}$$

Now, let us find the formula for the rotation angle θ_m. From Eq. (2.102), we get

$$A'-B' = \frac{1}{{E_0}^2}(\cos^2\theta_m - \sin^2\theta_m)\left[\frac{1}{{\pi_m}^2}-\frac{1}{{\sigma_m}^2}\right] = \frac{\cos(2\theta_m)}{{E_0}^2}\left[\frac{1}{{\pi_m}^2}-\frac{1}{{\sigma_m}^2}\right], \tag{2.109}$$

and

$$\frac{C'}{A'-B'} = \tan(2\theta_m). \tag{2.110}$$

Similarly, by using Eq. (2.97), we obtain

$$A-B = \frac{1}{\sin^2\Phi_m {E_0}^2}\left[\frac{1}{{p_m}^2}-\frac{1}{{s_m}^2}\right] = \frac{-1}{\sin^2\Phi_m {E_0}^2}\left[\frac{{p_m}^2-{s_m}^2}{{p_m}^2{s_m}^2}\right] \tag{2.111}$$

and

$$\frac{C}{A-B} = \frac{2p_m s_m}{{p_m}^2-{s_m}^2}\cos\Phi_m. \tag{2.112}$$

Because $C/(A-B) = C'/(A'-B')$, we can show that the rotation angle θ_m is proportional to the real part of ξ_m as follows:

$$\tan(2\theta_m) = \frac{2\mathrm{Re}[\xi_m]}{1-|\xi_m|^2}. \tag{2.113}$$

In particular, by using Eq. (2.113), we define the Faraday rotation $\theta_F = \theta_t$ for the transmitted light and the Kerr rotation $\theta_K = \theta_r$ for the reflected light.

Chapter 3

Methods to calculate magnetization in 2D materials

In this chapter, we present methods of calculations to obtain magnetization of 2D materials in Chapter 5. As a starting point, we discuss the equation of motion of an electron in the presence of an external magnetic field, and show that the canonical momentum can be expressed by the creation and annihilation operators. Then, we describe the Landau levels formations in 2D Dirac materials, such as gapless graphene, gapped graphene, and monolayer transition-metal dichacogenides (TMDs). Finally, we discuss how to obtain magnetization and orbital susceptibility as a function of magnetic field, temperature, chemical potential, as well as impurity scattering.

3.1 Landau levels of 2D Dirac materials

In the presence of external magnetic field $\boldsymbol{B}$, an electron in solid feels the Lorentz force $\boldsymbol{F}$, which keeps the electron moving in a closed orbit with a constant velocity $\boldsymbol{v}$, as follows:

$$\boldsymbol{F} = -e(\boldsymbol{v} \times \boldsymbol{B}). \tag{3.1}$$

The magnetic field is given by the vector potential $\boldsymbol{A}$ by $\boldsymbol{B} = \nabla \times \boldsymbol{A}$. By using the identity cross products $\boldsymbol{a} \times (\boldsymbol{b} \times \boldsymbol{c}) = \boldsymbol{b}(\boldsymbol{a} \cdot \boldsymbol{c}) - \boldsymbol{c}(\boldsymbol{b} \cdot \boldsymbol{a})$, we get

$$\boldsymbol{F} = -e\nabla(\boldsymbol{v} \cdot \boldsymbol{A}), \tag{3.2}$$

where we use the fact that $\nabla \cdot \boldsymbol{v} = 0$. In general, a conservative force is given by potential energy V by $\boldsymbol{F} = -\nabla V$. In the case of Eq. (3.2), the potential energy of electron associated with $\boldsymbol{B}$ is given by $V = e\boldsymbol{v} \cdot \boldsymbol{A}$. The Lagrangian [91] of an electron in $\boldsymbol{B}$ is thus given by

$$\mathcal{L} = \sum_{i=x,y} \Big[\frac{1}{2} m\dot{x}_i^2 - e\dot{x}_i A_i\Big], \tag{3.3}$$

where x_i is the i-th component of position vector $\boldsymbol{x}$. The kinetic momentum of electron $\boldsymbol{P} \equiv m\dot{\boldsymbol{x}}$ can be expressed in term of the canonical momentum p_i, which is related by the Lagrangian, $p_i = (\partial\mathcal{L}/\partial\dot{x}_i)$, as follows:

$$\boldsymbol{P} = \boldsymbol{p} + e\boldsymbol{A}. \tag{3.4}$$

Hence, the momentum of electron acquires an additional term in the magnetic field which is proportional to $\boldsymbol{A}$. This result is known as the Peierl substitution.

Let us first consider Hamiltonian of a 2D electron gas in magnetic field, in order to derive the Landau levels in the 2D Dirac materials. The electron gas is confined in a 2D box whose area is given by $\mathcal{A} = |L_x L_y|$, and the magnetic field is applied in the z-direction $\boldsymbol{B} = B\hat{\boldsymbol{z}}$. By using Eq. (3.4) and by adopting the Landau gauge $\boldsymbol{A} = (0, Bx)$, the Hamiltonian is given by

$$\hat{H} = \frac{1}{2m}[{p_x}^2 + (p_y + eBx)^2]. \tag{3.5}$$

By using $p_y = \hbar k_y$, Eq. (3.5) can be expressed as the Hamiltonian for a one-dimensional harmonic oscillator as follows:

$$\hat{H} = \frac{1}{2m}{p_x}^2 + \frac{1}{2}m{\omega_c}^2(x - x_0)^2, \tag{3.6}$$

where $\omega_c \equiv eB/m$ is the cyclotron frequency of the 2D electron gas, $x_0 \equiv -\hbar k_y/(eB)$ is the center of oscillation. The energy of electron in magnetic field is given by the eigenvalue of Eq. (3.6), which does not change by the shifting of x by x_0 as follows:

$$\epsilon_n = \hbar\omega_c\Big(n + \frac{1}{2}\Big), \quad n = 0,\ 1,\ 2, ... \tag{3.7}$$

Eq. (3.7) is the Landau level (LL) of a 2D electron gas. Since k_y is a good quantum number, its values are quantized, i.e. $k_y = 2\pi N/L_y$, where N is an integer to be determined as follows. It is noted that the maximum value of x in Eq. (3.6) is $|L_x|$, thus N satisfies

$$N = \frac{eBL_xL_y}{h} = B\frac{\mathcal{A}}{\phi_0}, \tag{3.8}$$

where $\phi_0 \equiv h/e$ is the quantum flux. Physically, N corresponds to the number of states of electron in the 2D material, which is known as the Landau degeneracy. Therefore, for each quantum flux, the LL is occupied by one electron.

Now, let us discuss the Landau quantization for the 2D Dirac materials. Here, we neglect the Zeeman term because we only consider the case in which the Zeeman splitting is much smaller than the LLs separation. We employ employ a 2×2 Hamiltonian matrix that is suitable to describe low-energy spectra of graphene and transition-metal dichalcogenides (TMDs). The latter is enabled by including a non-zero spin-orbit coupling (SOC) constant λ in the Hamiltonian [94], whose typical values are in the order of 100 meV. The Hamiltonian is given as follows [26, 27, 95]:

$$\hat{H}_{\tau s} = \begin{bmatrix} \Delta/2 & v_F\{\tau p_x - i(p_y + eBx)\} \\ v_F\{\tau p_x + i(p_y + eBx)\} & -\Delta/2 + \lambda\tau s \end{bmatrix}, \tag{3.9}$$

where $\Delta \geqslant 0$ and $v_F \sim 10^6$ m/s are band-gap and the Fermi velocity of the 2D Dirac material, respectively. In this case, $\boldsymbol{p} = (p_x, p_y)$ is measured from the K ($\tau = +1$) and the K' ($\tau = -1$) valleys, and $s = +1$ (-1) is the index for spin-up (spin-down) electron. To solve Eq. (3.9), we define an annihilation operator as follows:

$$\hat{a} \equiv \frac{1}{\sqrt{2m\hbar\omega_c}}[p_x + m\omega_c(x - x_0)] = \frac{\ell_B}{\sqrt{2}\hbar}[ip_x + (p_y + eBx)]. \tag{3.10}$$

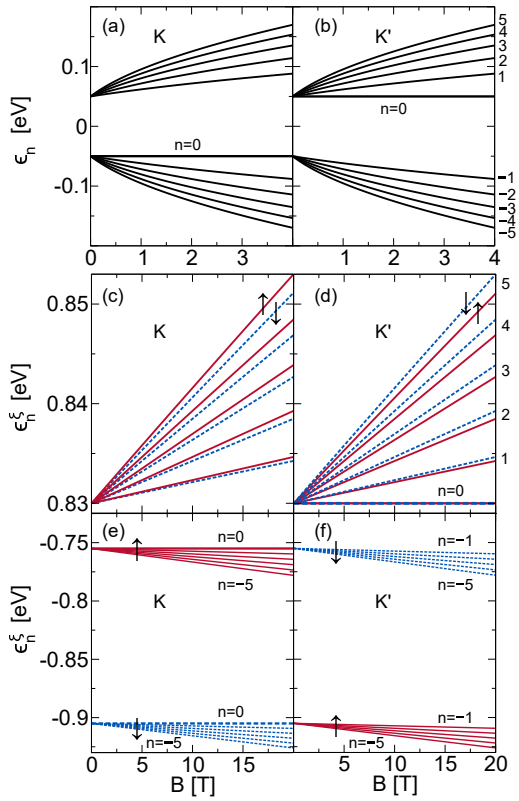

Figure 3.1 The LLs ($n = -5$ to $n = 5$) of the massive Dirac systems. The figures in the left (right) side correspond to the LLs at the K (K') valley. (a), (b): LLs of a gapped graphene ($\Delta = 100$ meV, $\lambda = 0$, and $v_F = 10^6$ m/s) for $B = 0 - 4$ T. (c)-(f) The LLs of MoS_2 ($\Delta = 1.66$ eV, $\lambda = 75$ meV and $v_F = 5.3 \times 10^5$ m/s) for $B = 0 - 20$ T. The LLs for the spin-up and spin-down electrons are shown with red-solid and blue-dashed lines, respectively [101].

Here, in the right-most side of Eq. (3.10), we define the magnetic length $\ell_B \equiv \sqrt{\hbar/(eB)}$, so that no mass variable appears in the expression of $\hat{a}$. The expression of $\hat{a}$ is useful to derive the LLs for massless Dirac fermions in graphene. Similarly, the creation operator $\hat{a}^\dagger$ is given by taking the complex conjugate of Eq. (3.10). In term of $\hat{a}$ and $\hat{a}^\dagger$, Eq. (3.9) becomes,

$$\hat{H}_\xi = \begin{bmatrix} \Delta/2 & -i\hbar\omega_c \hat{O}_\tau \\ i\hbar\omega_c \hat{O}_\tau^\dagger & -\Delta/2 + \lambda\xi \end{bmatrix}, \tag{3.11}$$

where $\xi \equiv \tau s$, $\hat{O}_+ \equiv \hat{a}$, and $\hat{O}_- \equiv \hat{a}^\dagger$. Thus, $\xi = +1(-1)$ represents the spin-up (spin-down) electron at the K valley or spin-down (spin-up) electron at K' valley. It is noted that in the 2D Dirac material, $\omega_c = \sqrt{2}v_F/\ell_B = \sqrt{2{v_F}^2 eB/\hbar}$, in contrast to the linear B-dependence in the case of the 2D electron gas.

Fig. 3.1: fig/ch3/Landaulvl2.eps

The LL ϵ_n^ξ is given by the eigenvalue Eq. (3.11), as follows:

$$\epsilon_n^\xi = \frac{\xi\lambda}{2} + \mathrm{sgn}_\tau(n)\sqrt{(\hbar\omega_c)^2|n| + \left(\frac{\Delta_\xi}{2}\right)^2}, \tag{3.12}$$

where we define $\Delta_\xi \equiv \Delta - \xi\lambda$ as a shorthand notation. In the absence of the SOC ($\lambda = 0$), we drop the superscript ξ in Eqs. (3.12) and (3.13). $\mathrm{sgn}_\tau(n)$ is the sign function defined by $\mathrm{sgn}_\tau(n) = -1$ for $n < 0$ and $\mathrm{sgn}_\tau(n) = +1$ for $n > 0$. In the case of $\Delta = 0$ and $\lambda = 0$, the LL of graphene in Eq. (1.24) is recovered from Eq. (3.12)

To determine the sign for the zeroth LLs ($n = 0$) we need to consider the wave function of electron $|\Psi_n^\xi\rangle$, which is given by the eigenvector of Eq. (3.11), as follows:

$$|\Psi_n^\xi\rangle = \frac{1}{\sqrt{2|\epsilon_n^\xi - \frac{\xi\lambda}{2}|}} \begin{bmatrix} -i\sqrt{|\epsilon_n^\xi + \frac{\Delta}{2} - \lambda\xi|}|\alpha_n^\tau\rangle \\ \sqrt{|\epsilon_n^\xi - \frac{\Delta}{2}|}|\beta_n^\tau\rangle \end{bmatrix}. \tag{3.13}$$

Here, $|\alpha_n^\tau\rangle$ and $|\beta_n^\tau\rangle$ are opposite for the K and K' valleys, i.e. $|\alpha_n^+\rangle = |\beta_n^-\rangle \equiv ||n|-1\rangle$ and $|\alpha_n^-\rangle = |\beta_n^+\rangle \equiv ||n|\rangle$, where $||n|\rangle$ is a normalized eigenvector of the operators $\hat{a}^\dagger$ and $\hat{a}^\dagger$, such that $\hat{a}||n|\rangle = \sqrt{|n|}||n|-1\rangle$ and $\hat{a}^\dagger||n|\rangle = \sqrt{|n|+1}||n|+1\rangle$. From Eq. (3.13), a non-trivial wave function is satisfied by choosing $\mathrm{sgn}_+(0) = -1$ and $\mathrm{sgn}_-(0) = +1$. Thus, the zeroth LLs at the K and K' valleys exist at the valence and the conduction bands, respectively [33, 34]. The existence of only one zeroth LL in each valley has been confirmed by first-principle calculations for hexagonal boron-nitride and MoS_2 [96]. For $\Delta < 0$ and $\lambda = 0$, a non-trivial wave function for $n = 0$ is satisfied by $\mathrm{sgn}_+(0) = +1$ and $\mathrm{sgn}_-(0) = -1$, as in the case of topological silicene [97]. Nevertheless, in this study we only consider $\Delta \geqslant$ without losing generality because it will be shown that the magnetization of the Dirac system depends only on the absolute value of Δ, and not on the sign. It is noted that our convention of the K and K' valleys is same as used in references [33, 34, 98], which is opposite of those references [35, 99].

In Fig. 3.1, we plot the LLs ($n = -5$ to $n = 5$) of a gapped graphene [(a) and (b)] and monolayer MoS_2 [(c)-(f)] at the K and the K' valleys as a function of the magnetic field B. In (a) and (b), the LLs of the gapped graphene with $\Delta = 100$ meV, $\lambda = 0$, and $v_F = 10^6$ m/s show $\sqrt{B}$ dependences, because $\Delta/2$ is smaller than the cyclotron energy $\hbar\omega_c$ (72.5 meV for $B = 4$ T). In Fig. 3.1(c)-(f), the LLs of MoS_2 at conduction bands [(c) and (d)] and valence bands [(e) and (f)] are shown, where we adopt $\Delta = 1.66$ eV, $\lambda = 75$ meV and $v_F = 5.3 \times 10^5$ m/s [94, 98, 99, 100]. We can see that the SOC generates spin-splitting between the spin-up (red-solid lines) and the spin-down (blue-dashed lines) electrons except for the zeroth LLs at the K' valley [Fig. 3.1(d)]. For the valence band, a spin-splitting $2\lambda = 150$ meV occurs for the zeroth LLs at the K valley [Fig. 3.1(e)]. The LLs are linearly dependent on B for $B = 0 - 20$ T because $\Delta/2$ is around ten times larger than $\hbar\omega_c = 0.086$ eV for $B = 20$ T.

3.2 Thermodynamic potential and magnetization

In order to obtain magnetization, let us derive thermodynamic potential for fermions. In the grand-canonical ensemble, the thermodynamic potential Ω is given by

$$\Omega = -\frac{1}{\beta}\sum_j g_j \ln\Big[\sum_{N_j} e^{-\beta(N_j\epsilon_j - N_j\mu)}\Big], \tag{3.14}$$

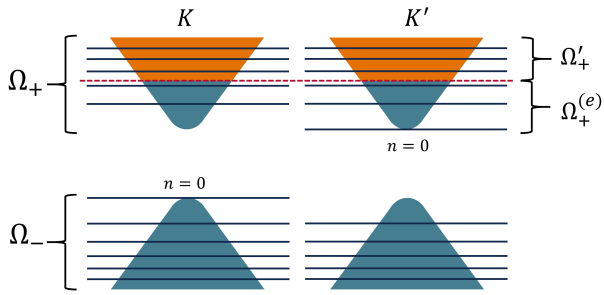

Figure 3.2 Schematic definitions of Ω_-, Ω_+, $\Omega_+^{(e)}$, and Ω'_+ for electron-doped gapped graphene. The black and red lines represent the LLs and the level of chemical potential μ, respectively [101].

where $\beta = 1/(k_B T)$ is the inverse temperature and μ is the chemical potential. N_j is the occupation number the j-th state, whose energy level and degeneracy are given by ϵ_j and g_j, respectively. In the case of fermions, the Pauli exclusion principle prevails, in which only one electron can occupy a given state j and thus $N_j = 0, 1$.

Let us apply Eq. (3.14) to the particular case of a 2D Dirac fermion in magnetic field as described in the Section 3.1. By assuming that the system is electron-doped, the thermodynamic potential per unit area consists all occupied Landau levels in both valence and conduction bands, as follows:

$$\begin{aligned}\Omega &= -\frac{1}{\beta}\frac{eB}{h}\sum_{\xi=\pm}\sum_{n=-\infty}^{\nu_\xi}\ln[1+e^{-\beta(\epsilon_n^\xi-\mu)}] \\ &\equiv [\Omega_- + \Omega_+^{(e)}],\end{aligned} \tag{3.15}$$

The pre-factor eB/h represents the Landau degeneracy per unit area for the each LL [see Eq. (3.8)]. The summation in Eq. (3.15) is carried out up to ν_ξ, which is defined as index of the highest occupied Landau at the conduction bands, that is obtained from Eq. (3.12) by setting $\mu = \epsilon_\nu^\xi$ as follows:

$$\nu_\xi \equiv \left\lfloor \frac{(\mu - \xi\lambda/2)^2 - (\Delta_\xi/2)^2}{(\hbar\omega_c)^2} \right\rfloor \equiv \lfloor \tilde{\nu_\xi} \rfloor, \tag{3.16}$$

where the floor function $\lfloor x \rfloor$ is gives by the greatest integer smaller than or equal to x. It is noted that for $\lambda = 0$, we drop the summation on ξ Eq. (3.15) and multiply the thermodynamic potentials by $g_s = 2$ to account the spin degeneracy. Similarly, we drop the subscript ξ in Eq. (3.16). For expository purposes, we define Ω_- and $\Omega_+^{(e)}$ as thermodynamic potentials for the occupied LLs at the valence and conduction bands, respectively, as illustrated in Fig. 3.2. We also define potential which include all the LLs at the conduction bands, Ω_+, as well as potential for $n = \nu_\xi + 1$ to $n = \infty$ LLs, Ω'_+. Thus, we have the relation $\Omega_+^{(e)} = \Omega_+ - \Omega'_+$. It shall be shown that Ω'_+ and Ω_+

Fig. 3.2: fig/ch3/Omega2.eps

are relevant for the calculations at high temperature. After obtaining an analytical expression of Ω, the magnetization is calculated by

$$M(B,\mu,T) = -\frac{\partial\Omega(B,\mu,T)}{\partial B}. \tag{3.17}$$

In the presence of impurity, the magnetization for a given scattering rate γ is calculated by convolution of M in Eq. (3.17) with a Lorentzian profile as follows [102, 103, 104, 105, 106]:

$$M(\mu,T,\gamma) = \frac{\gamma}{\pi}\int_{-\infty}^{\infty} d\varepsilon M(\varepsilon,T)\frac{1}{(\varepsilon-\mu)^2+\gamma^2}. \tag{3.18}$$

The parameter γ is related to the self-energy due impurity scattering, and γ is inversely proportional to the relaxation time of the quasiparticle. For simplicity, we assume that γ is independent of B and T, and therefore the susceptibility as a function of temperature is given by

$$\chi(\mu,T,\gamma) = \Big[\frac{\partial M(\mu,T,\gamma)}{\partial B}\Big]_{B=0}. \tag{3.19}$$

Chapter 4

Circular dichroism, Faraday and Kerr rotations in 2D materials

In this chapter, by using the energy dispersion of the Haldane model [Eq. (2.13)] and the Kubo formula for optical conductivity [Eq. (2.70)], we derive intrinsic longitudinal and Hall conductivities of the 2D Haldane material as a function of photon energy. Our formula is a generalization of the result by Haldane [16], which shows that the transport Hall conductivity of undoped topological Haldane material is quantized [see Fig. 1.6(c)]. The real part of the intrinsic Hall conductivity gives rise to the Faraday and the Kerr effects without applying an external magnetic field. In particular, the angles of the Faraday and the Kerr rotations show singularities when the photon energy matches to the band gap. Further, we show that the ellipticity of the transmitted and reflected lights are proportional to the circular dichroism (CD), which is given by imaginary part of the intrinsic Hall conductivity. Moreover, our formula for optical conductivities can be applied to various 2D materials, such as silicene and monolayer trasition-metal dichalcogenides (TMDs). The spin/valley dependence of the Hall conductivities give rise to spin-valley selection rule in silicene and valley polarization (VP) in monolayer TMDs.

4.1 Intrinsic optical conductivities of Haldane model

The Kubo formula for optical conductivity in Eq. (2.70) can be decomposed into the intraband $\sigma_{ij}^{(D,\kappa)}$ and interband contributions $\sigma_{ij}^{(E,\kappa)}$ of the K ($\kappa = +1$) and K' ($\kappa = -1$) valleys, as follows:

$$\sigma_{ij} = \sum_{\kappa=+1,-1} [\sigma_{ij}^{(D,\kappa)} + \sigma_{ij}^{(E,\kappa)}], \quad i,j = x,y. \tag{4.1}$$

The intraband conductivity originates from the excitation of electron within the same band. Since we discuss the optical transition, we can take limit $\boldsymbol{k} \to \mathbf{0}$ for the momen-

tum of photon in Eq. (2.70). The $\sigma_{ij}^{(D,\kappa)}$ is given by

$$\begin{aligned}\sigma_{ij}^{(D,\kappa)}(\omega) =& -ie^2\hbar \lim_{\boldsymbol{k}\to\boldsymbol{0}} \int \frac{d^2\boldsymbol{q}}{(2\pi)^2} \left[\frac{f\{\epsilon_v(\boldsymbol{q})\} - f\{\epsilon_v(\boldsymbol{q}+\boldsymbol{k})\}}{\epsilon_v(\boldsymbol{q}) - \epsilon_v(\boldsymbol{q}+\boldsymbol{k})} \frac{\langle v,\boldsymbol{q}|\hat{v}_i|v,\boldsymbol{q}+\boldsymbol{k}\rangle\langle v,\boldsymbol{q}+\boldsymbol{k}|\hat{v}_j|v,\boldsymbol{q}\rangle}{\epsilon_v(\boldsymbol{q}) - \epsilon_v(\boldsymbol{q}+\boldsymbol{k}) + \hbar\omega + i\hbar\gamma} \right. \\ &\left. + \frac{f\{\epsilon_c(\boldsymbol{q})\} - f\{\epsilon_c(\boldsymbol{q}+\boldsymbol{k})\}}{\epsilon_c(\boldsymbol{q}) - \epsilon_c(\boldsymbol{q}+\boldsymbol{k})} \frac{\langle c,\boldsymbol{q}|\hat{v}_i|c,\boldsymbol{q}+\boldsymbol{k}\rangle\langle c,\boldsymbol{q}+\boldsymbol{k}|\hat{v}_j|c,\boldsymbol{q}\rangle}{\epsilon_c(\boldsymbol{q}) - \epsilon_c(\boldsymbol{q}+\boldsymbol{k}) + \hbar\omega + i\hbar\gamma} \right] \\ =& -ie^2\hbar \int \frac{d^2\boldsymbol{q}}{(2\pi)^2} \left[\frac{df\{\epsilon_v(\boldsymbol{q})\}}{d\epsilon_v(\boldsymbol{q})} \frac{\langle v,\boldsymbol{q}|\hat{v}_i|v,\boldsymbol{q}\rangle\langle v,\boldsymbol{q}|\hat{v}_j|v,\boldsymbol{q}\rangle}{\hbar\omega + i\hbar\gamma} \right. \\ &\left. + \frac{df\{\epsilon_c(\boldsymbol{q})\}}{d\epsilon_c(\boldsymbol{q})} \frac{\langle c,\boldsymbol{q}|\hat{v}_i|c,\boldsymbol{q}\rangle\langle c,\boldsymbol{q}|\hat{v}_j|c,\boldsymbol{q}\rangle}{\hbar\omega + i\hbar\gamma} \right],\end{aligned} \tag{4.2}$$

where v (c) is the index for valence (conduction) band.

The interband conductivity $\sigma_{ij}^{(E,\kappa)}$ emerges when the transition of electron occurs between valence and conduction bands, as follows:

$$\begin{aligned}\sigma_{ij}^{(E,\kappa)}(\omega) =& -ie^2\hbar \int \frac{d^2\boldsymbol{q}}{(2\pi)^2} \left[\frac{f\{\epsilon_v(\boldsymbol{q})\} - f\{\epsilon_c(\boldsymbol{q})\}}{\epsilon_v(\boldsymbol{q}) - \epsilon_c(\boldsymbol{q})} \frac{\langle v,\boldsymbol{q}|\hat{v}_i|c,\boldsymbol{q}\rangle\langle c,\boldsymbol{q}|\hat{v}_j|v,\boldsymbol{q}\rangle}{\epsilon_v(\boldsymbol{q}) - \epsilon_c(\boldsymbol{q}) + \hbar\omega + i\hbar\gamma} \right. \\ &\left. + \frac{f\{\epsilon_c(\boldsymbol{q})\} - f\{\epsilon_v(\boldsymbol{q})\}}{\epsilon_c(\boldsymbol{q}) - \epsilon_v(\boldsymbol{q})} \frac{\langle c,\boldsymbol{q}|\hat{v}_i|v,\boldsymbol{q}\rangle\langle v,\boldsymbol{q}|\hat{v}_j|c,\boldsymbol{q}\rangle}{\epsilon_c(\boldsymbol{q}) - \epsilon_v(\boldsymbol{q}) + \hbar\omega + i\hbar\gamma} \right].\end{aligned} \tag{4.3}$$

Here, the velocity operator in the direction of i, $\hat{v}_i$ ($i = x, y$) is defined by

$$\hat{v}_i \equiv \frac{1}{\hbar}\frac{\partial\hat{\mathcal{H}}}{\partial q_i}, \tag{4.4}$$

where we adopt the Hamiltonian of the Haldane model [Eq. (2.12)] for $\hat{\mathcal{H}}$. The valley index κ is incorporated in the matrix elements of velocity in Eqs. (4.2) and (4.3) as we show as follows. By using the eigenvector of the Haldane model [Eq. (2.16)], the matrix elements of $\hat{v}_x$ from the intraband contributions are given by

$$\begin{aligned}\langle v,\boldsymbol{q}|\hat{v}_x|v,\boldsymbol{q}\rangle =& \frac{1}{2[\epsilon_v(\boldsymbol{q})+\zeta]} \begin{bmatrix}\sqrt{\epsilon_v+\zeta+\Gamma_\kappa} & \sqrt{\epsilon_v(\boldsymbol{q})+\zeta-\Gamma_\kappa}e^{-i\varphi/\kappa}\end{bmatrix} \\ &\times \begin{bmatrix}0 & \kappa v_F \\ \kappa v_F & 0\end{bmatrix} \begin{bmatrix}\sqrt{\epsilon_v(\boldsymbol{q})+\zeta+\Gamma_\kappa} \\ \sqrt{\epsilon_v(\boldsymbol{q})+\zeta-\Gamma_\kappa}e^{+i\varphi/\kappa}\end{bmatrix} \\ =& +\kappa v_F \frac{\sqrt{[\epsilon_v(\boldsymbol{q})+\zeta]^2 - {\Gamma_\kappa}^2}}{\epsilon_v+\zeta}\cos\left(\frac{\varphi}{\kappa}\right) \\ =& -\kappa v_F \frac{\sqrt{[\epsilon_c(\boldsymbol{q})+\zeta]^2 - {\Gamma_\kappa}^2}}{\epsilon_c+\zeta}\cos\left(\frac{\varphi}{\kappa}\right) \\ =& -\langle c,\boldsymbol{q}|\hat{v}_x|c,\boldsymbol{q}\rangle,\end{aligned} \tag{4.5}$$

where ζ and Γ_κ are defined by Eq. (2.13), and φ is the polar angle between q and q_x. In the third line of Eq. (4.5), we use Eq. (2.14) to express the matrix element of $\hat{v}_x$ in

term of $\epsilon_c(\boldsymbol{q})$ instead of $\epsilon_v(\boldsymbol{q})$. Similarly, the intraband matrix element of $\hat{v}_y$ is given as follows:

$$\begin{aligned}\langle v,\boldsymbol{q}|\hat{v}_y|v,\boldsymbol{q}\rangle &= \frac{1}{2[\epsilon_v(\boldsymbol{q})+\zeta]}\left[\sqrt{\epsilon_v(\boldsymbol{q})+\zeta+\Gamma_\kappa}\quad\sqrt{\epsilon_v(\boldsymbol{q})+\zeta-\Gamma_\kappa}e^{-i\varphi/\kappa}\right]\\ &\quad\times\begin{bmatrix}0 & -iv_F\\ iv_F & 0\end{bmatrix}\begin{bmatrix}\sqrt{\epsilon_v(\boldsymbol{q})+\zeta+\Gamma_\kappa}\\ \sqrt{\epsilon_v(\boldsymbol{q})+\zeta-\Gamma_\kappa}e^{+i\varphi/\kappa}\end{bmatrix}\\ &= -v_F\frac{\sqrt{[\epsilon_c(\boldsymbol{q})+\zeta]^2-{\Gamma_\kappa}^2}}{\epsilon_c(\boldsymbol{q})+\zeta}\sin\left(\frac{\varphi}{\kappa}\right)\\ &= -\langle c,\boldsymbol{q}|\hat{v}_y|c,\boldsymbol{q}\rangle.\end{aligned} \tag{4.6}$$

Thus, we can see that the intraband matrix elements of velocity possess opposite signs for the transitions within the valence and the conduction bands. The matrix element of $\hat{v}_x$ and $\hat{v}_y$ from the interband contributions are given by

$$\begin{aligned}\langle c,\boldsymbol{q}|\hat{v}_x|v,\boldsymbol{q}\rangle &= \frac{1}{-2[\epsilon_c(\boldsymbol{q})+\zeta]}\left[\sqrt{\epsilon_c(\boldsymbol{q})+\zeta+\Gamma_\kappa}\quad\sqrt{\epsilon_c(\boldsymbol{q})+\zeta-\Gamma_\kappa}e^{-i\varphi/\kappa}\right]\\ &\quad\times\begin{bmatrix}0 & \kappa v_F\\ \kappa v_F & 0\end{bmatrix}\begin{bmatrix}\sqrt{-[\epsilon_c(\boldsymbol{q})+\zeta]+\Gamma_\kappa}\\ \sqrt{-[\epsilon_c(\boldsymbol{q})+\zeta]-\Gamma_\kappa}e^{+i\varphi/\kappa}\end{bmatrix}\\ &= \frac{\kappa v_F}{2[\epsilon_c(\boldsymbol{q})+\zeta]}\left[\{\epsilon_c(\boldsymbol{q})+\zeta+\Gamma_\kappa\}e^{+i\varphi/\kappa}+\{\epsilon_c(\boldsymbol{q})+\zeta-\Gamma_\kappa\}e^{-i\varphi/\kappa}\right]\\ &= \kappa v_{\mathrm{F}}\left[\cos\left(\frac{\varphi}{\kappa}\right)+i\frac{\Gamma_\kappa}{\epsilon_{\mathrm{c}}+\zeta}\sin\left(\frac{\varphi}{\kappa}\right)\right]\\ &= \langle v,\boldsymbol{q}|\hat{v}_x|c,\boldsymbol{q}\rangle^*,\end{aligned} \tag{4.7}$$

and

$$\begin{aligned}\langle c,\boldsymbol{q}|\hat{v}_y|v,\boldsymbol{q}\rangle &= \frac{1}{-2[\epsilon_c(\boldsymbol{q})+\zeta]}\left[\sqrt{\epsilon_c(\boldsymbol{q})+\zeta+\Gamma_\kappa}\quad\sqrt{\epsilon_c(\boldsymbol{q})+\zeta-\Gamma_\kappa}e^{-i\varphi/\kappa}\right]\\ &\quad\times\begin{bmatrix}0 & -iv_F\\ iv_F & 0\end{bmatrix}\begin{bmatrix}\sqrt{-[\epsilon_c(\boldsymbol{q})+\zeta]+\Gamma_\kappa}\\ \sqrt{-[\epsilon_c(\boldsymbol{q})+\zeta]-\Gamma_\kappa}e^{+i\varphi/\kappa}\end{bmatrix}\\ &= v_{\mathrm{F}}\left[\sin\left(\frac{\varphi}{\kappa}\right)-i\frac{\Gamma_\kappa}{\epsilon_{\mathrm{c}}+\zeta}\cos\left(\frac{\varphi}{\kappa}\right)\right]\\ &= \langle v,\boldsymbol{q}|\hat{v}_y|c,\boldsymbol{q}\rangle^*,\end{aligned} \tag{4.8}$$

respectively. It is noted that the interband matrix elements of velocity are complex for $\Gamma_\kappa \neq 0$, as a result of broken time-reversal ($\mathcal{T}$) or/and inversion ($\mathcal{I}$) symmetries. The longitudinal conductivities [$\sigma_{xx}(\omega)$, $\sigma_{yy}(\omega)$] and the Hall conductivities [$\sigma_{xy}(\omega)$, $\sigma_{yx}(\omega)$] are analytically calculated by using Eq. (4.5)-(4.8).

Hereafter, we restrict our calculations either for undoped system ($\epsilon_F = 0$) or electron-doped system ($\epsilon_F > 0$) at low temperature ($T \approx 0$ K), where the Fermi energy ϵ_F is measured from the middle of band gap. For simplicity, it is assumed that the scattering due to impurity is negligible by setting the damping constant $\gamma \to 0$. Let

us first calculate the intraband contributions of the longitudinal conductivity $\sigma_{xx}^{(D,\kappa)}(\omega)$ from Eq. (4.3) as follows:

$$\sigma_{xx}^{(D,\kappa)}(\omega) = -ie^2\hbar \int \frac{d^2\boldsymbol{q}}{(2\pi)^2}\left[\frac{df\{\epsilon_v(\boldsymbol{q})\}}{d\epsilon_v(\boldsymbol{q})}\frac{|\langle v,\boldsymbol{q}|\hat{v}_x|v,\boldsymbol{q}\rangle|^2}{\hbar\omega+i\hbar\gamma} + \frac{df\{\epsilon_c(\boldsymbol{q})\}}{d\epsilon_c(\boldsymbol{q})}\frac{|\langle c,\boldsymbol{q}|\hat{v}_x|c,\boldsymbol{q}\rangle|^2}{\hbar\omega+i\hbar\gamma}\right]. \tag{4.9}$$

It is noted that $f(\epsilon_v) = 1$ because the valence band is fully occupied. On the other hand, we let $f(\epsilon_c) = \Theta(\epsilon_F - \epsilon_c)\Theta[\epsilon_F - \epsilon_{c0}^{(\kappa)}]$ to make sure that the intraband conductivity is relevant only if the conduction bands are occupied up to ϵ_F. $\Theta(x) = 1$ (0) for $x \geqslant 0$ ($x < 0$) is the Heaviside step function and

$$\epsilon_{c0}^{(\kappa)} \equiv -\zeta + |\Gamma_\kappa| \tag{4.10}$$

is the bottom of the conduction band at the κ valley, which is given by setting $\epsilon_c(q = 0)$. By transforming $\boldsymbol{q} = (q_x, q_y)$ into polar coordinate $\boldsymbol{q} = (q, \varphi)$, the integration on $\boldsymbol{q}$ is given by

$$\begin{aligned}\sigma_{xx}^{(D,\kappa)}(\omega) =& -\frac{ie^2\hbar}{4\pi^2}\int_0^\infty qdq\int_0^{2\pi} d\varphi\Bigg[-\delta(\epsilon_F-\epsilon_c)\Theta(\epsilon_F-\epsilon_{c0}^{(\kappa)})\kappa^2 {v_F}^2\frac{(\epsilon_c+\zeta)^2-{\Gamma_\kappa}^2}{(\epsilon_c+\zeta)^2} \\ &\times\cos^2\left(\frac{\varphi}{\kappa}\right)\Bigg]\frac{1}{\hbar\omega+i\hbar\gamma} \\ =& \frac{ie^2}{4\pi^2\hbar}\left[\int_{\epsilon_{c0}^{(\kappa)}}^\infty d\epsilon_c\delta(\epsilon_F-\epsilon_c)\Theta(\epsilon_F-\epsilon_{c0}^{(\kappa)})\frac{(\epsilon_c+\zeta)^2-{\Gamma_\kappa}^2}{(\epsilon_c+\zeta)}\int_0^{2\pi} d\varphi\cos^2\left(\frac{\varphi}{\kappa}\right)\right] \\ &\times\left[\frac{-i\hbar\gamma}{(\hbar\omega)^2+(\hbar\gamma)^2}+\frac{\hbar\omega}{(\hbar\omega)^2+(\hbar\gamma)^2}\right].\end{aligned} \tag{4.11}$$

In the first line of Eq. (4.11), we have used $qdq = (\epsilon_c + \zeta)d\epsilon_c/(\hbar v_F)^2$ [see Eq. (2.13)]. By using the identity $\lim_{a\to 0} a/(x^2 + a^2) = \pi\delta(x)$, we get

$$\begin{aligned}\sigma_{xx}^{(D,\kappa)}(\omega) =& \frac{e^2}{4\hbar}\frac{(\epsilon_F+\zeta)^2-{\Gamma_\kappa}^2}{(\epsilon_F+\zeta)}\delta(\hbar\omega)\Theta[\epsilon_F-\epsilon_{c0}^{(\kappa)}] + i\frac{e^2}{4\pi\hbar^2\omega}\frac{(\epsilon_F+\zeta)^2-{\Gamma_\kappa}^2}{(\epsilon_F+\zeta)}\Theta[\epsilon_F-\epsilon_{c0}^{(\kappa)}] \\ =& \sigma_{yy}^{(D,\kappa)}(\omega).\end{aligned} \tag{4.12}$$

The statement in second line of Eq. (4.12) is inferred by using the fact that $\int_0^{2\pi}\cos^2(\varphi/\kappa) = \int_0^{2\pi}\sin^2(\varphi/\kappa) = \pi$ for $\kappa = \pm 1$ [see Eq. (4.6)] for the intraband matrix element of $\hat{v}_y$.

The interband contribution of the longitudinal conductivity is derived by using $f(\epsilon_c) = \Theta(\Lambda_\kappa - \epsilon_c)$, where the function

$$\Lambda_\kappa \equiv \max[\epsilon_F, \epsilon_{c0}^{(\kappa)}] \tag{4.13}$$

takes the larger value from ϵ_F and $\epsilon_{c0}^{(\kappa)}$. Thus, the interband transitions can occur for both undoped and doped systems, provided that the Pauli exclusion principle is not

violated. Here, we use the identity $f(\epsilon_v) - f(\epsilon_c) = 1 - \Theta(\Lambda_\kappa - \epsilon_c) = \Theta(\epsilon_c - \Lambda_\kappa)$. By using Eqs. (4.3) and (4.7), $\sigma_{xx}^{(D,\kappa)}(\omega)$ is derived as follows:

$$\begin{aligned}
\sigma_{xx}^{(E,\kappa)}(\omega) =& -ie^2\hbar \int \frac{d^2\boldsymbol{q}}{(2\pi)^2} \left[\frac{f\{\epsilon_v(\boldsymbol{q})\} - f\{\epsilon_c(\boldsymbol{q})\}}{\epsilon_v(\boldsymbol{q}) - \epsilon_c(\boldsymbol{q})} |\langle c, \boldsymbol{q}|\hat{v}_x|v, \boldsymbol{q}\rangle|^2 \right. \\
& \left. \times \left\{ \frac{1}{\epsilon_v(\boldsymbol{q}) - \epsilon_c(\boldsymbol{q}) + \hbar\omega} + \frac{1}{\epsilon_c(\boldsymbol{q}) - \epsilon_v(\boldsymbol{q}) + \hbar\omega} \right\} \right] \\
=& -\frac{ie^2\hbar}{4\pi^2} \int_{\epsilon_{c0}^{(\kappa)}}^{\infty} \frac{(\epsilon_c + \zeta) d\epsilon_c}{(\hbar v_F)^2} \int_0^{2\pi} d\varphi \left[\frac{\Theta(\epsilon_c - \Lambda_\kappa)}{-2(\epsilon_c + \zeta)} \kappa^2 {v_F}^2 \right. \\
& \left. \times \left\{ \cos^2\left(\frac{\varphi}{\kappa}\right) + \frac{{\Gamma_\kappa}^2}{(\epsilon_c + \zeta)^2} \sin^2\left(\frac{\varphi}{\kappa}\right) \right\} \frac{2\hbar\omega}{(\hbar\omega)^2 - 4(\epsilon_c + \zeta)^2} \right] \\
=& -\frac{ie^2}{4\pi\hbar} \int_{\Lambda_\kappa}^{\infty} d\epsilon_c \left[1 + \frac{{\Gamma_\kappa}^2}{(\epsilon_c + \zeta)^2} \right] \left[\frac{\hbar\omega}{4(\epsilon_c + \zeta)^2 - (\hbar\omega)^2} \right].
\end{aligned} \tag{4.14}$$

In the second line of Eq. (4.14), we use $\epsilon_v - \epsilon_c = -2(\epsilon_c + \zeta)$ [see Eqs. (2.13) and (2.14)]. It is noted that because of the function $\Theta(\epsilon_c - \Lambda_\kappa)$, the lower limit of integration on ϵ_c is shifted from $\epsilon_{c0}^{(\kappa)}$ to Λ_κ. The integral of in the third line of Eq. (4.14) can be solved by using a formula

$$\begin{aligned}
\int_d^{\infty} dx \frac{a}{4(x+b)^2 - a^2} \left[1 + \frac{c^2}{(x+b)^2} \right] =& \frac{1}{2} \left[1 + \frac{4c^2}{a^2} \right] \ln \left[\sqrt{\frac{2(d+b)+a}{2(d+b)-a}} \right] \\
& - \frac{c^2}{a(d+b)},
\end{aligned} \tag{4.15}$$

for given real variables a, b, c, and d, by assuming that $d + b > 0$, and $2(d+b) \pm a > 0$. Thus, $\sigma_{xx}^{(E,\kappa)}(\omega)$ is given by

$$\sigma_{xx}^{(E,\kappa)}(\omega) = -\frac{ie^2}{4\pi\hbar} \left[\frac{1}{2} \left\{ 1 + \frac{4{\Gamma_\kappa}^2}{(\hbar\omega)^2} \right\} \ln \left[\sqrt{\frac{2(\Lambda_\kappa + \zeta) + \hbar\omega}{2(\Lambda_\kappa + \zeta) - \hbar\omega}} \right] - \frac{{\Gamma_\kappa}^2}{\hbar\omega(\Lambda_\kappa + \zeta)} \right]. \tag{4.16}$$

The interband transition occurs only when the photon energy is larger than the band gap, i.e. $\hbar\omega > 2|\Gamma_\kappa|$ [or, equivalently $\hbar\omega > 2(\epsilon_{c0}^{(\kappa)} + \zeta)$]. On the other hand, because of the Pauli exclusion principle, $\hbar\omega > 2(\epsilon_F + \zeta)$ should be satisfied. Therefore, the interband transition is allowed only if $\hbar\omega > 2(\Lambda_\kappa + \zeta)$. This means that the variables inside the square root in Eq. (4.16) is negative. By noting that $\ln(\sqrt{-x}) = \ln(i) + (1/2)\ln|x|$ for $x > 0$ and $\ln(i) = i\pi/2$, we get the real and imaginary parts of the $\sigma_{xx}^{(E,\kappa)}$ as follows:

$$\begin{aligned}
\sigma_{xx}^{(E,\kappa)}(\omega) =& \frac{e^2}{16\hbar} \left[1 + \frac{4{\Gamma_\kappa}^2}{(\hbar\omega)^2} \right] \Theta[\hbar\omega - 2(\Lambda_\kappa + \zeta)] + i\frac{e^2}{4\pi\hbar^2\omega} \frac{{\Gamma_\kappa}^2}{(\Lambda_\kappa + \zeta)} \\
& + i\frac{e^2}{16\pi\hbar} \left[1 + \frac{4{\Gamma_\kappa}^2}{(\hbar\omega)^2} \right] \ln \left| \frac{2(\Lambda_\kappa + \zeta) - \hbar\omega}{2(\Lambda_\kappa + \zeta) + \hbar\omega} \right| \\
=& \sigma_{yy}^{(E,\kappa)}(\omega).
\end{aligned} \tag{4.17}$$

Now, let us derive the Hall conductivities of the Haldane material. By using Eqs. (4.5) and (4.6), it is shown that intraband contribution of the Hall conductivity is zero,

$$\begin{aligned}\sigma_{xy}^{(D,\kappa)}(\omega) &= -ie^2\hbar\int\frac{d^2\boldsymbol{q}}{(2\pi)^2}\left[\frac{df\{\epsilon_c(\boldsymbol{q})\}}{d\epsilon_c(\boldsymbol{q})}\frac{\langle c,\boldsymbol{q}|\hat{v}_x|c,\boldsymbol{q}\rangle\langle c,\boldsymbol{q}|\hat{v}_y|c,\boldsymbol{q}\rangle}{\hbar\omega+i\hbar\gamma}\right]\\ &= -\frac{ie^2\hbar}{4\pi^2}\int_0^\infty qdq\int_0^{2\pi}d\varphi\Bigg[-\delta(\epsilon_F-\epsilon_c)\Theta(\epsilon_F-\epsilon_{c0}^{(\kappa)})\kappa {v_F}^2\frac{(\epsilon_c+\zeta)^2-{\Gamma_\kappa}^2}{(\epsilon_c+\zeta)^2}\\ &\quad\times\cos\left(\frac{\varphi}{\kappa}\right)\sin\left(\frac{\varphi}{\kappa}\right)\Bigg]\frac{1}{\hbar\omega+i\hbar\gamma}\\ &= \sigma_{yx}^{(D,\kappa)}(\omega)\\ &= 0,\end{aligned} \tag{4.18}$$

because $\cos(\varphi/\kappa)\sin(\varphi/\kappa)$ is an odd function of φ.

In the case of the interband contribution of the Hall conductivity, we shall show that the signs of $\sigma_{xy}^{(E,\kappa)}(\omega)$ depends on the valley index κ, or the phase angle of the Haldane material ϕ. The general formula for $\sigma_{xy}^{(E,\kappa)}(\omega)$ is given by

$$\begin{aligned}\sigma_{xy}^{(E,\kappa)}(\omega) = -ie^2\hbar\int\frac{d^2\boldsymbol{q}}{(2\pi)^2}\Bigg[&\frac{f\{\epsilon_v(\boldsymbol{q})\}-f\{\epsilon_c(\boldsymbol{q})\}}{\epsilon_v(\boldsymbol{q})-\epsilon_c(\boldsymbol{q})}\\ &\times\left\{\frac{\langle v,\boldsymbol{q}|\hat{v}_x|c,\boldsymbol{q}\rangle\langle c,\boldsymbol{q}|\hat{v}_y|v,\boldsymbol{q}\rangle}{\epsilon_v(\boldsymbol{q})-\epsilon_c(\boldsymbol{q})+\hbar\omega}+\frac{\langle c,\boldsymbol{q}|\hat{v}_x|v,\boldsymbol{q}\rangle\langle v,\boldsymbol{q}|\hat{v}_y|c,\boldsymbol{q}\rangle}{\epsilon_c(\boldsymbol{q})-\epsilon_v(\boldsymbol{q})+\hbar\omega}\right\}\Bigg].\end{aligned} \tag{4.19}$$

It is helpful to note that the products of the matrix elements of velocities in Eq. (4.19) are given by

$$\begin{aligned}\langle v,\boldsymbol{q}|\hat{v}_x|c,\boldsymbol{q}\rangle\langle c,\boldsymbol{q}|\hat{v}_y|v,\boldsymbol{q}\rangle &= \kappa {v_F}^2\left[\left\{1-\frac{{\Gamma_\kappa}^2}{(\epsilon_c+\zeta)^2}\right\}\cos\left(\frac{\varphi}{\kappa}\right)\sin\left(\frac{\varphi}{\kappa}\right)-i\frac{\Gamma_\kappa}{(\epsilon_c+\zeta)}\right]\\ &= (\langle c,\boldsymbol{q}|\hat{v}_x|v,\boldsymbol{q}\rangle\langle v,\boldsymbol{q}|\hat{v}_y|c,\boldsymbol{q}\rangle)^*.\end{aligned} \tag{4.20}$$

We can see that by integration on φ from 0 to 2π, the real part vanishes of Eq. (4.20), and the remaining imaginary part is given by $-2\pi i\Gamma_\kappa/(\epsilon+\zeta)$. Thus, the Hall conductivity is determined by the imaginary part of the products of the matrix elements of $\hat{v}_x$ and $\hat{v}_y$, whereas for the longitudinal conductivities, the products of the matrix elements of velocities are always real. Eq. (4.19) is reduced as follows:

$$\sigma_{xy}^{(E,\kappa)}(\omega) = -\kappa\Gamma_\kappa\frac{e^2}{\pi\hbar}\int_{\Lambda_{(\kappa)}}^\infty d\epsilon_c\frac{1}{4(\epsilon_c+\zeta)^2-(\hbar\omega)^2}. \tag{4.21}$$

By applying the following formula

$$\int_d^\infty dx\frac{1}{4(x+b)^2-a^2} = \frac{1}{2a}\ln\left[\sqrt{\frac{2(d+b)+a}{2(d+b)-a}}\right] \tag{4.22}$$

on Eq. (4.21), and by imposing the requisite for the interband transition [$\hbar\omega > 2(\Lambda_\kappa + \zeta)$], we get

$$\begin{aligned}\sigma_{xy}^{(E,\kappa)}(\omega) = & \frac{e^2}{4\pi\hbar^2\omega}\kappa\Gamma_\kappa \ln\left|\frac{2(\Lambda_\kappa+\zeta)-\hbar\omega}{2(\Lambda_\kappa+\zeta)+\hbar\omega}\right| - i\frac{e^2}{4\pi\hbar^2\omega}\kappa\Gamma_\kappa\Theta[\hbar\omega-2(\Lambda_\kappa+\zeta)] \\ = & -\sigma_{yx}^{(E,\kappa)}(\omega),\end{aligned} \tag{4.23}$$

where we infer $\sigma_{xy}^{(E,\kappa)}(\omega) = -\sigma_{yx}^{(E,\kappa)}(\omega)$ from the second line of Eq. (4.20). It is noted that the real and imaginary parts of the Hall conductivity consist of the logarithmic function $\ln|2(\Lambda_\kappa+\zeta) \mp \hbar\omega|$ and the Heaviside function $\Theta[\hbar\omega - 2(\Lambda_\kappa+\zeta)]$, respectively, as is opposite to that of the interband longitudinal conductivity [see Eq. (4.17)]. We can see that the interband Hall conductivity gives a non-zero value because the imaginary part of the product $\langle b, \boldsymbol{q}|\hat{v}_x|b', \boldsymbol{q}\rangle\langle b', \boldsymbol{q}|\hat{v}_y|b, \boldsymbol{q}\rangle$ does not vanish after the integration on φ. It can be shown that in the case when the $\mathcal{T}$ and $\mathcal{I}$ symmetries are conserved ($t_2 = 0$, $\phi = 0$, and $M = 0$), the optical conductivities of the monolayer graphene [107, 108] are recovered from Eqs. (4.12), (4.17), and (4.23).

The pre-factor $\kappa\Gamma_\kappa = \kappa M - 3\sqrt{3}t_2 \sin\phi$ in the expression of $\sigma_{xy}^{(E,\kappa)}(\omega)$ represents the dependence of the intrinsic Hall conductivity on the topological phases of the Haldane model. From Eq. (4.23), we can see that the sign of the real and imaginary parts of $\sigma_{xy}^{(E,\kappa)}$, $\mathrm{Re}[\sigma_{xy}^{(E,\kappa)}]$ and $\mathrm{Im}[\sigma_{xy}^{(E,\kappa)}]$, depend on the region of the phase diagram of the Haldane model as given by Fig. 1.6(c). In the region i (ii), where the effect of the broken $\mathcal{T}$ symmetry is dominant over the broken $\mathcal{I}$ symmetry ($|M| < 3\sqrt{3}|t_2 \sin\phi|$), $\mathrm{Re}[\sigma_{xy}^{(E,\kappa)}]$ and $\mathrm{Im}[\sigma_{xy}^{(E,\kappa)}]$ are positive (negative) for both the K and K' valleys. On the other hand, when the effect of the broken $\mathcal{I}$ symmetry is larger than the broken $\mathcal{T}$ symmetry ($|M| > 3\sqrt{3}|t_2 \sin\phi|$), $\mathrm{Re}[\sigma_{xy}^{(E,\kappa)}]$ and $\mathrm{Im}[\sigma_{xy}^{(E,\kappa)}]$ are negative for K the valley and positive for the K' valley for the region iii, and vice versa for the region iv.

Let us we show that in the limit of $\omega \to 0$, the Hall conductivity of the topological Haldane material is indeed quantized for $\epsilon_F = 0$, where the $\Lambda_\kappa = \epsilon_{c0}^{(\kappa)}$. It is noted that $\mathrm{Im}[\sigma_{xy}^{(E,\kappa)}] = 0$ because of the function $\Theta[\hbar\omega - 2(\Lambda_\kappa+\zeta)]$. By applying the expansion $\ln(a+x) \approx \ln(a) + x/a$ for $x \ll a$ on Eq. (4.23), $\sigma_{xy}^{(E,\kappa)}$ reduces to

$$\sigma_{xy}^{(E,\kappa)} = -\frac{e^2}{4\pi\hbar^2\omega}\kappa\Gamma_\kappa\frac{\hbar\omega}{|\Gamma_\kappa|}. \tag{4.24}$$

In the case of $|M| < 3\sqrt{3}|t_2 \sin\phi|$, the sign of Γ_κ does not depend on the valley index κ and only depends on ϕ, we can write $\kappa\Gamma_\kappa = -\mathrm{sgn}(\phi)|\Gamma_\kappa|$. By including the contributions from both the K and K' valleys [see Eq. (4.1)] the Hall conductivity is given by

$$\sigma_{xy} = \mathrm{sgn}(\phi)\frac{e^2}{\hbar}, \tag{4.25}$$

which shows the quantum anomalous Hall effect in the topological phase of the Haldane model. It is noted that when $|M| > 3\sqrt{3}|t_2 \sin\phi|$, $\sigma_{xy} = 0$ because the sign of $\sigma_{xy}^{(E,+1)}$ (K valley) is opposite to $\sigma_{xy}^{(E,-1)}$ (K' valley).

Let us illustrate the dependence of the optical conductivities on t_2, ϕ, and M for the for topological and trivial Haldane materials, respectively. For the topological

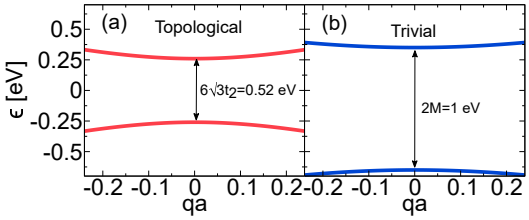

Figure 4.1 (a) Energy bands around the K point for (a) the topological ($t_2 = 0.05$ eV, $\phi = \pi/2$, and $M = 0$) and (b) the trivial ($t_2 = 0.05$ eV, $\phi = 0$, and $M = 0.5$ eV) Haldane materials [66].

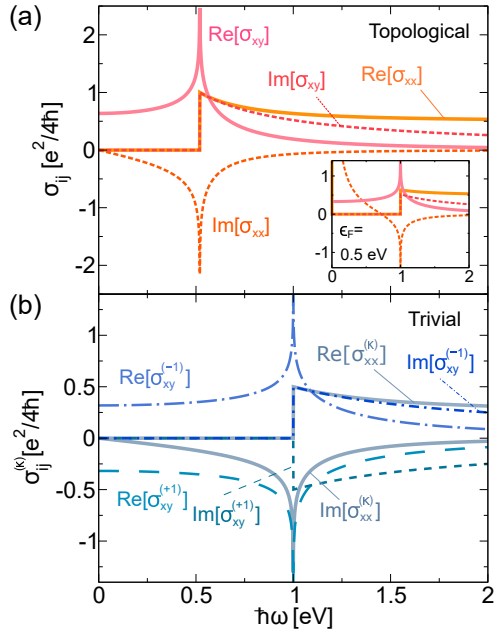

Figure 4.2 (a) Optical conductivities for (a) the topological ($t_2 = 0.05$ eV, $\phi = \pi/2$, and $M = 0$) and (b) the trivial ($t_2 = 0.05$ eV, $\phi = 0$, and $M = 0.5$ eV) Haldane materials [66]. Inset in (a) shows the optical conductivities for the doped case, $\epsilon_F = 0.5$ eV.

(trivial) Haldane material, we adopt $t_2 = 0.05$ eV, $\phi = \pi/2$, and $M = 0$ ($t_2 = 0.05$ eV, $\phi = 0$, and $M = 0.5$ eV). It is noted that the example of the topological (trivial) cases given here corresponds to the region i (iii) in Fig. 1.6(c). In Fig. 4.1(a) and (b), we plot the energy dispersions of the topological and the trivial Haldane materials, respectively. In Fig. 4.1(a), the energy gap is $\epsilon_g^{(\kappa)} = 6\sqrt{3}t_2 = 0.52$ eV, while in Fig. 4.1(b), $\epsilon_g^{(\kappa)} = 2M = 1$ eV.

In Fig. 4.2(a), we plot $\sigma_{xx}(\omega)$ and $\sigma_{xy}(\omega)$ of the topological Haldane material

Fig. 4.1: fig/ch4/haldane-eps.eps
Fig. 4.2: fig/ch4/haldane-sig2.eps

without doping ($\epsilon_F = 0$), where only interband transition takes place. In the inset of Fig. 4.2(a), we plot the case for doped topological Haldane material ($\epsilon_F = 0.5$ eV) to illustrate the effects of intraband transition on the optical conductivities. Here, σ_{xx} and σ_{xy} consist of the contributions of the electrons at the K and K' valleys. We observe that for $\epsilon_F = 0$, $\mathrm{Re}[\sigma_{xx}]$ and $\mathrm{Im}[\sigma_{xy}]$ decrease monotonically when $\hbar\omega > \epsilon_g^{(\kappa)} = 0.52$ eV, while $\mathrm{Im}[\sigma_{xx}]$ and $\mathrm{Re}[\sigma_{xy}]$ show logarithmic singularities at $\hbar\omega = \epsilon_g^{(\kappa)}$. In the case of $\epsilon_F = 0.5$ eV, we can see that the $\mathrm{Re}[\sigma_{xx}]$ and $\mathrm{Im}[\sigma_{xx}]$ diverge at $\hbar\omega = 0$ due to the dependences on $\delta(\hbar\omega)$ and $1/\omega$, respectively. The effect of the electron doping also shift the singular points of σ_{xx} and σ_{xy} from $\hbar\omega = \epsilon_g^{(\kappa)}$ to $\hbar\omega = 2\epsilon_F = 1$ eV.

In Fig. 4.2(b), we plot the optical conductivities per valley $\sigma_{ij}^{(\kappa)}(\omega) \equiv \sigma_{ij}^{(D,\kappa)}(\omega) + \sigma_{ij}^{(E,\kappa)}(\omega)$ for the trivial Haldane material ($\epsilon_F = 0$). As in the case of the topological Haldane material, the singularities in the Hall conductivities occur when the light energy match to the energy gap $\hbar\omega = \epsilon_g^{(\kappa)} = 1$ eV. It is noted that $\sigma_{xx}^{(\kappa)}$ does not have valley dependence, while $\sigma_{xy}^{(+1)}$ has equal magnitude but opposite sign to that of $\sigma_{xy}^{(-1)}$. We shall show in the next section that this property generates VP in the Haldane material. On the other hand, when $\sigma_{xy}(\omega)$ does not vanish as in the case of In Fig. 4.2(a), the Haldane material shows circular dichroism (CD). The phenomena of CD and VP will be discussed in the next section, in which we derive the absorption probabilities.

4.2 Optical absorption probability in Haldane material

In order to derive the expression of optical probability in the 2D Haldane material, we need to solve the variable $\xi_m \equiv s'_m/p_m$ from the boundary conditions of the Maxwell equations, which are given by Eqs. (2.81)-(2.84). We remind the readers that s'_m and p_m are the components of the Jones vector of the electric field in medium m, $m = i, t, r$ [see Eq. (2.74)]. First, we derive ξ_t as a function of ξ_i. In other words, we determine the property of transmitted light for a given incident light. By some algebraic manipulations, we eliminate p_r in Eqs. (2.81) and (2.82), and derive a relation as follows:

$$2p_i Z_t \cos\psi = p_t[Z_t \cos\chi + Z_i \cos\psi + Z_i Z_t \sigma_{xx}(\omega)\cos\psi\cos\chi] + s'_t Z_i Z_t \sigma_{xy}(\omega)\cos\psi. \tag{4.26}$$

Similarly, by eliminating s'_r in Eqs. (2.83) and (2.84), we get

$$2s'_i Z_t \cos\psi = s'_t[Z_t \cos\psi + Z_i \cos\chi + Z_i Z_t \sigma_{xx}(\omega)] - p_t Z_i Z_t \sigma_{xy}(\omega)\cos\chi. \tag{4.27}$$

By dividing Eq. (4.27) by Eq. (4.26), we obtain

$$\xi_i = \frac{s'_t \Delta_s - p_t Z_i Z_t \sigma_{xy}(\omega)\cos\chi}{p_t \Delta_p + s'_t Z_i Z_t \sigma_{xy}(\omega)\cos\psi}, \tag{4.28}$$

where Δ_p and Δ_s are defined by

$$\Delta_p \equiv Z_t \cos\chi + Z_i \cos\psi + Z_i Z_t \cos\psi\cos\chi\sigma_{xx}(\omega), \tag{4.29}$$

and

$$\Delta_s \equiv Z_t \cos\psi + Z_i \cos\chi + Z_i Z_t \sigma_{xx}(\omega), \tag{4.30}$$

respectively. By dividing the nominator and denominator on the right-hand side of Eq. (4.28) by $1/p_t$, ξ_t is given as follows:

$$\xi_t = \frac{\xi_i \Delta_p + Z_i Z_t \sigma_{xy} \cos\chi}{\Delta_s - \xi_i Z_i Z_t \sigma_{xy} \cos\psi}. \tag{4.31}$$

The property of the reflected light is given by incident and transmitted lights. By eliminating p_t in Eqs. (2.81) and (2.82), and s'_r in Eqs. (2.83) and (2.84), we get

$$p_i \left[K_t \cos\psi - \frac{\cos\chi}{Z_i} \right] = -p_r \left[K_t \cos\psi + \frac{\cos\chi}{Z_i} \right], \tag{4.32}$$

and

$$s'_i \left[K_s - \frac{\cos\psi}{Z_i} \right] = -s'_r \left[K_s + \frac{\cos\psi}{Z_i} \right], \tag{4.33}$$

respectively, where the variables K_t and K_s are defined by

$$K_t \equiv \left[\frac{1}{Z_t} + \sigma_{xx}(\omega) \cos\chi + \sigma_{xy}(\omega) \xi_t \right], \tag{4.34}$$

and

$$K_s \equiv \left[\frac{\cos\chi}{Z_t} + \sigma_{xx}(\omega) - \frac{\sigma_{xy}(\omega) \cos\chi}{\xi_t} \right], \tag{4.35}$$

respectively. By dividing Eq. (4.33) by Eq. (4.32), we get

$$\begin{aligned} \xi_r &= \xi_i \frac{\Delta_p + Z_i Z_t \cos\psi \sigma_{xy}(\omega) \xi_t}{\Delta'_p - Z_i Z_t \cos\psi \sigma_{xy}(\omega) \xi_t} \times \frac{\Delta'_s + Z_i Z_t \cos\chi \sigma_{xy}(\omega)/\xi_t}{\Delta_s - Z_i Z_t \cos\chi \sigma_{xy}(\omega)/\xi_t} \\ &= \frac{\xi_t \Delta'_s + Z_i Z_t \cos\chi \sigma_{xy}(\omega)}{\Delta'_p - Z_i Z_t \cos\psi \sigma_{xy}(\omega) \xi_t}, \end{aligned} \tag{4.36}$$

where we define Δ'_p and Δ'_s as follows:

$$\Delta'_p \equiv Z_t \cos\chi - Z_i \cos\psi - Z_i Z_t \cos\psi \cos\chi \sigma_{xx}(\omega), \tag{4.37}$$

and

$$\Delta'_s \equiv Z_t \cos\psi - Z_i \cos\chi - Z_i Z_t \sigma_{xx}(\omega). \tag{4.38}$$

In the second line of Eq. (4.36), we make use Eq. (4.31) to simplify the expression of ξ_r. Therefore, ξ_r is given as a function of ξ_t, which is at first determined by ξ_i.

Let us calculate the optical absorption probability A for left-handed and right-handed circularly-polarized (LCP and RCP, respectively) lights to demonstrate the occurrences of the CD and VP in the topological and trivial Haldane materials. Here, $p_i = 1$, $s'_i = \pm i$, $\xi_i = \pm i$. By using Eq. (2.90)-(2.92), we identify that for circularly-polarized lights, A is the sum of one-half absorption for p-polarized light A_p and one-half absorption for s-polarized light A_s, as follows:

$$A = \frac{1}{2} A_p + \frac{1}{2} A_s, \tag{4.39}$$

where

$$A_p \equiv 1 - \left[|p_t|^2 \frac{Z_i \cos\chi}{Z_t \cos\psi} + |p_r|^2 \right], \tag{4.40}$$

and

$$A_s \equiv 1 - \left[|s'_t|^2 \frac{Z_i \cos\chi}{Z_t \cos\psi} + |s'_r|^2 \right], \tag{4.41}$$

respectively. By using Eqs. (4.26), (4.27), (4.32), and (4.33), the explicit expressions of A_p and A_s are given by

$$A_p = \frac{4Z_i {Z_t}^2 \cos\psi \cos\chi \mathrm{Re}[\sigma_{xx}(\omega)\cos\chi + \xi_t \sigma_{xy}(\omega)]}{|\Delta_p + \xi_t Z_i Z_t \cos\psi \sigma_{xy}(\omega)|^2}, \tag{4.42}$$

and

$$A_s = \frac{4Z_i {Z_t}^2 \cos\psi \mathrm{Re}[\sigma_{xx}(\omega) - \sigma_{xy}(\omega)\cos\chi/\xi_t]}{|\Delta_s - Z_i Z_t \sigma_{xy}(\omega)\cos\chi/\xi_t|^2}, \tag{4.43}$$

respectively.

In the case of normal incident ($\psi = 0$, $\chi = 0$), $\Delta_p = \Delta_s$ and $\Delta'_p = \Delta'_s$, and from Eqs. (4.31) and (4.36), $\xi_t = \xi_r = \xi_i$. This means that transmitted and reflected lights remain circularly-polarized. In such case that $A_p = A_s$, A reduces to

$$\begin{aligned} A &= \frac{4Z_i {Z_t}^2 \mathrm{Re}\{\sigma_{xx}(\omega) + i\hat{\sigma}\sigma_{xy}(\omega)\}}{|Z_i + Z_t + Z_i Z_t[\sigma_{xx}(\omega) + i\hat{\sigma}\sigma_{xy}(\omega)]|^2} \\ &= \frac{4Z_i {Z_t}^2 [\mathrm{Re}\{\sigma_{xx}(\omega)\} - \hat{\sigma}\mathrm{Im}\{\sigma_{xy}(\omega)\}]}{|Z_i + Z_t + Z_i Z_t\{\sigma_{xx}(\omega) + i\hat{\sigma}\sigma_{xy}(\omega)\}|^2}, \end{aligned} \tag{4.44}$$

where $\hat{\sigma} = +1$ ($\hat{\sigma} = -1$) for LCP (RCP) light. Therefore, for the normal incident, the absorption spectra for circularly-polarized lights are determined by $\mathrm{Re}[\sigma_{xx}(\omega)]$ and $\mathrm{Im}[\sigma_{xy}(\omega)]$.

In Fig. 4.3, we plot the absorption spectra of LCP and RCP lights in undoped ($\epsilon_F = 0$) topological and trivial Haldane materials. The Haldane material is placed in vacuum ($\varepsilon_i = \varepsilon_t = 1$), and the angle of incidence is $\psi = 0$. The absorption probability A for the topological case ($t_2 = 0.05$ eV, $\phi = \pi/2$, and $M = 0$) are shown by the red-dashed line. When the photon energy matches to the band-gap $\hbar\omega = \epsilon_g^{(\kappa)} = 0.52$ eV, the material only absorbs the RCP light ($\hat{\sigma} = -1$), which indicates the phenomenon of perfect CD. This result is consistent with the previous result by Ghalamkari et al. [67], which is obtained within the dipole approximation. However, it should be emphasized that even though perfect CD for RCP occurs, the A for RCP remains relatively low ($\sim 4.4\%$). As we increase the $\hbar\omega$, the A for RCP (LCP) light monotonically decreases (increase), thus CD almost disappears for $\hbar\omega \gg 2$ eV. It is also noted that in the case of $\phi = -\pi/2$, the absorption spectra of RCP and LCP are reversed, because the sign of $\mathrm{Im}[\sigma_{xy}(\omega)]$ changes to negative.

The absorption probability for the trivial Haldane material ($t_2 = 0.05$ eV, $\phi = 0$, and $M = 0.5$ eV) is shown by the blue-dashed-dotted line in Fig. (4.3). Here LCP and

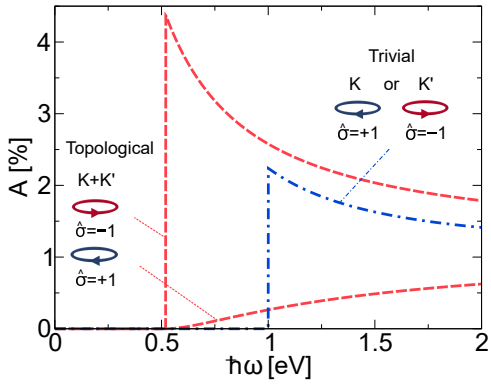

Figure 4.3 Optical absorption probabilities of LCP and RCP lights in the topological ($t_2 = 0.05$ eV, $\phi = \pi/2$, and $M = 0$) and the trivial ($t_2 = 0.05$ eV, $\phi = 0$, and $M = 0.5$ eV) Haldane materials with $\epsilon_F = 0$. The former (later) exhibits CD (VP) [66].

RCP lights are absorbed at the K and the K' valleys, respectively. The absorption spectra indicate the occurrence of VP, which is reversed (i.e. LCP and RCP are absorbed at the K' and the K valleys, respectively) in the case of $M < 0$, because the imaginary part of the Hall conductivity is positive for the K valley and negative for the K' valley. In general, the positive (negative) $\mathrm{Im}[\sigma_{xy}^{(E,\kappa)}(\omega)]$ corresponds to larger absorption for RCP (LCP), which is shown by Eq. (4.44).

Let us discuss the physical origin of the CD. In a study by Harada et al. [109], it is shown by that A in a 2D material can be obtained from the Joule heat Q, which is given by

$$Q = \frac{1}{2}\mathrm{Re}[\boldsymbol{J} \cdot \boldsymbol{E}_h^*], \tag{4.45}$$

where $\boldsymbol{J}$ and $\boldsymbol{E}_h$ are the electric field and surface current density on the 2D material, respectively. By referring to Fig. 2.3, $\boldsymbol{E}_h$ and $\boldsymbol{J}$ are given as follows:

$$\boldsymbol{J} = [\sigma_{xx}E_t^{(p)}\cos\chi + \sigma_{xy}E_t^{(s)}]\hat{\boldsymbol{x}} + [\sigma_{yx}E_t^{(p)}\cos\chi + \sigma_{yy}E_t^{(s)}]\hat{\boldsymbol{y}}, \tag{4.46}$$

and

$$\boldsymbol{E}_h = \cos\psi[E_i^{(p)} + E_r^{(p)}]\hat{\boldsymbol{x}} + [E_i^{(s)} + E_r^{(s)}]\hat{\boldsymbol{y}}, \tag{4.47}$$

respectively. In the case of normal incident $\psi = 0$, the Joule heat for circularly-polarized lights ($\xi_i = \pm i$) is given by

$$Q = \frac{2{Z_t}^2[\mathrm{Re}\{\sigma_{xx}(\omega)\} - \hat{\sigma}\mathrm{Im}\{\sigma_{xy}(\omega)\}]}{|Z_i + Z_t + Z_iZ_t\{\sigma_{xx}(\omega) + i\hat{\sigma}\sigma_{xy}(\omega)\}|^2}{E_0}^2. \tag{4.48}$$

By comparing Eq. (4.48) with Eq. (4.44), we get

$$A_c = 2Z_i\frac{Q}{{E_0}^2}. \tag{4.49}$$

Fig. 4.3: fig/ch4/h-abs.eps

Therefore, the absorption probability is proportional to the Joule heat in the 2D Haldane material, and inversely proportional to the square of the amplitude of electric field E_0. We infer that the perfect CD for RCP in Fig. 4.3 corresponds to the absence of the Joule heat for LCP, and vice versa. We have shown that the broken $\mathcal{T}$ symmetry is physically manifested in the difference of Q for LCP and RCP lights [due to $\sigma_{xy}(\omega)$], hence CD occurs. This phenomenon can be compared (and consistent) with the case of the CD in 2D metamaterials. Khanikaev et al. [110] experimentally observe that LCP and RCP lights generate different amount of the Joule heat in the asymmetric 2D metamaterial, which is attributed to the origin of CD.

4.3 Application of Haldane model on silicene and monolayer TMDs

In this section, we apply the Haldane model to explain CD and VP in silicene and a monolayer TMD, in particular MoS_2. We shall show that by simply changing the parameters t_2, ϕ, and M in the Haldane model, we are able to calculate optical conductivity and absorption probability for a given electronic state in the 2D hexagonal materials.

Silicene is a 2D material in which Si atoms are arranged in honeycomb lattice, or in another words, a silicone analogue of graphene. However, silicene has a buckled structure, in which the sublattices A and B are separated vertically by a distance 2ℓ ($\ell = 0.23$) [111]. By applying an external electric field perpendicular to the silicene plane E_z, a staggered potential between A and B sublattices is generated. Furthermore, Si atom is heavier than C atom, thus, the spin-orbit coupling in silicene ($\lambda = 3.9$ meV) [111, 112, 113, 114] is significantly larger compared with that of graphene ($\lambda = 1.3$ μeV)[112], and should be included in the Hamiltonian. The energy dispersion of silicene around the K and K' points [114] is given by

$$\epsilon(\mathbf{q}) = \mp\sqrt{|\hbar v_{\mathrm{F}}\mathbf{q}|^2 + (e\ell E_z - \kappa s\lambda)^2}, \tag{4.50}$$

where $v_F = \sqrt{3}at_1/2\hbar$, $a_0 = 3.86$ angstrom, $t_1 = 1.6$ eV [113]. The spin index s is $+1$ (-1) for spin-up (spin-down) electron.

Let us first apply the Haldane model on silicene. By substituting $t_2 = \lambda/(3\sqrt{3})$, $M = e\ell E_z$, and $\phi = +\pi/2$ ($\phi = -\pi/2$) in the energy dispersion of the Haldane model [Eq. (2.13)], the state of spin-up (spin-down) electron in silicene given by Eq. (4.50) is reproduced. This model is similar to the Kane-Mele model, which takes account the spin-orbit coupling in graphene [115, 116]. It is noted that silicene undergoes transition from topological to trivial phases at critical electric field $E_{cr} = \lambda/(e\ell)$ [113]. Thus, silicene is a topological (trivial) insulator when E_z is less (greater) than E_{cr}.

First, we consider the 'topological' silicene by setting $E_z = [\lambda/(2e\ell)] < E_{cr}$. In Fig. 4.4(a), we plot energy dispersion of the topological silicene at the K and K' valleys for spin-up ($s = +1$) and spin-down ($s = -1$) electron. At the K (K') valley, the band gap for spin-up is smaller (greater) than that of spin-down electron. In Fig. 4.4(b), we plot the real and imaginary parts of $\sigma_{xx}(\omega)$, which does not depend on the spin index. In the spectra of $\mathrm{Re}[\sigma_{xx}(\omega)]$ and $\mathrm{Im}[\sigma_{xx}(\omega)]$, there are two singularities at different photon energies $\hbar\omega$. The singularity at lower energy corresponds to the interband transitions of spin-up electron at the K valley and spin-down electron at

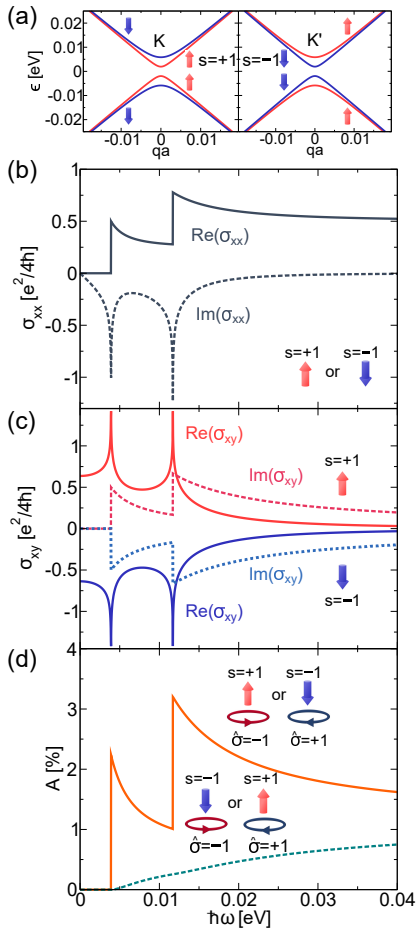

Figure 4.4 (a) Electronic energy dispersion of the topological silicene ($e\ell E_z = \lambda/2 = 1.95$ meV) at the K and K' valleys. The real and imaginary parts of (b) σ_{xx} ($s = \pm 1$) and (c) σ_{xy} ($s = +1$ and $s = -1$). (d) The optical absorptions of LCP ($\hat{\sigma} = +1$) and RCP ($\hat{\sigma} = -1$) lights in the topological silicene ($\epsilon_F = 0$, $\psi = 0$, $\varepsilon_i = \varepsilon_t = 1$) [66].

the K' valley. The singularity at higher energy corresponds to the transitions of spin-down electron at the K valley and spin-up electron at the K' valley. In Fig. 4.4(c) we plot the real and imaginary parts of $\sigma_{xy}(\omega)$ for each spin index, where the signs of $\mathrm{Re}[\sigma_{xy}(\omega)]$ and $\mathrm{Im}[\sigma_{xy}(\omega)]$ are positive for $s = +1$ and negative for $s = -1$. The states $s = +1$ and $s = -1$ belong to the regions i and ii in Fig. 1.6(c), respectively. In Fig. 4.4(d), we plot the absorption spectra of LCP ($\hat{\sigma} = +1$) and RCP ($\hat{\sigma} = -1$) lights for both $s = +1$ and $s = -1$, where we can distinguish two spectra. The absorption spectra for RCP light of spin-up and spin-down electrons are given by orange-solid line and green-dashed lines, respectively. The absorption of spin-up electron is larger than that of spin-down electron. In the case of LCP light, the absorption of a given

Fig. 4.4: fig/ch4/Si-top.eps

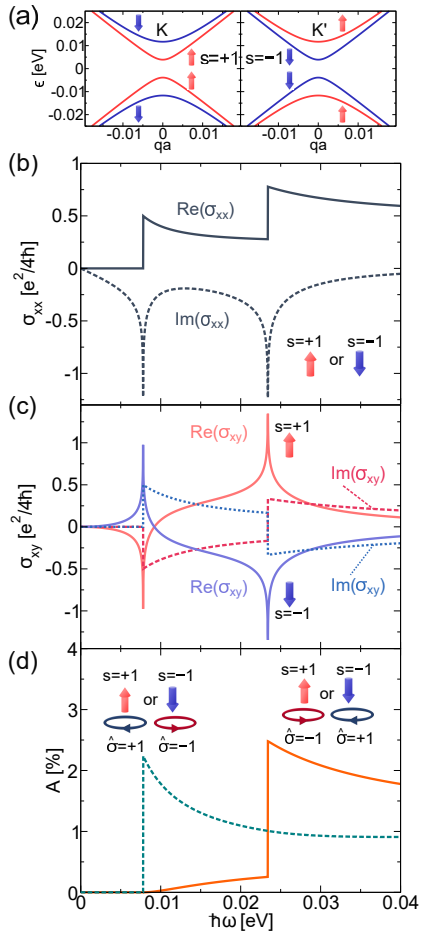

Figure 4.5 (a) Electronic energy dispersion of the trivial silicene ($e\ell E_z = 2\lambda = 7.8$ meV) at the K and K' valleys. The real and imaginary parts of (b) σ_{xx} ($s = \pm 1$) and (c) σ_{xy} ($s = +1$ and $s = -1$). (d) The optical absorption of LCP ($\hat{\sigma} = +1$) and RCP ($\hat{\sigma} = -1$) lights in the trivial silicene ($\epsilon_F = 0$, $\psi = 0$, $\varepsilon_i = \varepsilon_t = 1$) [66].

spin is opposite to the RCP light, where the absorption of spin-down electron (solid line) is higher than that of spin-up electron (dashed-line). Therefore, the absorption of the circularly-polarized light in this case is only determined by the spin index, and does not depend on the valley index.

Now, we consider the 'trivial' silicene by letting $[E_z = 2\lambda/(e\ell)] > E_{cr}$. In Fig. 4.5(a), we plot the electronic energy dispersions of the $s = +1$ and $s = -1$ electrons at the K and K' valleys. Here, we can see that the energy dispersions are similar to those of the topological silicene. The real and imaginary parts of $\sigma_{xx}(\omega)$ are plotted in Fig. 4.5(b), where we can see two singularities for different excitation

Fig. 4.5: fig/ch4/Si-triv.eps

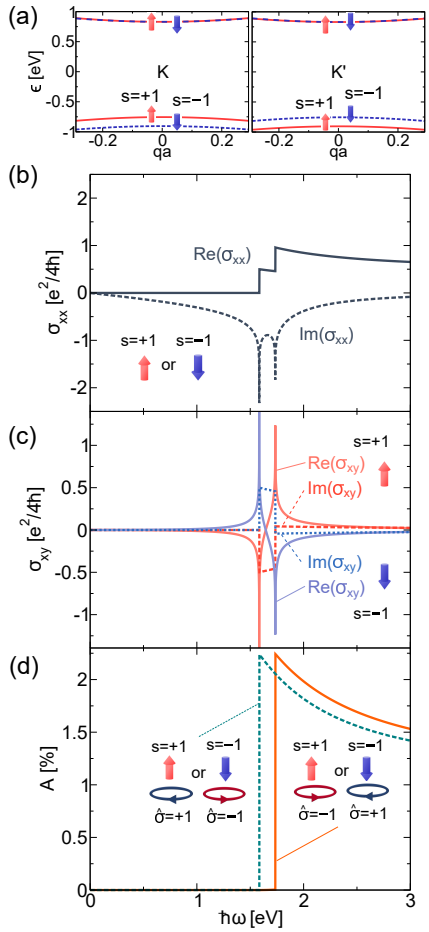

Figure 4.6 (a) Electronic energy dispersion of monolayer MoS_2 at the K and K' valleys. The real and imaginary parts of (b) σ_{xx} ($s = \pm 1$) and (c) σ_{xy} ($s = +1$ and $s = -1$). (d) The optical absorption of LCP ($\hat{\sigma} = +1$) and RCP ($\hat{\sigma} = -1$) lights in the monolayer MoS_2 ($\epsilon_F = 0$, $\psi = 0$, $\varepsilon_i = \varepsilon_t = 1$) [66].

energies. In Fig. 4.5(c), we plot the real and imaginary parts of $\sigma_{xy}(\omega)$ for $s = +1$ and $s = -1$, where the signs of $\mathrm{Re}[\sigma_{xy}]$ and $\mathrm{Im}[\sigma_{xy}]$ of each spin index are opposite at two singular points. The singularities at smaller and larger $\hbar\omega$ correspond to the interband transitions of the spin-up (spin-down) electrons at the K and K' (K' and K) valleys, respectively. In Fig. 4.5(d) we plot the absorption spectra of LCP ($\hat{\sigma} = +1$) and RCP ($\hat{\sigma} = -1$) lights for each spin. The green-dashed line in Fig. 4.5(d) corresponds to the absorption of LCP light by the spin-up electron (at the K valley) or RCP light by the spin-down electron (at the K' valley), while the orange-solid line corresponds to the absorption of RCP light by the spin-up electron (at the K' valley) or LCP light by the spin-down electron (at the K valley). Hence, the absorption of the circularly-polarized

Fig. 4.6: fig/ch4/MoS2-triv.eps

lights is only determined by valley index and not by the spin direction, which indicates the occurrence of VP.

Finally, we apply the Haldane model on the monolayer TMD. In the case of monolayer TMDs such as MoS_2 and WSe_2, we have a direct band gap due to broken $\mathcal{I}$ symmetry. This is because the unit cell consists of one transition-metal atom and two chalcogenide atoms [100, 117]. The d-orbital of the metal contributes to the spin-orbit interaction, which leads to a strong valley-spin coupling [100]. The energy dispersion at the K and K' valleys is given by [118, 119]:

$$\epsilon(\mathbf{q}) = \frac{\kappa s\lambda}{2} \mp \sqrt{|\hbar v_{\rm F}\mathbf{q}|^2 + \left(\frac{\Delta}{2} - \frac{\kappa s\lambda}{2}\right)^2}. \tag{4.51}$$

In particular, for monolayer MoS_2 the Fermi velocity of electron $v_F = at_1/\hbar$, with $a = 3.193$ angstrom, and $t_1 = 1.1$ eV. The energy band gap between valence and conduction bands are $\Delta = 1.66$ eV, and the spin-splitting of energy band at the top of valence band is given by $2\lambda = 0.15$ eV.

By choosing $t_2 = \lambda/(3\sqrt{3})$, $M = \Delta/2$, and $\phi = +5\pi/6$ $(-\pi/6)$ in Eq. (2.13), we reproduce the electronic state of MoS_2 [Eq. (4.51)] for $s = +1$ $(s = -1)$ at the K valley. Similarly for the electron at the K' valley, we choose $\phi = +\pi/6$ $(-5\pi/6)$ to reproduce $s = +1$ $(s = -1)$. Therefore, as in the case of silicene, an electronic state state in the monolayer MoS_2 can be represented by a particular phase angle ϕ in the Haldane model. In Fig. 4.6(a) we plot the energy dispersion of spin-up and spin-down electrons at the K and K' valleys. The splitting between the spin-up and the spin-down electrons at the valence bands is generated by the spin-orbit coupling λ. At the K valley, the upper (lower) valence band is occupied by spin-up (spin-down) electron, which is the opposite of that of the K' valley. The conduction bands are degenerate at the both valleys. In Fig. 4.6(b), the real and imaginary parts $\sigma_{xx}(\omega)$ are shown. Here, the two singularities are separated by $\hbar\omega = 2\lambda = 150$ meV. In Fig. 4.6(c), we plot $\mathrm{Re}[\sigma_{xy}(\omega)]$ and $\mathrm{Im}[\sigma_{xy}(\omega)]$ for each spin index, which change signs at the two different singular points. In Fig. 4.6(d) we plot the absorption spectra for LCP $(\hat{\sigma} = +1)$ and RCP $(\hat{\sigma} = -1)$ lights for each spin index. As in the case of the trivial silicene, the absorption spectra show the occurence of VP.

4.4 Faraday and Kerr rotations in topological Haldane material

In this section, we discuss the Faraday and Kerr rotations in the topological Haldane material. Unless otherwise specified, the topological Haldane material with $t_2 = 0.05$ eV, $M = 0$, and $\phi = \pi/2$ [which was discussed in Sections 4.1 and 4.2 is placed between a substrate $(\varepsilon_i = 3.9)$ and vacuum $(\varepsilon_t = 1)$. The substrate is introduced to enhance the reflection probability. In this geometry, the critical angle for incident light is $\psi_c = \arcsin(\sqrt{1/3.9}) = 30.42°$, above which the total internal reflection occurs $(\psi \geqslant \psi_c)$. The incident light is linearly p-polarized by putting $\xi_i \to 0$ in Eqs. (4.31) and (4.36). By using Eq. (2.113), the Faraday angle $\theta_t = \theta_F$ and the Kerr angle $\theta_r = \theta_K$ are calculated.

Before discussing the Faraday and the Kerr rotations, let us show CD as a function of ψ help us understand calculated results for the ellipticity of transmitted and reflected

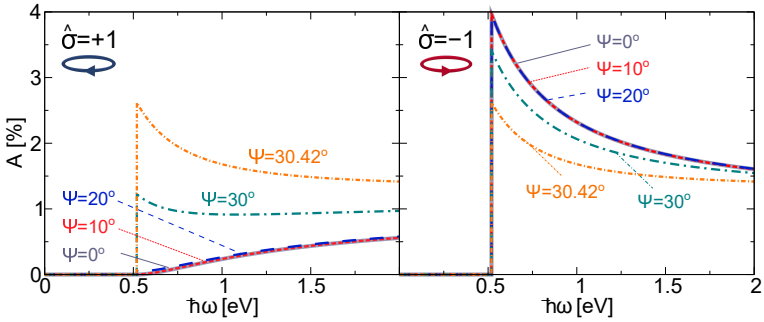

Figure 4.7 Absorption probability A for LCP ($\hat{\sigma} = +1$) and RCP ($\hat{\sigma} = -1$) lights in the topological Haldane material as a function $\hbar\omega$ for several values of $\psi = 0,\ 10,\ 20,\ 30$, and 30.42° [66].

lights. In Fig. 4.7, we plot the absorption probabilities of LCP and RCP lights for several incident angles $\psi = 0,\ 10,\ 20,\ 30$, and 30.42°. The perfect CD occurs at $\hbar\omega = 0.52$ eV (corresponds to the energy gap of the topological Haldane material $\epsilon_g^{(\kappa)}$) for $\psi = 0^\circ$ to $\psi = 20^\circ$. In the case of the perfect CD, ~ 4 % of RCP ($\hat{\sigma} = -1$) light is absorbed and no absorption for the LCP light ($\hat{\sigma} = +1$). At $\psi = 30^\circ$ partial CD is observed, because the absorption probability for LCP and RCP light are ~ 1 % and ~ 3 %, respectively. At the critical angle ($\psi = 30.42^\circ$), CD vanishes, because LCP and RCP are absorbed equally by the Haldane material ($A \sim 2.6\%$).

The phenomenon shown in Fig. 4.7 can be explained by Eqs. (4.39) - (4.43), in which the absorption probability A consists of $A_p \propto \cos\chi[\cos\psi \mathrm{Re}(\sigma_{xx}\cos\chi + \xi_t\sigma_{xy})]$ and $A_s \propto [\cos\psi \mathrm{Re}(\sigma_{xx} - \sigma_{xy}\cos\chi/\xi_t)]$. At small incident angles ($\psi = 0^\circ$ to $\psi = 20^\circ$), $A_p \approx A_s \approx [\mathrm{Re}(\sigma_{xx}) - \hat{\sigma}\mathrm{Im}(\sigma_{xy})]$, which corresponds to the perfect CD [see Eq. (4.44)]. As ψ increases, χ becomes larger by the Snell law. Consequently, the contribution of the A_p term decreases. From Fig. 4.7, it is noted that for $\psi = 0 - 20^\circ$, the change of A is not pronounced for both LCP and RCP lights, because the $\cos\chi$ does not vary significantly. At the critical angle, we have $\chi = 90^\circ$, and thus $A_p = 0$ and $A_s \propto [\cos\psi \mathrm{Re}(\sigma_{xx})]$. This means that A for both LCP and RCP lights only depend on the longitudinal conductivity $\sigma_{xx}(\omega)$ and not on the Hall conductivity $\sigma_{xy}(\omega)$. Since $\mathrm{Im}[\sigma_{xy}]$ is essential for CD, at the critical angle of incident ψ_c, CD can not occur.

In Fig. 4.8(a) we plot the Faraday rotation θ_F as a function of photon energy $\hbar\omega$ for several values of incident angles $\psi = 0,\ 10,\ 20,\ 30$, and 30.42°. In the figure, it is shown that the Faraday rotation has a singular point at $\hbar\omega = \epsilon_g^{(\kappa)} = 0.52$ eV. In Fig. 4.8(b) the ellipticity of the transmitted light $\eta_t = \eta_F$ for the corresponding ψ's are shown. Here, the ellipticity increases at $\hbar\omega \geqslant \epsilon_g^{(\kappa)}$ and decreases for the higher photon energy. The origin of the singularities in θ_F and η_F can be explained by Eq. (4.31). In the limit $\xi_i \to 0$, $\xi_t = \xi_\mathrm{F}$ reduces to

$$\lim_{\xi_i \to 0} \xi_F = \frac{Z_i Z_t \sigma_{xy} \cos\chi}{\Delta_s}. \tag{4.52}$$

Fig. 4.7: fig/ch4/haldane-cd.eps

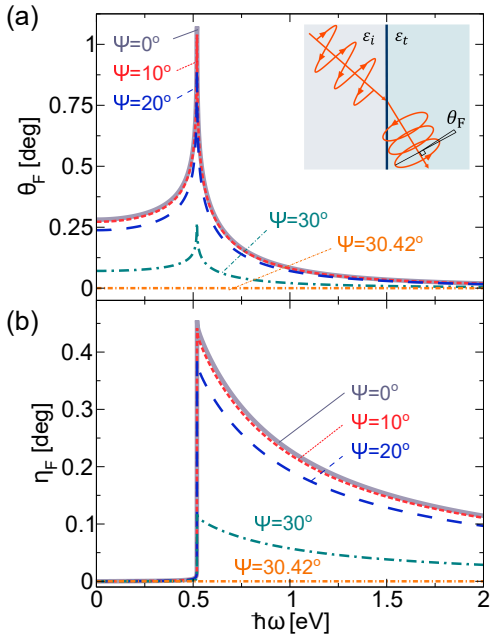

Figure 4.8 (a) The Faraday rotation θ_F and (b) ellipticity of the transmitted light η_F as a function of $\hbar\omega$ for several values of $\psi = 0,\ 10,\ 20,\ 30$, and $30.42°$. Inset in (a) illustrates the Faraday rotation [66].

By substituting Eq. (4.52) to Eqs. (2.113) and (2.108), we find proportional relations $\theta_F \propto \mathrm{Re}[\sigma_{xy}]$ and $\eta_F \propto \mathrm{Im}[\sigma_{xy}]$. Therefore, the singularities in θ_F and η_F originate from the singular points in the real and imaginary parts of $\sigma_{xy}(\omega)$, respectively, when $\hbar\omega = \epsilon_g^{(\kappa)}$.

The largest $\theta_F \sim 1°$ is observed for the normal incident ($\psi = 0°$), and θ_F decreases as ψ increases to ψ_c. This occurs because ξ_F is also proportional to $\cos\chi$. As for the ellipticity of transmitted light, it is shown that the largest $\eta_F \approx 0.45°$ is also obtained at $\psi = 0°$, which indicates that the transmitted light is almost linearly-polarized, because only $\sim 4\%$ of the RCP light are absorbed, while no absorption for LCP light (see Fig. 4.7). Therefore, after the transmission, the intensity of the LCP light is slightly higher than the RCP light, which implies the positive ellipticity ($\eta_F > 0$) in the transmitted light. It can be shown that η_F is non-zero if there is CD. By using Eq. (4.44), the difference of A between LCP ($\hat{\sigma} = +1$) and RCP ($\hat{\sigma} = -1$) lights is given by

$$\mathrm{CD} = A_+ - A_- \propto -2\mathrm{Im}[\sigma_{xy}], \tag{4.53}$$

which is similar to the case η_F, but has the opposite sign. Thus, when CD for LCP (RCP) light occurs, the transmitted light will acquires negative (positive) helicity. At $\psi = \psi_c = 30.42°$, the absorption probability LCP and RCP lights are equal as

Fig. 4.8: fig/ch4/faraday-rot.eps

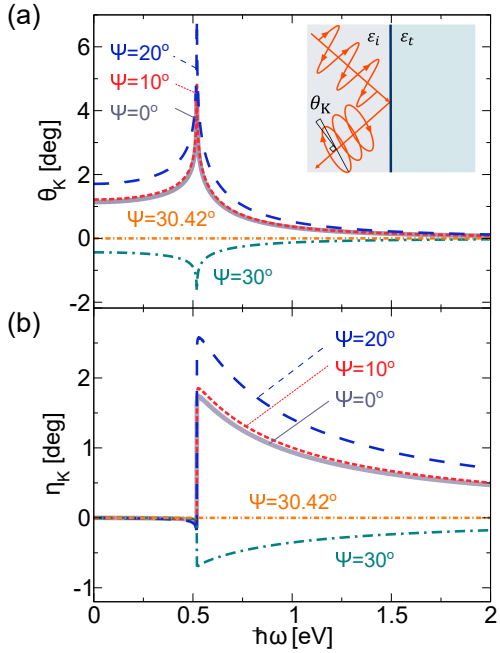

Figure 4.9 (a) The Kerr rotation θ_K and (b) ellipticity of the reflected light η_K as a function of $\hbar\omega$ for several values of $\psi = 0,\ 10,\ 20,\ 30,$ and $30.42°$. Inset in (a) illustrates the Kerr rotation [66].

shown in Fig. 4.7, which implies that the transmitted light remains linearly-polarized ($\eta_F = 0$).

In Fig. 4.9(a) and (b), we plot the Kerr rotation θ_K and the ellipticity of reflected light η_K, respectively, as a function of $\hbar\omega$ for $\psi = 0,\ 10,\ 20,\ 30,$ and $30.42°$. Again, singularities occur when at $\hbar\omega = \epsilon_g^{(\kappa)} = 0.52$ eV. However, at $\psi = 0°$ to $\psi = 20°$, both θ_K and η_K also increase, contrary to the case of the transmitted light. We can see that the magnitudes of the Kerr rotation ($\theta_K \sim 4°$ to $6°$) are significantly larger than the Faraday rotation ($\theta_F \leqslant 1°$), and the reflected light is more elliptical (η_K up to $2°$) than that of the transmitted light ($\eta_F < 0.5°$). At $\psi = 30°$, θ_K and η_K become negative. This phenomenon can be explained by substituting $\xi_i \to 0$ and Eq. (4.52) into Eq. (4.31). In the limits, $\xi_r = \xi_K$ can be simplified as follows:

$$\lim_{\xi_i \to 0} \xi_K = 2Z_t \cos\psi \frac{\Delta_p + [Z_i Z_t \sigma_{xy}]^2 \cos\psi \cos\chi/\Delta_s}{\Delta_p' - [Z_i Z_t \sigma_{xy}]^2 \cos\psi \cos\chi/\Delta_s}. \tag{4.54}$$

The negative sign of ξ_K originate from the the fact that Δ_p' can be less than zero [see Eq. (4.37)], which means that the p-components of the electric fields of the reflected and incident lights have have phase difference of π [93]. The direction of the Kerr rotation and the ellipticity of the transmitted lights are reversed, therefore $\theta_K < 0$ and $\eta_K < 0$. At the critical angle $\psi = 30.42°$ ($\chi = 90°$), the variable ξ_K in Eq. (4.54)

Fig. 4.9: fig/ch4/kerr-rot.eps

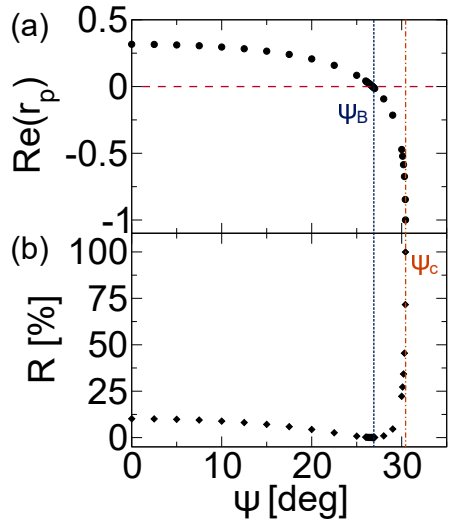

Figure 4.10 (a) The real part reflection coefficient $\mathrm{Re}(r_p)$ and (b) reflection probability R in the topological Haldane material as a function of ψ at $\hbar\omega = 0.52$ eV. The vertical dashed and dash-dotted lines indicate the Brewster and critical angles, ψ_B and ψ_c, respectively.

reduces to $\xi_K \approx 2Z_t \cos\psi\Delta_p/\Delta'_p$, which does not consist the Hall conductivity $\sigma_{xy}(\omega)$. This implies the reflected light does not undergo the rotation of polarization plane, and hence the absence of the Kerr rotation ($\theta_K = 0$).

In order to understand in a more detail change of θ_K as a function of ψ, let us consider the reflection coefficient for the p-component of light, $r_p \equiv p_r/p_i$. The r_p is obtained by solving Eq. (4.32) as follows:

$$r_p = \frac{\Delta'_p - Z_i Z_t \cos\psi\sigma_{xy}(\omega)\xi_t}{\Delta_p + Z_i Z_t \cos\psi\sigma_{xy}(\omega)\xi_t}. \tag{4.55}$$

By using Eq. (2.91), the reflection probability R is related to r_p by

$$R = |r_p|^2 \frac{(1+|\xi_r|^2)}{(1+|\xi_i|^2)}. \tag{4.56}$$

In Fig. (4.10)(a) and (b), we plot the real part reflection coefficient $\mathrm{Re}(r_p)$, and the reflection probability R, respectively, as a function of angle of incidence ψ at the resonant photon energy $\hbar\omega = 0.52$ eV. We can see that $\mathrm{Re}(r_p)$ changes sign at $\psi = \psi_B \approx 26.75°$. The ψ_B is known as the *Brewster angle*, in which the reflected light has no p-component and thus becomes s-polarized. Since $r_p \propto p_r = 0$ and $\xi_r \to \infty$ [see Eq. (2.85)], the angle of the Kerr rotation θ_K at ψ_B becomes very large ($\theta_K \sim 90°$) [see Eq. (2.113)]. Nevertheless, at this point, the reflection probability R is almost zero ($R \approx 0.07$ %). Therefore, even though we can obtain the maximum Kerr rotation up to 90° at the Brewster angle, this phenomenon is difficult to observe due to the low reflection probability.

Fig. 4.10: fig/ch4/brewster.eps

Chapter 5

Magnetizations and de Haas-van Alphen oscillations in 2D materials

In this chapter, we derive analytical expressions of thermodynamic potential Ω and magnetization M of the Dirac fermions as a function of magnetic field B, temperature T, and chemical potential μ. In the derivations, we employ the technique of zeta function regularization for the infinite summation of the Landau levels (LLs), in order to avoid the divergence in the Ω. In the case of undopped ($\mu = 0$) graphene, we show that $M = C_1 T - C_2\sqrt{B}$ in the strong B/low T limit, where C_1 and C_2 are constants. We identify that the T-dependences is originated from the entropy of electrons occupying the zeroth LLs from the K and the K' valley. In the weak B/high T limit, on the other hand, we find that $M \propto -B/T$ because of the thermal excitation of electrons from valence to conduction bands. The formulae for M reproduce the experimental data by Li et. al [78], which are empirically fitted into a Langevin function. Furthermore, we generalize the result by considering the effects of impurity on orbital susceptibility of graphene. In particular, we show that in the presence of impurity, the susceptibility follows a scaling law, which is approximately described by the so-called Faddeeva function. In the case of massive Dirac fermions such as monolayer transition-metal dichalcogenide, we show that a large band gap gives a robust magnetization and susceptibility with respect to temperature and impurity.

Finally, we discuss the de Haas-van Alphen (dHvA) oscillation at $T = 0$ K for both cases of fixed μ and fixed electron density N. We show that for a fixed μ, the opening of the band gap decreases both frequency and amplitude of the dHvA oscillation. For the fixed N, the dHvA oscillation possesses an equal frequency but different phase to that of the case for the fixed μ.

5.1 Thermodynamic potential and magnetization of massive Dirac fermion]$T = 0$ K, any Δ, λ, and μ [

Firs, we derive thermodynamic potential of massive Dirac fermions at $T = 0$ K, which is applicable for gapped graphene and transition-metal dichalcogenides (TMDs). The Landau level (LL) of the massive Dirac fermions is given by Eq. (3.12). Since we consider electron-doped system, we set $\mu \geqslant \Delta/2$. The thermodynamic potential for

the occupied LLs at the valence bands, Ω_- [see Eq. (3.15)] is given by

$$\begin{aligned}\Omega_- &= -\frac{1}{\beta}\frac{eB}{h}\sum_{\xi=\pm}\left[\sum_{n=0}^{\infty}+\sum_{n=1}^{\infty}\right]\ln[1+e^{-\beta(\epsilon_{-n}^{\xi}-\mu)}] \\ &= \frac{eB}{h}\sum_{\xi=\pm}\left[\sum_{n=0}^{\infty}+\sum_{n=1}^{\infty}\right]\left[\frac{\xi\lambda}{2}-\hbar\omega_c\sqrt{n+{\Gamma_\xi}^2}-\mu\right] \\ &= \frac{eB}{h}\sum_{\xi=\pm}\left[\frac{\xi\lambda}{2}+2\sum_{n=1}^{\infty}\frac{\xi\lambda}{2}-\mu-2\sum_{n=1}^{\infty}\mu+\frac{\Delta_\xi}{2}-2\hbar\omega_c\sum_{n=0}^{\infty}\sqrt{n+{\Gamma_\xi}^2}\right],\end{aligned} \tag{5.1}$$

where the summation on n which begins from $n = 0$ ($n = 1$) operates on the LLs at the K (K') valley [see Fig. (3.2)], and we define $\Gamma_\xi \equiv \Delta_\xi/(2\hbar\omega_c)$. It is noted that the logarithm function in the first line of Eq. (5.1) is approximated by $\ln[1 + \exp\{-\beta(\epsilon_{-n}^{\xi}-\mu)\}] \approx -\beta(\epsilon_{-n}^{\xi}-\mu)$, which is valid for $-(\epsilon_{-n}^{\xi}-\mu) \gg k_BT$, or $T \to 0$ K. In the third line of Eq. (5.1), we have shifted the index of the summation for the term $-\hbar\omega_c\sqrt{n+{\Gamma_\xi}^2}$ from $n = 1$ to $n = 0$ in order to adopt the Hurwitz zeta function $\zeta(p, q)$, while the first and the second infinite summations are regularized by using the Riemann zeta function $\zeta(p)$ [see Appendix A]. Thus, Ω_- is given by

$$\Omega_- = -2\frac{eB}{h}\sum_{\xi=\pm}\left[\hbar\omega_c\zeta\Big(-\frac{1}{2},{\Gamma_\xi}^2\Big)-\frac{\Delta_\xi}{4}\right]. \tag{5.2}$$

Here, we have used $\zeta(0) = -1/2$, which implies that the terms $\xi\lambda/2$ and μ in Eq. (5.1) disappear in the final expression in Ω_-. Therefore, for electron-doped system, Ω_- does not depend on the doping level. Eq. (5.2) gives the intrinsic diamagnetism of the Dirac fermions. Sharapov et al. [102] have derived a similar result for gapped graphene, which is obtained by introducing an ultraviolet cut-off in the calculation of the thermodynamic potential.

For a heavy fermion ($\Delta_\xi/2 \gg k_BT$), Eq. (5.2) can be simplified by the asymptotic form of $\zeta(p, q)$ for $q \to \infty$ and $p \neq 1$ [74] as follows:

$$\zeta(p,q) \sim \frac{q^{1-p}}{p-1}+\frac{q^{-p}}{2}+\frac{1}{12}pq^{-(1+p)}. \tag{5.3}$$

By using Eq. (5.3), Eq. (5.2) reduces to

$$\Omega_- \approx \sum_{\xi=\pm}\left(\frac{1}{24\pi}\frac{{\Delta_\xi}^3}{(\hbar v_F)^2}+\frac{eB}{h}\frac{(\hbar\omega_c)^2}{6\Delta_\xi}\right). \tag{5.4}$$

From the second term in the right-hand side of Eq. (5.4), we can see that Ω_- has B^2 dependence (${\omega_c}^2 \propto B$), which implies the linear-B dependence of M for the heavy Dirac fermion, as follows:

$$M \approx -\frac{(ev_F)^2B}{3\pi}\sum_{\xi=\pm1}\frac{1}{\Delta_\xi}. \tag{5.5}$$

It is noted that Eq. (5.5) prevails for undoped case, because we do not include the contribution of the LLs at the conduction bands.

Let us we consider the thermodynamic potential for the occupied LLs at the conduction bands $\Omega_+^{(e)}$. We introduce the Heaviside function $\Theta(\mu - \Delta/2)$ as a threshold to make sure that $\Omega_+^{(e)}$ is relevant when the doping level is larger than the band gap, as follows:

$$\begin{aligned}
\Omega_+^{(e)} &= -\frac{1}{\beta}\frac{eB}{h}\sum_{\xi=\pm}\left[\sum_{n=0}^{\nu_\xi}+\sum_{n=1}^{\nu_\xi}\right]\ln[1+e^{-\beta(\epsilon_n^\xi-\mu)}]\Theta(\mu-\Delta/2) \\
&= \frac{eB}{h}\sum_{\xi=\pm}\left[\sum_{n=0}^{\nu_\xi}+\sum_{n=1}^{\nu_\xi}\right]\left[\frac{\xi\lambda}{2}+\hbar\omega_c\sqrt{n+{\Gamma_\xi}^2}-\mu\right] \\
&= -2\frac{eB}{h}\sum_{\xi=\pm}\left[\frac{\Delta}{4}+\mu\Big(\nu_\xi+\frac{1}{2}\Big)-\frac{\xi\lambda}{2}(\nu_\xi+1)\right. \\
&\quad \left.+\hbar\omega_c\left\{\zeta\Big(-\frac{1}{2},{\Gamma_\xi}^2+\nu_\xi+1\Big)-\zeta\Big(-\frac{1}{2},{\Gamma_\xi}^2\Big)\right\}\right]\Theta(\mu-\Delta/2).
\end{aligned} \tag{5.6}$$

The summation from $n = 0$ ($n = 1$) operates on the LLs at the $K' = (K)$ valley. In the third line of Eq. (5.6), the finite summation of the LLs is expressed by a subtraction of two zeta functions as follows [74]:

$$\sum_{n=0}^{N}(n+q)^{-p} = \zeta(p,q)-\zeta(p,q+N+1). \tag{5.7}$$

In Appendix A.3, we confirm that the numerical calculation of the left-hand side of Eq. (5.7) reproduces the analytical expression on the right-hand side. Therefore, for electron-doped system, the total thermodynamic potential Ω [Eq. (3.15)] is obtained by substituting by Eqs. (5.2) and (5.6) for Ω_- and $\Omega_+^{(e)}$, respectively. In Appendix B, we discuss the case for hole-doped system, in which we show that in the absence of the spin-orbit coupling ($\lambda = 0$), the electron- and hole-doped systems possess an identical Ω due to the electron-hole symmetry.

The results given by Eqs. (5.2) and (5.6) will be used to obtain the magnetization M of the massive Dirac fermions for both undoped and doped cases at $T = 0$ K. In particular, we will discuss the effect of band gap Δ on the period and amplitude of the de Haas-van Alphen (dHvA) oscillations.

5.2 Thermodynamic potential and magnetization of massive Dirac fermion [$k_BT \gg (\hbar\omega_c \sim \Delta)$, $\lambda = 0$, any μ]

In this section, we derive thermodynamic potential of a gapped graphene in the case when the thermal energy k_BT is much larger than the cyclotron energy $\hbar\omega_c$ and the band gap Δ. We remind the readers that since we do not have spin-orbit coupling, we set $\lambda = 0$ and drops the index ξ [see Eq. (3.12)]. Here, the LL is given by $\epsilon_n = \mathrm{sgn}_\tau(n)\sqrt{(\hbar\omega_c)^2|n| + (\Delta/2)^2} = \mathrm{sgn}_\tau(n)\hbar\omega_c\sqrt{|n|+\Gamma^2}$. Since $\hbar\omega_c \sim \Delta \ll k_BT$, we

expand the logarithmic and the exponential functions to derive Ω_- as follows:

$$\begin{aligned}
\Omega_- &= -\frac{g_s}{\beta}\frac{eB}{h}\left[\sum_{n=0}^{\infty}+\sum_{n=1}^{\infty}\right]\ln[1+e^{-\beta(\epsilon_{-n}-\mu)}] \\
&= -\frac{g_s}{\beta}\frac{eB}{h}\left[\sum_{n=0}^{\infty}+\sum_{n=1}^{\infty}\right]\sum_{k=1}^{\infty}\frac{(-1)^{k-1}}{k}e^{\beta\mu k}\exp(-\beta\epsilon_{-n}k) \\
&= \frac{g_s}{\beta}\frac{eB}{h}\left[\sum_{n=0}^{\infty}+\sum_{n=1}^{\infty}\right]\sum_{k=1}^{\infty}\frac{(-e^{\beta\mu})^k}{k}\sum_{l=0}^{\infty}\frac{(-\beta\epsilon_{-n}k)^l}{l!} \\
&= \frac{g_s}{\beta}\frac{eB}{h}\sum_{l=0}^{\infty}\sum_{k=1}^{\infty}\frac{(-e^{\beta\mu})^k}{k^{1-l}}\frac{(\beta\hbar\omega_c)^l}{l!}\left[2\sum_{n=0}^{\infty}(n+\Gamma^2)^{l/2}-\Gamma^l\right] \\
&= \frac{2g_s}{\beta}\frac{eB}{h}\sum_{l=0}^{\infty}\mathrm{Li}_{1-l}(-e^{\beta\mu})\frac{(\beta\hbar\omega_c)^l}{l!}\left[\zeta\Big(\frac{-l}{2},\Gamma^2\Big)-\frac{\Gamma^l}{2}\right].
\end{aligned} \tag{5.8}$$

In the fourth line of Eq. (5.8), we switch the order of summations with indices k and l in order to express the μ dependence of Ω_- in term of the polylogarithm function $\sum_{k=1}^{\infty}(-e^{\beta\mu})^k/k^{1-l} = \mathrm{Li}_{1-l}(-e^{\beta\mu})$ [74], and we shift the summation on n which begins from $n=1$ to $n=0$ in order to adopt the Hurwitz zeta function.

In the calculation of $\Omega_+^{(e)}$, first we express $\Omega_+^{(e)} = \Omega_+ - \Omega'_+$, where Ω_+ (Ω'_+) is the thermodynamic potential for the entire (unoccupied) LLs at the conduction bands (see Fig. 3.2). We shall show that Ω'_+ is negligible for $\hbar\omega_c \ll \mu \ll k_BT$, which indicates that electrons can occupy indefinite number of the LLs at the conduction bands by the thermal excitation. Let us first derive $\Omega'_{+0} \equiv \Omega'_+(T=0\text{ K})$ as follows:

$$\begin{aligned}
\Omega'_{+0} &= 2g_s\frac{eB}{h}\sum_{n=\nu+1}^{\infty}[\epsilon_n-\mu] \\
&= 2g_s\frac{eB}{h}\left[\hbar\omega_c\zeta\Big(-\frac{1}{2},\Gamma^2+\nu+1\Big)+\Big(\nu+\frac{1}{2}\Big)\mu\right],
\end{aligned} \tag{5.9}$$

where the factor 2 represents valley degeneracy. In the second line of Eq. (5.9) we use $\sum_{n=\nu+1}^{\infty} = \zeta(0) - \sum_{n=1}^{\nu} = -(1/2+\nu)$ [see Appendix A]. By considering $\mu \gg \hbar\omega_c$, we get $\Gamma^2+\nu+1 \approx \mu^2/(\hbar\omega_c)^2$. By applying Eq. (5.3) on the zeta function in Eq. (5.9), and noting that

$$\zeta(p,q+1) = \zeta(p,q) - p^{-q}, \tag{5.10}$$

Ω'_{+0} is approximately given by

$$\Omega'_{+0}(\mu) \approx \frac{1}{2\pi}\frac{g_s}{(\hbar v_F)^2}\left[\frac{\mu^3}{3}-\frac{\Delta^2\mu}{4}-\frac{(\hbar\omega_c)^4}{24\mu}\right]. \tag{5.11}$$

For any $T > 0$ K, Ω'_+ is obtained from the convolution of Ω'_{+0} with $(-\partial f/\partial\varepsilon) = \beta\mathrm{sech}^2[\beta(\varepsilon-\mu)/2]/4$, where $f(\varepsilon)$ is the Fermi distribution function [24], as follows:

$$\Omega'_+(\mu) = \frac{\beta}{4}\int_{-\infty}^{\infty} d\varepsilon\ \Omega'_{+0}(\varepsilon)\ \mathrm{sech}^2\Big[\frac{\beta}{2}(\varepsilon-\mu)\Big]. \tag{5.12}$$

Here, $\Omega'_{+0}(\varepsilon)$ is given by substituting μ in Eq. (5.11) to the variable ε. It is noted that $\Omega'_{+0}(\varepsilon)$ is an odd function of ε, and for $\mu \ll k_BT$, the function $\mathrm{sech}^2[\beta(\varepsilon-\mu)/2]$ can be approximated as an even function. Thus, $\Omega'_{+}(\mu) \approx 0$ in the case of $\hbar\omega_c \ll \mu \ll k_BT$, which implies $\Omega_+^{(e)} \approx \Omega_+$. This means that for $k_BT \gg (\hbar\omega_c \sim \Delta)$, the entire LLs at the valence and conduction bands should be included in the calculation of Ω. By the similar procedure to derive Ω_- in Eq. (5.8), Ω_+ is given by

$$\Omega_+ = \frac{2g_s}{\beta}\frac{eB}{h}\sum_{l=0}^{\infty}\mathrm{Li}_{1-l}(-e^{\beta\mu})\frac{(-\beta\hbar\omega_c)^l}{l!}\left[\zeta\Big(\frac{-l}{2},\Gamma^2\Big) - \frac{\Gamma^l}{2}\right]. \tag{5.13}$$

When we add Eqs. (5.8) and (5.13) to obtain $\Omega = \Omega_- + \Omega_+$, The odd l terms disappear, while the even l terms such as $l = 0,\ 2,\ 4, ...$ are doubled. By expressing $l = 2\ell$, Ω is given by

$$\begin{aligned}\Omega &= \frac{4g_s}{\beta}\frac{eB}{h}\sum_{\ell=0}^{\infty}\mathrm{Li}_{1-2\ell}(-e^{\beta\mu})\frac{(\beta\hbar\omega_c)^{2\ell}}{(2\ell)!}\left[\zeta(-\ell,\Gamma^2) - \frac{\Gamma^{2\ell}}{2}\right] \\ &\equiv \sum_{\ell=0}^{\infty}\Omega_\ell.\end{aligned} \tag{5.14}$$

Let us expand the terms $\ell = 0$ and $\ell = 1$ in the second line of Eq. (5.14) to make clear the dependence of Ω on B. For $\ell = 0$, by using the identities $\zeta(0, x) = 1/2 - x$ (see Appendix A) and $\mathrm{Li}_1(z) = -\ln(1 - z)$ [74], Ω_0 in Eq. (5.14) is given by

$$\Omega_0 = k_BT\frac{g_s}{4\pi}\frac{\Delta^2}{(\hbar v_F)^2}\ln[1 + e^{\beta\mu}]. \tag{5.15}$$

Hence, Ω_0 is proportional to the square of band gap Δ^2, and is linearly dependent on temperature T. As for $\ell = 1$, by using $\mathrm{Li}_{-1}(z) = z/(1 - z)^2$ (here, $\mathrm{Li}_{-1}(-e^{\beta\mu}) = \mathrm{sech}^2[\mu/(2k_BT)]/4$), and $\zeta(-1, x) = -(1/2)(x^2 - x + 1/6)$ [74], Ω_1 is given by

$$\Omega_1 = \frac{g_s}{\pi k_BT}\mathrm{sech}^2\Big(\frac{\mu}{2k_BT}\Big)\left[\frac{\Delta^4}{256(\hbar v_F)^2} + \frac{(v_FeB)^2}{24}\right]. \tag{5.16}$$

Therefore, the leading factor of Ω which depends on magnetic field is proportional to B^2. The terms which consist of Δ in the expressions of Ω_0 and Ω_1 can be interpreted as a fraction of energy required to excite electrons from the valence to conduction bands across the band gap.

By using Eq. (5.14), M of the gapped graphene can be approximated by

$$M \approx -\frac{(ev_F)^2B}{6\pi k_BT}\mathrm{sech}^2\Big(\frac{\mu}{2k_BT}\Big). \tag{5.17}$$

5.3 Thermodynamic potential and magnetization of graphene [$k_BT \ll \hbar\omega_c$ or $k_BT \gg \hbar\omega_c$, $\Delta = 0$, $\lambda = 0$, any μ]

In this Section, we derive Ω and M of graphene for low T/strong B ($k_BT \ll \hbar\omega_c$) and high T/weak B ($k_BT \gg \hbar\omega_c$) limits. We shall show that our formulae reproduce an

experimental result by Li et al. [78] on the dependence of M on B and T. The LL of graphene is given by $\epsilon_n = \mathrm{sgn}_\tau(n)\hbar\omega_c\sqrt{n}$. The zeroth LLs $\epsilon_0 = 0$ are shared between the valence and conduction bands at the K and K' valleys, respectively, which is half-occupied at $T = 0$ K and $\mu = 0$.

By separating the contributions of the zeroth LLs from the $n \neq 0$ LLs, Ω_- and $\Omega_+^{(e)}$ for $\hbar\omega_c \gg k_BT$ are given as follows:

$$\begin{aligned}\Omega_- &= -\frac{g_s}{\beta}\frac{eB}{h}\left[\ln\{1+e^{\beta\mu}\} + 2\sum_{n=1}^{\infty}\ln\{1+e^{\beta(\hbar\omega\sqrt{n}+\mu)}\}\right] \\ &= -2g_s\frac{eB}{h}\left[\frac{1}{2\beta}\ln\{1+e^{\beta\mu}\} + \hbar\omega_c\zeta\Big(-\frac{1}{2},1\Big) - \frac{\mu}{2}\right],\end{aligned} \tag{5.18}$$

and

$$\begin{aligned}\Omega_+^{(e)} &= -\frac{g_s}{\beta}\frac{eB}{h}\left[\ln\{1+e^{\beta\mu}\} + 2\sum_{n=1}^{\nu}\ln\{1+e^{-\beta(\hbar\omega\sqrt{n}-\mu)}\}\right] \\ &= -2g_s\frac{eB}{h}\left[\frac{1}{2\beta}\ln\{1+e^{\beta\mu}\} + \mu\nu + \hbar\omega_c\left\{\zeta\Big(-\frac{1}{2},1+\nu\Big) - \zeta\Big(-\frac{1}{2},1\Big)\right\}\right],\end{aligned} \tag{5.19}$$

respectively. It is noted that by putting $T \to 0$ K, Eqs. (5.2) and (5.6) reduce to Eqs. (5.18) and (5.19) for $\Delta = \lambda = 0$. In the undoped graphene ($\mu = 0$), only the first term in the left-hand side of Eq. (5.19) survives, and therefore Ω is given by

$$\begin{aligned}\Omega(\mu=0) &= -2g_s\frac{eB}{h}\left[\hbar\omega_c\zeta\Big(-\frac{1}{2},1\Big) + \frac{1}{\beta}\ln(2)\right] \\ &\equiv \Omega_B + \Omega_S.\end{aligned} \tag{5.20}$$

Since Ω at $\mu = 0$ can be equivalently expressed by $\Omega = E - TS$, where E is internal energy and S is entropy, we identify that Ω_B and Ω_S in Eq. (5.20) are the potentials associated with E of the $n < 0$ LLs and S of the $n = 0$ LLs, respectively. The origin of the $\ln 2$ factor in the expression of Ω_S is two freedoms per valley, spin, and the LL degeneracies of the zeroth LLs. We justify this statement as follows. The general formula for the entropy is given by $S = (\text{degeneracies}) \times k_B \ln W$, where W is the number of freedoms for occupying one electron. Because the states of the zeroth LL consist of valence (K valley) and conduction (K' valley) bands, the electron acquires two possible freedoms, i.e. for occupying the zeroth LL from the valence band while that of the conduction band is empty, and vice versa ($W = 2$). In principle, we can not distinguish the two freedoms. This argument also explains that $n < 0$ LLs do not contribute to the entropy because they are fully occupied ($W = 1$).

In the case of $\hbar\omega_c \ll k_BT$, Ω is obtained from Eq. (5.14) by putting $\Gamma = 0$, as follows:

$$\Omega = -\frac{4g_s}{\beta}\frac{eB}{h}\sum_{\ell=1}^{\infty}\mathrm{Li}_{1-2\ell}(-e^{\beta\mu})\frac{(\beta\hbar\omega_c)^{2\ell}}{(2\ell)!}\frac{\mathcal{B}_{\ell+1}}{\ell+1}, \tag{5.21}$$

Here, $\mathcal{B}_{\ell+1}$ is the Bernoulli number which is related to the zeta function by $\zeta(-\ell, 0) = -\mathcal{B}_{\ell+1}/(\ell+1)$ for $\ell \geqslant 1$ (see Appendix A.2 for derivation). The summation of ℓ in Eq. (5.21) begins from $\ell = 1$, because the term $\ell = 0$ in Eq. (5.14) does not depend on B and is proportional to Δ^2, thus for graphene $\Omega_0 = 0$ [see Eq. (5.15)]. M of graphene for a given μ is given by

$$M = \frac{4g_s}{\beta}\frac{e}{h}\sum_{\ell=1}^{\infty}\mathrm{Li}_{1-2\ell}(-e^{\beta\mu})\frac{(2\hbar {v_F}^2 e\beta^2 B)^\ell}{(2\ell)!}\mathcal{B}_{\ell+1}. \tag{5.22}$$

It is important to note that by differentiating Eq. (5.22) on B, we reproduce the formula for susceptibility of graphene by McClure [24] in Eq. (1.32), which is derived by using cut-off of the LLs at the conduction bands. Here, Eq. (1.32) is valid for any temperature $T > 0$ K because we take $B = 0$ to calculate χ, thus the condition $\hbar\omega_c \ll k_BT$ is always satisfied.

From Eqs. (5.20) and (5.22), $M(B, T)$ of undoped graphene ($\mu = 0$) is given by

$$M = \begin{cases} -\dfrac{0.882}{\pi}\dfrac{e^{3/2}v_F}{\hbar^{1/2}}\sqrt{B} + \dfrac{2\ln(2)}{\pi}\dfrac{e}{\hbar}k_BT, \ (\hbar\omega_c \gg k_BT), \\ \\ -\dfrac{1}{6}\dfrac{e^2{v_F}^2}{\pi}\dfrac{B}{k_BT} + \mathcal{O}(B^3), \ (\hbar\omega_c \ll k_BT). \end{cases} \tag{5.23}$$

In Eq. (5.23) for $\hbar\omega_c \ll k_BT$, only odd powers of B survive because $\mathcal{B}_{\ell+1}$ is zero for even $\ell > 0$. The analytical expressions of M in Eq. (5.23) can be directly compared with the work of Li et al. [78], in which numerical calculation and experimental measurement of M of as a function B and T are fitted into a Langevin function [see Eq. (1.36)]. By setting Eqs. (5.23) and (1.37) side by side, our analytical formula reproduces experimental observation for the dependences of M on B and T, both for $\hbar\omega_c \gg k_BT$ and $\hbar\omega_c \ll k_BT$. Thus, the zeta regularization reasonably reproduces experimental results of M.

In Fig. 5.1(a), we plot $M(B, T)$ for $\hbar\omega_c \gg k_BT$ as a function of B for several values of T by the analytical expression Eq. (5.23) (symbols) and the Langevin function Eq. (1.36) (lines). We can see that Eq. (5.23) works well at temperature as high as $T = 100$ K for $B \geqslant 1$ T, but for $B < 1$ T, Eq. (5.23) overestimates the temperature dependence of M because the condition $\hbar\omega_c \gg k_BT$ is not satisfied. In Fig. 5.1(b) we show M as a function of T for several values of B. The linear dependence of M on T at strong B originates from the entropy S of electrons which occupy the zeroth LLs [see Eq. (5.20)]. In Fig. 5.1(c), we plot $M_S \equiv M + C\sqrt{B}$, with $C \equiv 0.882e^{3/2}v_F/(\pi\hbar^{1/2})$ [see Eq. (5.23)] as a function of T for several values of B. M_S is a deviation from the intrinsic diamagnetism with increasing temperature, and does not depend on B. Interestingly, the gradient of M_S on T in 5.1(c) is given by fundamental constants $[2\ln(2)/\pi]ek_B/\hbar = 9.256 \times 10^{-9}$ A/K.

In Fig. 5.2(a), we plot $M(B, T)$ for $\hbar\omega_c \ll k_BT$ as a function of B for several values of T by the analytical expression Eq. (5.23) (symbols) and the Langevin function Eq. (1.36) (lines), where the linear B dependences of M for $B \leq 0.5$ T are observed at temperature as low as $T = 200$ K, especially for weak $B \sim 0.1$ T. For stronger B, Eqs. (5.23) and (1.36) begin to show some discrepancies. In Fig. 5.2(b), M is plotted as a function of $1/T$ for several values of B. In Fig. 5.2(c), the function M/B is plotted as a function of $1/T$. Here, M is aligned into a straight line which illustrates

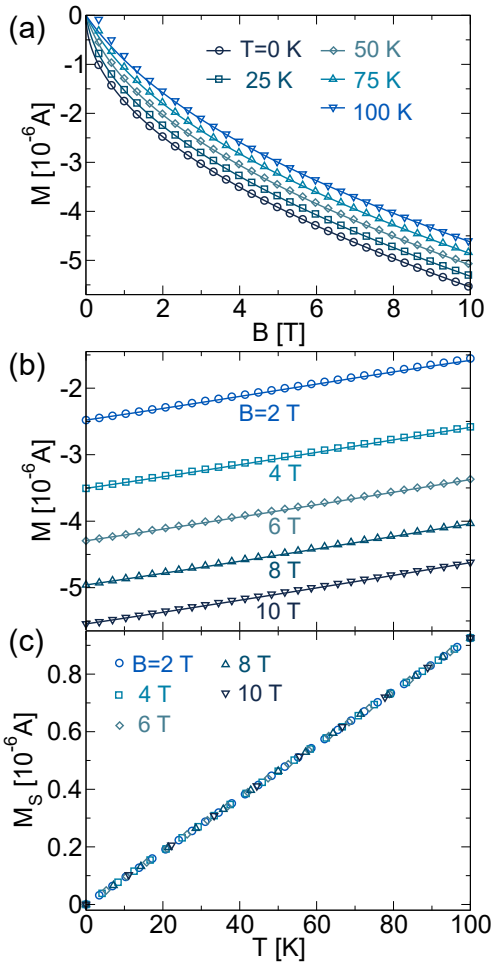

Figure 5.1 Magnetization of graphene at $\hbar\omega_c \gg k_B T$ limit as a function of magnetic field and temperature. (a) M as a function of $B = 0 - 10$ T for several values of T. (b) M and (c) M_S as a function of T ($T = 0 - 100$ K) for several values of B. The calculations from the analytical formula [Eq. (5.23)] and the Langevin function [Eq. (1.36)] are depicted by symbols and lines, respectively [101].

$M \propto -B/T$ dependence. The linear T^{-1} dependence of M at weak B originates from the thermal excitation of electrons from valence to conduction bands, because in the derivation of Eq. (5.14), we consider the entire LLs at the both bands.

In the case of doped grapphene ($\mu > 0$), M at $\hbar\omega_c \ll k_B T$ rapidly decreases with increasing μ because of the leading factor, $\mathrm{Li}_{-1}(-e^{\beta\mu})$ in Eq. (5.22). On the other hand, M for $\mu > 0$ at $T = 0$ K shows the dHvA oscillation. The dHvA oscillation of graphene and gapped graphene will be discussed together in the next Section, in order to uncover the effect of the band gap on the period and amplitude of the oscillations.

Fig. 5.1: fig/ch5/fig:GrlowT.eps

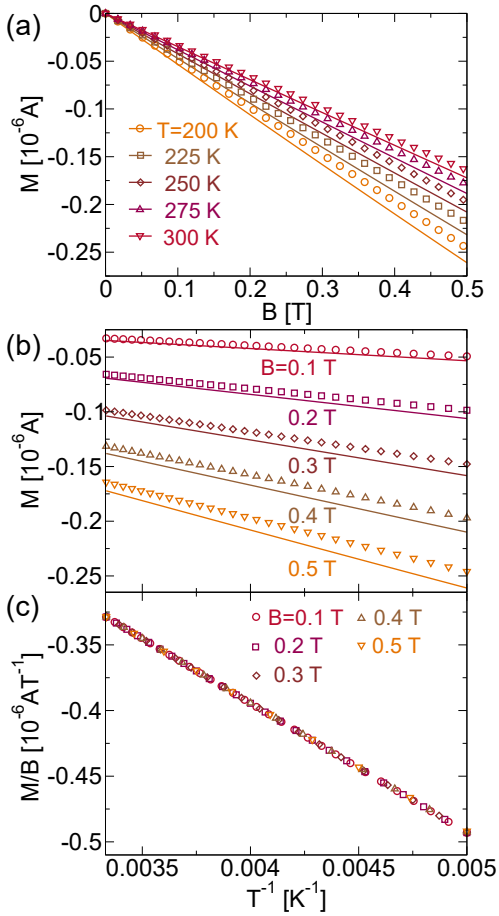

Figure 5.2 Magnetization of graphene at $\hbar\omega_c \ll k_B T$ limit as a function of magnetic field and temperature. (a) M as a function of $B = 0 - 0.5$ T for several values of T. (b) M and (c) M/B as a function $1/T$ ($T = 200 - 300$ K) for several values of B. The calculations from the analytical formula [Eq. (5.23)] and the Langevin function [Eq. (1.36)] are depicted by symbols and lines, respectively [101].

The explicit magnetization for both graphene ($\Delta = 0$) and gapped graphene ($\Delta \neq 0$) is given by Eq. (5.26) in Section 5.4.

5.4 Magnetization and dHvA oscillation of graphene and gapped graphene [$T = 0$ K, any $\Delta = 0$, $\lambda = 0$, any μ]

In this section, magnetization M is obtained by applying Eq. (3.17) on Eqs. (5.2) and (5.6). First, let discuss the dependence of M on Δ for undoped ($\mu = 0$) massive Dirac fermions at $T = 0$ K. In Fig. 5.3, we plot M as a function of B for several

Fig. 5.2: fig/ch5/fig:GrhighT.eps

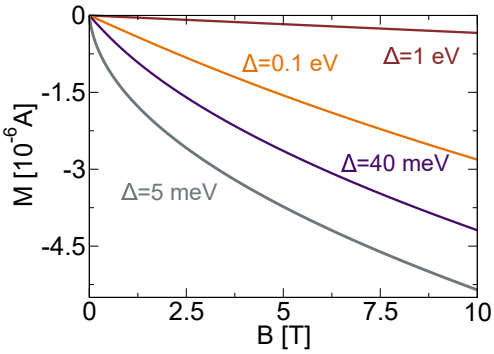

Figure 5.3 Magnetization of massive Dirac fermions (Δ = 5 meV, 40 meV, 0.1 eV and 1 eV) as a function $B = 0 - 10$ T at $T = 0$ K. The value of chemical potential is $\mu = 0$ [101].

values of Δ, where the magnetization undergoes a gradual change from $M \propto -\sqrt{B}$ to $M \propto -B$ dependences with increasing Δ for $B = 1 - 10$ T. This indicates that the anomalous orbital diamagnetism for $\Delta = 0$ disappears with opening the band-gap. The spacing of the LLs which is initially $\sqrt{|n|}$ dependence becomes constant $(\hbar\omega_c)^2/\Delta$ with increasing Δ. This process can be observed by the transition from the topological to the trivial phases of undoped silicene, in which the band-gap can be controlled by applying an external electric field [120] perpendicular to the silicene plane. In the Section 5.3, a similar transition is predicted for M of graphene with increasing temperature, for the same reason. Here, the $\sqrt{|n|}$ dependence of the LLs in the valence bands is responsible for the $M \propto -\sqrt{B}$ behaviour. When the thermal energy becomes larger than the cyclotron energy, the effect $\sqrt{|n|}$ spacing of the LLs on M becomes no longer important, and thus the Dirac system shows linear response $M \propto -B$ at a high T.

Let us discuss the dHvA oscillation at $T = 0$ K by assuming a fixed $\mu > \Delta/2$ and $\lambda = 0$ in Eqs. (5.2) and (5.6). In the bottom panel of Fig. 5.4(a), we plot Ω for $\mu = 100$ meV and $\Delta = 0$ meV as a function of inverse magnetic field $1/B$. At several values of $1/B$ (labelled as $1/B_\nu$, $\nu = 1, 2, ...$), we observe peaks of Ω which indicate the local maxima of potential. The peaks are separated by a period of 0.13 T^{-1}. At $1/B_\nu$, the ν-th LLs at the K and K' valleys exactly match the chemical potential μ, and therefore we get

$$\nu = \frac{\mu^2 - (\Delta/2)^2}{2\hbar {v_F}^2 e B_\nu} = \frac{\hbar A_F}{2\pi e B_\nu}, \tag{5.24}$$

where $A_F = \pi {k_F}^2 = \pi[\mu^2 - (\Delta/2)^2]/(\hbar v_F)^2$ is the area of the Fermi surface of the Dirac system. The rightmost side of Eq. (5.24) is the Onsager relation [86] for the massive Dirac fermions. The period of the dHvA oscillation is given as follows

$$P = \frac{1}{B_\nu} - \frac{1}{B_{\nu-1}} = \frac{2\hbar {v_F}^2 e}{\mu^2 - (\Delta/2)^2}, \tag{5.25}$$

Fig. 5.3: fig/ch5/fig:DiracT0.eps

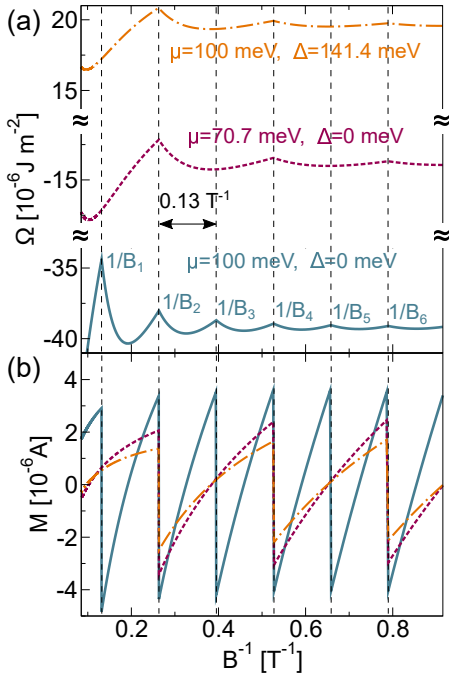

Figure 5.4 (Color online) The oscillations of (a) thermodynamic potential and (b) magnetization for $\mu = 100$ meV, $\Delta = 0$ meV (solid lines), $\mu = 70.7$ meV, $\Delta = 0$ meV (dashed lines), and $\mu = 100$ meV, $\Delta = 141.4$ meV (dash-dotted lines) at $T = 0$ K [101].

which is similar to ref. [102]. In the middle and upper panels of Fig. 5.4(a), we plot Ω by adopting (1) $\mu = 100/\sqrt{2}$ meV ≈ 70.7 meV, $\Delta = 0$ meV and (2) $\mu = 100$ meV, $\Delta = 100\sqrt{2}$ meV ≈ 141.4 meV, respectively. In the both cases, the periods of the oscillation are doubled, which is consistent with Eq. (5.25). Thus, the period of the dHvA can be used to extract the value μ relative to the band gap Δ. This method is originally proposed by Sharapov et al. [102] to detect the opening of band-gap in graphene with keeping μ constant. Experimentally, the band-gap opening was observed [121] in epitaxially grown graphene on SiC substrate, where $\Delta \approx 0.26$ eV is observed by breaking of sublattice symmetry due to graphene-substrate interaction [121].

In Fig. 5.4(b) we plot M for several values of (μ, Δ) provided in Fig. 5.4(a), where the oscillations exhibits a sawtooth-like feature, which is a characteristic of 2D materials [80, 122, 123] We show that the sawtooth behaviour of M can be explained from the zeta functions in Eqs. (5.2) and (5.6). By using $\partial\zeta(p,q)/\partial q = -p\zeta(p+1,q)$,

Fig. 5.4: fig/ch5/fig:dHvADirac.eps

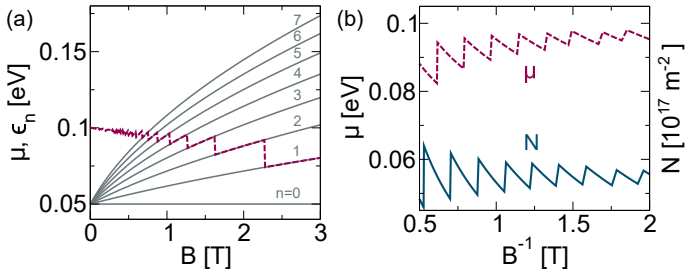

Figure 5.5 Oscillations of (a) $\mu(B)$ superimposed on the $n = 0 - 7$ LLs at the K' valley and (b) $\mu(B)$ and $N(B)$ as a function of B^{-1}. In (a) and (b), we take $\epsilon_F = 100$ meV and $T = 0$ K [101].

M is analytically given by

$$M = \frac{4e}{h}\left[\frac{3}{2}\hbar\omega_c\zeta\Big(-\frac{1}{2},\phi\Big) + \mu\Big(\nu+\frac{1}{2}\Big) - \mu\widetilde{\nu}\sum_{\nu}\delta(\widetilde{\nu}-\nu) - \frac{1}{2}\hbar\omega_c\zeta\Big(\frac{1}{2},\phi\Big)\left\{\Gamma^2 + \widetilde{\nu}\sum_{\nu}\delta(\widetilde{\nu}-\nu)\right\}\right], \tag{5.26}$$

where we define $\phi \equiv \Gamma^2 + \nu + 1$. Thus, the sawtooth-like oscillation in M originates from the delta function at $\tilde{\nu} = \nu$ in Eq. (5.26), which is the result of differentiation of the floor function in the expression of ν $[\partial\lfloor x\rfloor/\partial x = \sum_{n\in\mathbb{Z}}\delta(x-n)]$. Physically, the delta function indicates the occupations of electrons at the discrete LLs. With the increase of temperature, the presence of impurity scattering, electron-electron and electron-phonon interactions [124, 125, 126], the LLs become broad, therefore the delta function should be replaced by Gaussian or Lorentzian functions to account the broadening by the interactions. As a result, the oscillation of magnetization becomes less sharp. The effects of the broadening on the dHvA oscillation can be incorporated by the convolution of the thermodynamic potential at $T = 0$ K with the distribution functions for temperature and impurities [127, 128].

We observe that for $\Delta = 0$ (doped graphene) [solid and dashed lines in Fig. 5.4(b)], the smaller μ not only yields a decreasing frequency but also a weaker amplitude in the oscillation. When we consider the cases of $\sqrt{\mu^2 - (\Delta/2)^2} = 70.7$ meV (dashed and dash-dotted lines), the oscillation with $\Delta \neq 0$ (dash-dotted line) produces a smaller amplitude than the case with $\Delta = 0$ (dashed line). The effect of Δ on the magnitude of the oscillation appears in the last term of Eq. (5.26) [$\Gamma = \Delta/(2\hbar\omega)$]. Therefore the opening of the band-gap decreases not only the frequency, but also the amplitude of the dHvA oscillation, as the functions $\zeta(-1/2,\phi)$ and $\zeta(1/2,\phi)$ possess the same signs for a given ϕ (see Appendix A.3). It is noted that for a strong magnetic field ($\hbar\omega_c > \sqrt{\mu^2 - (\Delta/2)^2}$, hence $\nu = 0$), Eq. (5.26) will reduce to $M \propto -\sqrt{B}$ because of the linear dependence on ω_c, which will be retained with small increase of temperature ($\hbar\omega_c \gg k_BT$).

We also discuss the possible behaviour of dHvA effect for a fixed electron density N, which is originated from the oscillation of the chemical potential as a function

Fig. 5.5: fig/ch5/fig:muNdHvA2.eps

of B, $\mu(B)$ for an isolated sample from the particle source. N is given by the spin and Landau degeneracies multiplied by the number of occupied LLs at the conduction bands, as follows:

$$N = g_s \frac{eB}{h}(2\nu + 1), \tag{5.27}$$

where the factor 2 for 2ν comes from the valley degeneracy, and the term 1 inside the bracket represents the zeroth LL at the K' valley. From Eq. (5.27), ν for a fixed N is given by

$$\nu = \left\lfloor \frac{1}{2}\Big(\frac{Nh}{g_s eB} - 1\Big) \right\rfloor, \tag{5.28}$$

In Eq. (5.28), N can be obtained from the Fermi energy at zero magnetic field $\epsilon_F = \sqrt{(\hbar v_F k_F)^2 + (\Delta/2)^2}$, that is,

$$N = 2g_s \frac{\pi {k_F}^2}{(2\pi)^2} = \frac{g_s}{2\pi} \frac{{\epsilon_F}^2 - \Delta^2/4}{(\hbar v_F)^2}. \tag{5.29}$$

For a given B, the chemical potential is equal to the highest LL $\epsilon_\nu(B)$, and thus we get $\mu(B) = \epsilon_\nu(B) = \sqrt{2\hbar {v_F}^2 eB\nu + \Delta^2/4}$.

In Fig. 5.5(a), we plot $\mu(B)$ (red-dashed line) for $\epsilon_F = 100$ meV at $B = 0$ T, superimposed on the $n = 0 - 7$ LLs (grey-solid lines). We see that $\mu(B)$ falls to the lower LLs one by one with increasing B. It is noted that we need to take a special care for the occupancy in the $n = 0$ LL for a large B [out of range of B in Fig. 5.5(a)] since there is only one zeroth LL that electrons occupy in the conduction bands, which we do not discuss here. At B_ν, μ undergoes transition from ϵ_ν to $\epsilon_{\nu-1}$, the corresponding ν is as follows:

$$\nu = \frac{{\epsilon_F}^2 - \Delta^2/4}{2\hbar {v_F}^2 eB_\nu} - \frac{1}{2}. \tag{5.30}$$

From Eq. (5.29) and (5.30), the period of oscillation is given by

$$P = \frac{2\hbar {v_F}^2 e}{{\epsilon_F}^2 - \Delta^2/4}, \tag{5.31}$$

which is identical to Eq. (5.25). In Fig. 5.5(b), we compare the oscillation for the cases of $\mu(B)$, with keeping N constant (red-dashed line) and $N(B)$, with keeping μ constant (blue-solid line). For μ constant, $N(B)$ is given by

$$N(B) = g_s \frac{eB}{h}\left(2\Big\lfloor \frac{\mu^2 - \Delta^2/4}{2\hbar {v_F}^2 eB} \Big\rfloor + 1\right). \tag{5.32}$$

Therefore, we conclude that the dHvA effect with a fixed N has the same period to that of the oscillation with a fixed μ, but differs in phase.

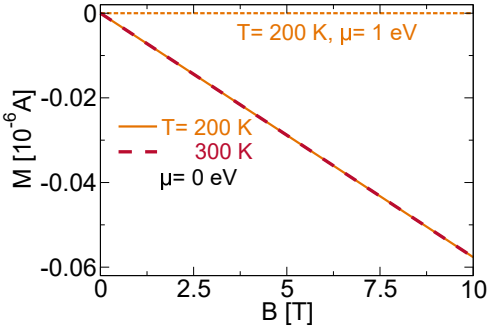

Figure 5.6 Magnetization of undoped and doped ($\mu = 1$ eV) MoS_2 as a function $B = 0-10$ T at $T = 200$ and 300 K [101].

5.5 Magnetization of monolayer TMDs [$(k_BT \sim \hbar\omega_c) \ll \Delta$, $\lambda \neq 0$, any μ]

In a magnetic field up to $\sim$ 10 T, the LL of a monolayer TMD in Eq. (3.12) are approximated by $\epsilon_n^\xi \approx \xi\lambda - \Delta/2 - (\hbar\omega_c)^2|n|/\Delta_\xi$ and $\epsilon_n^\xi \approx \Delta/2 + (\hbar\omega_c)^2|n|/\Delta_\xi$ for $\mathrm{sgn}_\tau(n) = -1$ and $\mathrm{sgn}_\tau(n) = +1$, respectively. Hence, the LLs separation is inversely proportional to the band gap, i.e. $(\hbar\omega_c)^2/\Delta_\xi$. This approximation is also valid for heavy Dirac fermions such as hexagonal boron-nitride where $\Delta \approx 6$ eV [129, 130, 131] by setting $\lambda = 0$. Since the separation of the LLs is small compared with k_BT, thermal excitation can induce indefinite occupation of the LLs at the conduction bands, and therefore $\Omega = \Omega_- + \Omega_+$. First, let us derive Ω_- as follows:

$$\begin{aligned}
\Omega_- &= -\frac{1}{\beta}\frac{eB}{h}\sum_{\xi=\pm}\left[\sum_{n=0}^{\infty}+\sum_{n=1}^{\infty}\right]\ln[1+\exp\{-\beta(\epsilon_{-n}^\xi-\mu)\}] \\
&= -\frac{1}{\beta}\frac{eB}{h}\sum_{\xi=\pm}\ln[1+e^{\beta(\mu-\xi\lambda+\Delta/2)}] \\
&\quad -\frac{2}{\beta}\frac{eB}{h}\sum_{\xi=\pm}\sum_{n=1}^{\infty}\ln[1+e^{\beta\{\mu-\xi\lambda+\Delta/2+(\hbar\omega_c)^2 n/\Delta_\xi\}}] \\
&\equiv \Omega'_- + \Omega''_-.
\end{aligned} \tag{5.33}$$

In the last line of Eq. (5.33), we define Ω'_- and Ω''_- as thermodynamic potentials for the zeroth LL (at the K valley) and the LLs $n \leqslant -1$, respectively. By expanding the

Fig. 5.6: fig/ch5/fig:MoS2Th.eps

logarithmic and the exponential functions in the expression of Ω''_-, we get

$$\begin{aligned}\Omega''_- &= \frac{2}{\beta}\frac{eB}{h}\sum_{\xi=\pm}\sum_{k=1}^{\infty}\frac{[-e^{(\mu-\xi\lambda+\Delta/2)}]^k}{k}\sum_{l=0}^{\infty}\Big(\frac{\beta k}{\Delta_\xi}\Big)^l\frac{(\hbar\omega_c)^{2l}}{l!}\sum_{n=1}^{\infty}n^l \\ &= \frac{2}{\beta}\frac{eB}{h}\sum_{\xi=\pm}\sum_{l=0}^{\infty}\mathrm{Li}_{1-l}[-e^{\beta(\mu-\xi\lambda+\Delta/2)}]\Big(\frac{\beta}{\Delta_\xi}\Big)^l\frac{(\hbar\omega_c)^{2l}}{l!}\zeta(-l) \\ &= \sum_{l=0}^{\infty}\Omega''_l.\end{aligned} \tag{5.34}$$

Because $\mathrm{Li}_1(z) = -\ln(1-z)$ and $\zeta(0) = -1/2$, we get $\Omega''_0 = eB/(\beta h)\sum_{\xi=\pm1}\ln[1 + e^{(\mu-\xi\lambda+\Delta/2)}] = -\Omega'_-$. As a result, only the terms for $l \geqslant 1$ survives in the final expression of Ω_- as follows:

$$\Omega_- = -\frac{2}{\beta}\frac{eB}{h}\sum_{\xi=\pm1}\sum_{l=1}^{\infty}\mathrm{Li}_{1-l}[-e^{\beta(\mu-\xi\lambda+\Delta/2)}]\Big(\frac{\beta}{\Delta_\xi}\Big)^l\frac{(\hbar\omega_c)^{2l}}{l!}\frac{\mathcal{B}_{l+1}}{l+1}. \tag{5.35}$$

Thus, the entropy of electrons at the zeroth LLs is not manifested in a linear T dependence of as in the case of graphene. Similarly, we can derive Ω_+ of a monolayer as follows:

$$\Omega_+ = -\frac{2}{\beta}\frac{eB}{h}\sum_{\xi=\pm1}\sum_{l=1}^{\infty}\mathrm{Li}_{1-l}[-e^{\beta(\mu-\Delta/2)}]\Big(\frac{-\beta}{\Delta_\xi}\Big)^l\frac{(\hbar\omega_c)^{2l}}{l!}\frac{\mathcal{B}_{l+1}}{l+1}. \tag{5.36}$$

From the leading terms in Eqs. (5.35) and (5.36) ($\ell = 1$), the total thermodynamic potential Ω and magnetization M of the monolayer TMD are given by

$$\Omega \approx \frac{e^2{v_F}^2B^2}{6\pi}\sum_{\xi=\pm}\frac{1}{\Delta_\xi}\frac{\sinh\Big[\frac{\beta\Delta_\xi}{2}\Big]}{\cosh\Big[\frac{\beta\Delta_\xi}{2}\Big]+\cosh\Big[\beta\Big(\mu-\frac{\xi\lambda}{2}\Big)\Big]}, \tag{5.37}$$

and

$$M \approx -\frac{(ev_F)^2B}{3\pi}\sum_{\xi=\pm}\frac{1}{\Delta_\xi}\frac{\sinh\Big[\frac{\beta\Delta_\xi}{2}\Big]}{\cosh\Big[\frac{\beta\Delta_\xi}{2}\Big]+\cosh\Big[\beta\Big(\mu-\frac{\xi\lambda}{2}\Big)\Big]}, \tag{5.38}$$

respectively.

In Fig. 5.6, we plot M of undoped MoS_2 as a function of B for $B = 0 - 10$ T at $T = 200$ K and 300 K, where the magnetization does not change with increasing temperature from $T = 200$ K to 300 K. Thus, even though the magnitude of magnetization in a heavy Dirac fermion decreases with the increasing band gap, the magnetization is robust for temperature. The temperature-independent behaviour originates from the energy of the zeroth LLs. In Section 5.3, we have shown that for graphene, the T-dependent is mainly contributed by entropy of the zeroth LLs for $\hbar\omega_c \gg k_BT$ and thermal excitation from valence to conduction bands for $\hbar\omega_c \ll k_BT$. In a heavy Dirac fermion, on the other hand, the energy gap is much larger than the thermal energy $\Delta \gg k_BT$, therefore electrons can not be thermally excited from the valence to

conduction bands. Furthermore, since the zeroth LL at the K valley is fully occupied, the zeroth LL does not contribute to the entropy as in the case of undoped graphene. As a result, magnetization of the heavy Dirac fermion is temperature-independent. In fact, by comparing Eqs. (5.38) and (5.5), we infer that the magnetizations of the undoped ($\mu = 0$), heavy Dirac fermions at $T = 0$ K and $T \sim \hbar\omega_c/k_B$ are almost equal, provided that $\Delta/2 \gg k_B T$. We also plot M for a doped case ($\mu = 1$ eV) at $T = 200$ K where the magnetization becomes zero, which demonstrates the effect of pseudospin paramagnetism [33, 34], as discussed by Koshino and Ando with the Euler-Maclaurin formula.

5.6 Justification of zeta function regularization

In this section, we briefly discuss the physical meaning of zeta function regularization in the calculation of Ω. This discussion is useful to justify the use of zeta function when calculate infinite summations of the LLs.

Let us consider the calculation of M of undoped graphene at $T = 0$ K. When we apply an external magnetic field, the states of electron at the K and K' coalesce to the LLs (see Fig. 1.7 which illustrates this process). Here, we introduce an energy cut-off of the LL in the valence bands ϵ_{-m}. The energy of graphene without B, $\Omega^{(0)}(m)$ is given by the integration along the Dirac cone as follows:

$$\Omega^{(0)} = 4\int_{\epsilon_{-m-1/2}}^{0} d\epsilon\ |\epsilon| g(\epsilon) = -\frac{2}{3}\frac{2^{3/2}}{\pi}\frac{e^{3/2}v_F}{\hbar^{1/2}}B^{3/2}\Big(m+\frac{1}{2}\Big)^{3/2}, \tag{5.39}$$

where $g(\epsilon)$ is the density of states of electrons in graphene (per unit area) [see Eq. (1.27)], and the factor 4 represents the spin and valley degeneracies. The binomial expansion on $(m+1/2)^{3/2}$ is given by

$$\Big(m+\frac{1}{2}\Big)^{3/2} = m^{3/2} + \frac{3}{4}m^{1/2} + \frac{3}{32}m^{-1/2} - \frac{1}{128}m^{-3/2} + \mathcal{O}(m^{-5/2}). \tag{5.40}$$

Thus, Eq. (5.39) can be expressed in term of the power series of m as follows:

$$\Omega^{(0)}(m) \approx -\frac{2^{3/2}}{\pi}\frac{e^{3/2}v_F}{\hbar^{1/2}}B^{3/2}\left[\frac{2}{3}m^{3/2} + \frac{1}{2}m^{1/2} + \frac{1}{16}m^{-1/2} - \frac{1}{192}m^{-3/2}\right] \tag{5.41}$$

On the other hand, the energy of graphene with B is given by

$$\Omega_-(m) = 4\frac{eB}{h}\sum_{n=-m}^{-1}\epsilon_n = -\frac{2^{3/2}}{\pi}\frac{e^{3/2}v_F}{\hbar^{1/2}}B^{3/2}\sum_{n=1}^{m}\sqrt{n}. \tag{5.42}$$

By using Eq. (5.7), the summation on n on the right-most side of Eq. (5.42) is given by the difference of the Riemann and Hurwitz zeta functions as follows:

$$\sum_{n=1}^{m}\sqrt{n} = \zeta\Big(-\frac{1}{2}\Big) - \zeta\Big(-\frac{1}{2}, m+1\Big). \tag{5.43}$$

For $m \gg 1$, $\zeta(-1/2, m+1)$ is approximately given by [see Eqs. (5.3) and (5.10)]

$$\zeta\Big(-\frac{1}{2}, m+1\Big) \approx -\frac{2}{3}m^{3/2} - \frac{1}{2}m^{1/2} - \frac{1}{24}m^{-1/2}. \tag{5.44}$$

By substituting Eqs. (5.43) and (5.44) to Eq. (5.42), we get

$$\Omega_-(m) \approx -\frac{2^{3/2}}{\pi}\frac{e^{3/2}v_F}{\hbar^{1/2}}B^{3/2}\left[\zeta\Big(-\frac{1}{2}\Big)+\frac{2}{3}m^{3/2}+\frac{1}{2}m^{1/2}+\frac{1}{24}m^{-1/2}\right]. \tag{5.45}$$

When we subtract Eq. (5.41) from Eq. (5.45) to calculate the change of energy after and before we apply the magnetic field, the terms $\propto m^{3/2}$ and $m^{1/2}$ are cancelled. The remaining terms are given by

$$\Delta\Omega(m) \equiv \Omega_- - \Omega^{(0)} = -\frac{2^{3/2}}{\pi}\frac{e^{3/2}v_F}{\hbar^{1/2}}B^{3/2}\left[\zeta\Big(-\frac{1}{2}\Big)-\frac{1}{48}m^{-1/2}+\frac{1}{192}m^{-3/2}\right]. \tag{5.46}$$

It is observed that as $m \to \infty$, the terms which depend on m vanish. Therefore, we conclude that $\Delta\Omega(\infty) \propto -B^{3/2}\zeta(-1/2)$ is a quantity that remains when we take the difference of two diverging quantities, $\Omega_-(\infty)$ and $\Omega^{(0)}(\infty)$. The calculation of M by using Eq. (5.46) yields $M \propto -\sqrt{B}$ for $T = 0$ K [see Eq. (5.23)].

5.7 Impurity effect on susceptibilities of graphene and monolayer TMDs

Finally, by using Eqs. (3.18) and (3.19), let us analyse the effect of impurity scattering on the orbital susceptibility of the Dirac fermions. In the case of graphene, we approximate the function $\mathrm{Li}_{-1}(-e^{\beta\varepsilon}) \propto \mathrm{sech}^2(\beta\varepsilon/2)$ in Eq. (5.22) by a Gaussian function as follows. For given secant-hyperbolic and the Gaussian distributions, $F(\varepsilon) \equiv \mathrm{sech}(\varepsilon/W)$ and $G(\varepsilon) \equiv \exp[-\varepsilon^2/(2\sigma^2)]$, respectively, the half-width of the distributions are given by $\mathrm{HW}_F = \ln(2+\sqrt{3})W$ and $\mathrm{HW}_G = \sqrt{2\ln(2)}\sigma$, where σ is the standard deviation of the Gaussian function. By solving $\mathrm{HW}_F = \mathrm{HW}_G$ and by setting $W = 2/\beta$, the Gaussian approximation for the function $f(\varepsilon) \equiv \mathrm{sech}^2(\beta\varepsilon/2)$ is given by $g(\varepsilon) \equiv \exp[-(C\beta\varepsilon)^2]$, where $C = \sqrt{\ln 2}/[\sqrt{2}\ln(2+\sqrt{3})] \approx 0.447$. In Fig. 5.7, we compare $f(\varepsilon)$ and $g(\varepsilon)$ (thin-solid lines) for several values of temperature. The distribution $g(\varepsilon)$ has a smaller tail compared with $f(\varepsilon)$. Therefore, Eq. (3.18) is approximated by convolution of the Gaussian with the Lorentzian functions, which is known as the Voigt profile. The solution of the Voigt profile is given by the real part of the Faddeeva function $w(z)$ as follows [74]:

$$V(x,y,\sigma) \equiv \frac{y}{\pi}\int_{-\infty}^{\infty} dt \frac{\exp[-t^2/(2\sigma^2)]}{(t-x)^2+y^2} = \mathrm{Re}[w(z)], \tag{5.47}$$

where $z \equiv (x+iy)/(\sqrt{2}\sigma)$, and $w(z)$ is the Faddeeva function defined by

$$w(z) \equiv e^{-z^2}\left(1+\frac{2i}{\sqrt{\pi}}\int_0^z dt e^{t^2}\right). \tag{5.48}$$

Thus, in the presence of impurity, the orbital susceptibility of graphene is approximately given by

$$\chi(\mu,\gamma) \approx -\frac{e^2{v_F}^2}{6\pi k_B T}\mathrm{Re}[w(z')], \tag{5.49}$$

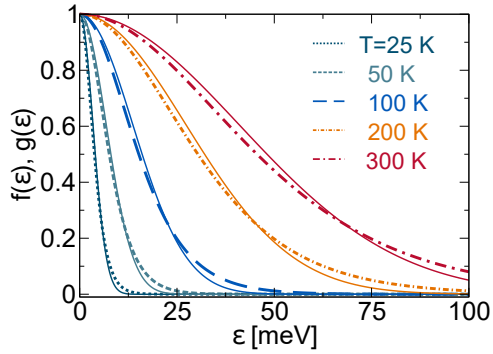

Figure 5.7 Comparison between the functions $f(\varepsilon)$ and $g(\varepsilon)$ (thin-solid lines) for T = 25, 50, 100, 200 and 300 K [101].

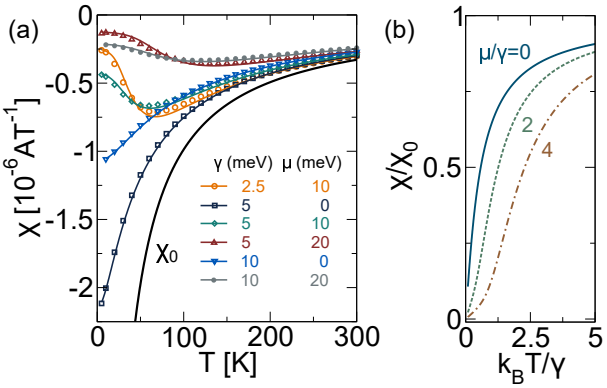

Figure 5.8 Susceptibility of graphene with impurity as a function of temperature. (a) The calculations of χ as a function of $T = 0-300$ K for several values of γ and μ with the Faddeeva function (solid lines) and numerical calculations (symbols). (b) The scaled susceptibility χ/χ_0 as a function of k_BT/γ for $\mu/\gamma = 0,\ 2$, and 4 with the Faddeeva function [101].

where we define $z' \equiv C\beta(\mu + i\gamma)$.

In Fig. 5.8(a), we plot χ of graphene as a function of T for several values of γ and μ, by using Eq. (5.49) (lines), as well as by numerical calculation of the convolution by using the $\mathrm{sech}^2(\beta\varepsilon/2)$ function (symbols). We can see that the approximation with the Fadddeeva function is in a good agreement with the numerical calculation. For comparison, we show the susceptibility of undoped graphene without impurity χ_0 by putting $\mu = 0$ in Eq. (1.32) $[\chi_0 = -(ev_F)^2/(6\pi k_B T)]$, which is inversely proportional to T. From Fig. 5.8(a), χ for non-zero γ stays at finite value $T \to 0$ K, which shows that the anomalous diamagnetism in graphene disappears by introducing impurity. In the cases of $\mu \neq 0$, we observe minimum values of χ at finite temperatures. For $\gamma = 5$ meV, the minimum value becomes smaller and shift to the higher temperature

Fig. 5.7: fig/ch5/fig:Gaussian.eps
Fig. 5.8: fig/ch5/fig:faddevaT2.eps

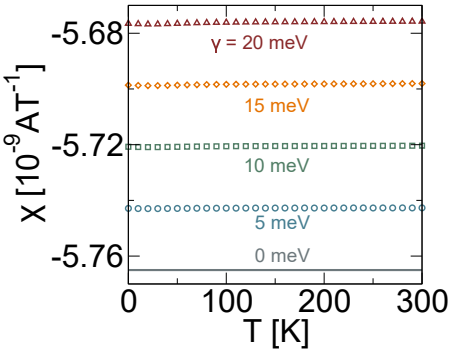

Figure 5.9 (Color online) The susceptibility of undoped MoS_2 with impurity as a function of temperature $T = 0 - 300$ K for $\gamma = 0,\ 5,\ 10$, and 20 meV [101].

as we increase μ from 10 meV to 20 meV. The present method reproduces the calculation by Nakamura and Hirasawa [104, 105], where the χ of graphene with impurity is approximated by the Sommerfeld expansion, and also shows the minimum values as a function of T. It is noted that the origin of discrepancies between the numerical calculation and the Faddeeva approximation in the calculation of $\chi(\mu, \gamma)$ is the approximation of the function $f(\varepsilon) = \mathrm{sech}^2(\beta\varepsilon/2)$ and $g(\varepsilon) \equiv \exp[-(C\beta\varepsilon)^2]$.

In Fig. 5.8(b), we plot χ/χ_0 as a function of $k_B T/\gamma$. For a given ratio μ/γ, the curves shown in Fig. 5.8(a) follow the scaling law shown in Fig. 5.8(b). Hence, the advantage of using the Faddeeva function is that the susceptibility of graphene in the presence of the impurity scattering is approximately scaled by the function $\mathrm{Re}[w(z')]$.

In Fig. 5.9, we numerically calculate the χ of undoped MoS_2 as a function of T for several values of γ. Here, χ does not change with increasing T. As we increase γ, the magnitude of χ decreases with the same rate, which means that for a given temperature, the magnitude of susceptibility decreases linearly as a function of γ.

Fig. 5.9: fig/ch5/fig:MoS2I.eps

Chapter 6

Conclusions

Faraday and Kerr rotations in the Haldane model

For the first subject, we investigate the Faraday and the Kerr rotations in the Haldane model without an external magnetic field. Here, the Faraday and the Kerr rotations originate from intrinsic Hall conductivity which is generated by broken time-reversal symmetry in the Haldane model. The Faraday and the Kerr rotations show singularities when the photon energy matches the energy band gap. Further, we show that the maximum Kerr rotations occurs at the Brewster angle. Nevertheless, this phenomenon is difficult to observe due to small reflection probability. Our treatment on the Faraday and the Kerr rotations is relevant to determine the topological phases in 2D materials. Moreover, our analytical formulae for optical conductivities can be applied to explain optical absorption of circularly-polarized lights in silicene and monolayer transition-metal dichalcogenides.

Magnetzation and de Haas-van Alphen effect in 2D materials

For the second subject, we derive analytical expressions for magnetizations of 2D Dirac fermions by using the zeta function regularization. Our formula reproduces the empirical fitting for the magnetization of undoped graphene in strong field/low temperature and weak field/high temperature limits. In the case of heavy Dirac fermions, we show that the magnetization is robust with respect to temperature and impurity scattering. Further, we demonstrate that band-gap opening in the 2D materials can be detected from decreasing amplitude of the de Haas-van Alphen (dHvA) effect, and the occupancy of electrons at the zeroth Landau level affects the phase of the dHvA oscillations. Our formulas reproduce experimental results without fitting procedure. Thus, the method of zeta function regularization is justified in the present problem.

Appendix A

Analytic continuation of zeta functions

In this appendix, we prove several formulas of the Riemann and Hurwitz zeta functions $\zeta(s)$ and $\zeta(s,a)$, which are relevant for the regularization methods in Chapter 5.

A.1 Riemann functional equation

The Riemann zeta function $\zeta(s)$, $s \in \mathbb{C}$ is defined by

$$\zeta(s) \equiv \sum_{k=1}^{\infty} \frac{1}{k^s}. \tag{A.1}$$

Eq. (A.1) converges for $\mathrm{Re}(s) > 1$. For $\mathrm{Re}(s) < 1$, the convergence of the zeta function can be obtained by the method of analytical continuation. In this section, we will derive the Riemann functional equation, which shows the convergence of $\zeta(s)$ for $\mathrm{Re}(s) < 1$.

First, we show the relation between the zeta function and gamma function $\Gamma(s)$, which is defined as follows:

$$\Gamma(s) \equiv \int_0^{\infty} dx\ x^{s-1}e^{-x}. \tag{A.2}$$

By transforming the variable x in Eq. (A.2) to $k^2\pi x$, $x \to k^2\pi x$, the product of $\zeta(s)$ and $\Gamma(s)$ is given by

$$\frac{\zeta(s)\Gamma(s/2)}{\pi^{s/2}} = \int_0^{\infty} dx\ x^{\frac{s}{2}-1} \sum_{k=1}^{\infty} e^{-k^2\pi x} \equiv \int_0^{\infty} dx\ x^{\frac{s}{2}-1}\psi(x), \tag{A.3}$$

where $\psi(x)$ is known as the *Jacobi function*. To solve Eq. (A.3), let us consider a Fourier transform of a Gaussian function $e^{-\alpha^2 t^2}$ as follows:

$$\mathcal{F}[e^{-\alpha^2 t^2}](u) \equiv \int_{-\infty}^{\infty} dt\ e^{-\alpha^2 t^2} e^{-2\pi i u t} = \gamma \int_{-\infty}^{\infty} dt e^{-(\alpha t+\beta)^2}. \tag{A.4}$$

By completing the square inside the exponential function in the right-most side of Eq. (A.4), we find that $\beta = i\pi u/\alpha$ and $\gamma = e^{-\pi^2 u^2/\alpha^2}$. Therefore,

$$\mathcal{F}[e^{-\alpha^2 t^2}](u) = e^{-\frac{\pi^2 u^2}{\alpha^2}} \int_{-\infty}^{\infty} dt\ e^{-(\alpha t + i\pi u/\alpha)^2} = \frac{\sqrt{\pi}}{\alpha} e^{-\frac{\pi^2 u^2}{\alpha^2}}. \tag{A.5}$$

By choosing $\alpha = \sqrt{\pi x}$, we obtain a discrete Fourier transform as follows:

$$\sum_{k=-\infty}^{\infty} e^{-k^2\pi x} e^{-2\pi i k\ell} = \frac{1}{\sqrt{x}} e^{-\frac{\pi\ell^2}{x}}, \tag{A.6}$$

which gives

$$\sum_{\ell=-\infty}^{\infty} e^{-\ell^2\pi x} = \frac{1}{\sqrt{x}} \sum_{\ell=-\infty}^{\infty} e^{-\frac{\pi\ell^2}{x}}, \tag{A.7}$$

or equivalently

$$1 + 2\psi(x) = \frac{1}{\sqrt{x}} \left[1 + 2\psi\Big(\frac{1}{x}\Big) \right]. \tag{A.8}$$

Here, we used the identity

$$\sum_{\ell=-\infty}^{\infty} e^{-2\pi i k\ell} = \delta_{k,\ell} \tag{A.9}$$

to derive Eq. (A.7), where $\delta_{k,\ell}$ is the Kronecker delta. By using Eq. (A.8), Eq. (A.3) can be expressed by

$$\begin{aligned} \frac{\zeta(s)\Gamma(s/2)}{\pi^{s/2}} &= \int_0^1 dx\ x^{\frac{s}{2}-1}\psi(x) + \int_1^\infty dx\ x^{\frac{s}{2}-1}\psi(x) \\ &= \int_0^1 dx\ x^{\frac{s}{2}-1} \left[\frac{1}{2\sqrt{x}} + \frac{1}{\sqrt{x}}\psi\Big(\frac{1}{x}\Big) - \frac{1}{2} \right] + \int_1^\infty dx\ x^{\frac{s}{2}-1}\psi(x) \\ &= \frac{1}{s-1} - \frac{1}{s} + \int_0^1 dx\ x^{\frac{s}{2}-\frac{3}{2}}\psi\Big(\frac{1}{x}\Big) + \int_1^\infty dx\ x^{\frac{s}{2}-1}\psi(x). \end{aligned} \tag{A.10}$$

To simplify the calculation, let us transform the variable $x \to 1/x$ for the first integration in the right-hand side of Eq. (A.10) as follows:

$$\int_0^1 dx\ x^{\frac{s}{2}-\frac{3}{2}}\psi\Big(\frac{1}{x}\Big) = \int_1^\infty dx\ x^{-\frac{s}{2}-\frac{1}{2}}\psi(x). \tag{A.11}$$

By using the identity in Eq. (A.11), Eq. (A.10) reduces to

$$\frac{\zeta(s)\Gamma(s/2)}{\pi^{s/2}} = \frac{1}{s(s-1)} + \int_1^\infty dx \left[x^{-\frac{s}{2}-\frac{1}{2}} + x^{\frac{s}{2}-1} \right] \psi(x). \tag{A.12}$$

It is noted that the right-hand side of Eq. (A.12) remains the same when we change s to $1-s$. Furthermore, the right-hand side of Eq. (A.12) converges for any $s \neq 1$ because of $\psi(x)$, which rapidly decays with increasing x for $x > 0$. Therefore, we obtain a remarkable formula which was first derived by Riemann in 1859, as follows:

$$\pi^{-\frac{s}{2}}\Gamma\Big(\frac{s}{2}\Big)\zeta(s) = \pi^{-\frac{1}{2}+\frac{s}{2}}\Gamma\Big(\frac{1-s}{2}\Big)\zeta(1-s). \tag{A.13}$$

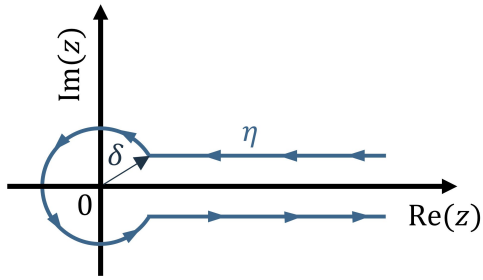

Figure A.1 The Hankel contour η.

Eq. (A.13) is known as the *Riemann functional equation*. It is useful to demonstrate the convergence of $\zeta(s)$ for $\mathrm{Re}(s) < 0$. For example, by taking $s = -1/2$ and using the identity $\Gamma(p+1) = p\Gamma(p)$, we obtain

$$\zeta(-1/2) = -\frac{1}{4\pi}\zeta(3/2), \tag{A.14}$$

where $\zeta(3/2) \approx 2.6124$. Thus, the infinite summation $\sum_{k=1}^{\infty}\sqrt{k}$ yields approximately -0.208 with the zeta function regularization.

A.2 Hurwitz zeta function and Bernoulli polynomials

In this subsection, we will derive another method to prove the convergence of $\zeta(s)$ for $\mathrm{Re}(s) < 0$, especially when $\mathrm{Re}(s)$ is an integer. We begin with the definition of the Hurwitz (or generalized) zeta function $\zeta(s,a)$ as follows:

$$\zeta(s,a) = \sum_{k=0}^{\infty}\frac{1}{(k+a)^s}, \tag{A.15}$$

for $a \neq 0,\ -1,\ -2, \ldots$. Thus, by choosing $a = 1$, Eq. (A.15) reduces to Eq. (A.1). In this section, by using the method of analytical continuation, we will derive the relation between the Hurwitz zeta function and the bernoulli polynomial $\mathcal{B}_p(x)$.

The Hurwitz zeta function is related to the gamma function by

$$\zeta(s,a)\Gamma(s) = \int_0^{\infty} dx\ x^{s-1}\frac{e^{(1-a)x}}{e^x - 1}. \tag{A.16}$$

Now, let us consider an integral $I(s,a)$ which is calculated by the *Hankel contour* η follows:

$$I(s,a) = \int_{\eta}\frac{dz}{z}(-1)^s z^s\frac{e^{(1-a)z}}{e^z - 1}. \tag{A.17}$$

Fig. A.1: fig/app/fig:hankel.eps

η extends from $(+\infty, \delta)$, anti-clockwise around a circle of radius $\delta \to 0$ at the origin, and back to $(\delta, +\infty)$, as illustrated by Fig. A.1. Therefore, Eq. (A.17) becomes

$$I(s,a) = \int_{\infty}^{\delta} \frac{dz}{z} e^{-is\pi} z^s \frac{e^{(1-a)z}}{e^z - 1} + \oint_{z=|\delta|} \frac{dz}{z} (-z)^s \frac{e^{(1-a)z}}{e^z - 1} + \int_{\delta}^{\infty} \frac{dz}{z} e^{+is\pi} z^s \frac{e^{(1-a)z}}{e^z - 1}. \tag{A.18}$$

In Eq. (A.18), we used $(-1)^s = e^{+is\pi}$ and $(-1)^s = e^{-is\pi}$ for the paths $(+\infty, \delta)$ and $(\delta, +\infty)$, respectively. Thus, the integrations along positive real axis do not cancel each other. Let us first calculate the anticlockwise integral around the origin. By using $z = \delta e^{i\theta}$, we get $dz = i\delta e^{i\theta} d\theta$, $e^z \approx 1 + \delta e^{i\theta}$ and

$$\oint_{z=|\delta|} \frac{dz}{z} (-z)^s \frac{e^{(1-a)z}}{e^z - 1} = i \int_0^{2\pi} d\theta \; (-1)^s \delta^{s-1} e^{i\theta(s-1)} [1 + (1-a)\delta e^{i\theta}] = 0, \tag{A.19}$$

for $s \neq 1$. Therefore, Eq. (A.18) becomes

$$I(s,a) = 2i \sin(s\pi) \zeta(s,a) \Gamma(s). \tag{A.20}$$

By using the reflection formula of gamma function

$$\Gamma(s)\Gamma(1-s) = \frac{\pi}{\sin(s\pi)}, \tag{A.21}$$

and by changing $s \to -s$, we get

$$\zeta(-s,a) = \frac{s!}{2\pi i} I(-s,a). \tag{A.22}$$

Now, let us return to Eq. (A.17) in order to find the relation between $\zeta(-s,a)$ and the Bernoulli polynomials. By changing $z \to -z$, $I(-s,a)$ is by

$$I(-s,a) = \int_{\eta} \frac{dz}{z^{s+1}} \frac{e^{az}}{1 - e^z}. \tag{A.23}$$

The Bernoulli polynomial $\mathcal{B}_\ell(x)$ can be defined by using a generation function as follows:

$$\frac{z e^{xz}}{e^z - 1} = \sum_{\ell=0}^{\infty} \mathcal{B}_\ell(x) \frac{z^\ell}{\ell!}. \tag{A.24}$$

The Bernoulli polynomials for $\ell = 0 - 4$ are given as follows:

$$\begin{cases} \mathcal{B}_0(x) = 1, \\ \mathcal{B}_1(x) = x - \frac{1}{2}, \\ \mathcal{B}_2(x) = x^2 - x + \frac{1}{6}, \\ \mathcal{B}_3(x) = x^3 - \frac{3}{2}x^2 + \frac{1}{2}x, \\ \mathcal{B}_4(x) = x^4 - 2x^3 + x^2 - \frac{1}{30}. \end{cases} \tag{A.25}$$

Let us multiply the left- and right-hand sides of Eq. (A.24) with dz/z^{p+1} performing integration with the Hankel contour η as follows:

$$\int_\eta \frac{dz}{z^p}\frac{e^{xz}}{e^z-1} = \sum_{\ell\neq p}^{\infty}\frac{\mathcal{B}_\ell(x)}{\ell!}\int_\eta dz\ z^{\ell-p-1} + \frac{\mathcal{B}_p(x)}{p!}\int_\eta \frac{dz}{z}. \tag{A.26}$$

In Eq. (A.26), the integrations along positive real axis cancel each other, and the remaining integration is around circle with radius δ at the origin. Thus, Eq. (A.26) becomes

$$\int_\eta \frac{dz}{z^p}\frac{e^{xz}}{e^z-1} = i\sum_{\ell\neq p}^{\infty}\delta^{\ell-p}\mathcal{B}_\ell(x)\int_0^{2\pi} d\theta\ e^{i(\ell-p)\theta} + i\frac{\mathcal{B}_p(x)}{p!}\int_0^{2\pi} d\theta. \tag{A.27}$$

It is noted that the first term on the right-hand side of Eq. (A.27) vanishes. By changing $p \to p+1$, and by using the result in Eq. (A.23), we get

$$-I(-p,x) = 2\pi i\frac{\mathcal{B}_{p+1}(x)}{(p+1)!}. \tag{A.28}$$

Finally, by substituting Eq. (A.22) to Eq. (A.28), we derive the relation between the Hurwitz zeta function and the Bernoulli polynomial as follows:

$$\zeta(-p,x) = -\frac{\mathcal{B}_{p+1}(x)}{(p+1)}. \tag{A.29}$$

In particular, for $x = 1$, we obtain the relation between the Riemann zeta function and the Bernoulli number $\mathcal{B}_\ell \equiv \mathcal{B}_\ell(1)$ [it is noted that for $\ell > 1$, $\mathcal{B}_\ell(1) = \mathcal{B}_\ell(0)$]. Therefore, infinite summations of positive powers of integers can be regularized by the zeta function. For instances, the summations $1+1+1+...$ and $1+2+3+...$ are given by $\zeta(0) = -1/2$ and $\zeta(-1) = -1/12$, respectively. These results have been applied to derive thermodynamic potentials of massive Dirac fermions in Chapter 5.

A.3 Numerical calculation of zeta function

In the calculation of the de Haas-van Alphen effect in Chapter 5, finite summations of positive numbers are expressed as the difference of two zeta functions. For example, consider the summation

$$S(p,q,N) \equiv \sum_{n=0}^{N}(n+q)^{-p} \tag{A.30}$$

for $q \neq 0,\ -1,\ -2, ...$, etc. The right-hand side of Eq. (A.30) can be expressed in term of subtraction of two Hurwitz zeta functions as follows:

$$\begin{aligned}\sum_{n=0}^{N}(n+q)^{-p} &= \sum_{n=0}^{\infty}(n+q)^{-p} - \sum_{n=N+1}^{\infty}(n+q)^{-p} \\ &= \zeta(p,q) - \zeta(p,q+N+1) \\ &\equiv Z(p,q,N).\end{aligned} \tag{A.31}$$

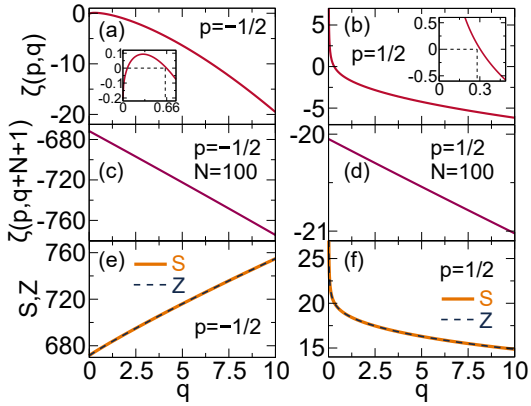

Figure A.2 Plot of $\zeta(p,q)$ with $q = 1-10$ for (a) $p = -1/2$, (b) $p = 1/2$. In the insets of (a) and (b) we show that the values of $\zeta(p,q)$ for $p = -1/2$ and $p = 1/2$ are negative for $q > 0.66$ and $q > 0.3$, respectively. Plot of $\zeta(p, q+N+1)$ with $N = 100$ for (c) $p = -1/2$, (d) $p = 1/2$.Comparison between the functions $S(p,q,N)$ and $Z(p,q,N)$ for (e) $p = -1/2$ and (f) $p = 1/2$.

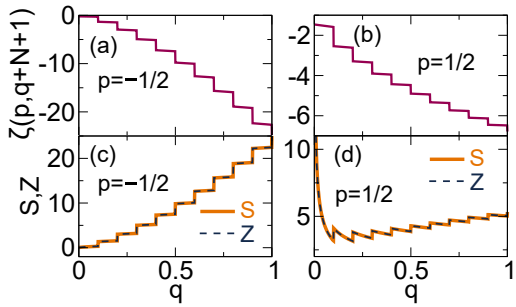

Figure A.3 Plot of $\zeta(p, q+N+1)$ with $N = 10\lfloor q \rfloor$ for (a) $p = -1/2$, (b) $p = 1/2$. The comparison between the functions $S(p,q,N)$ and $Z(p,q,N)$ for (c) $p = -1/2$ and (d) $p = 1/2$.

Thus, it should be confirmed that numerical calculation of $S(p,q,N)$ reproduces the analytical calculation of $Z(p,q,N)$. In Fig. A.2 (a) and (b), we plot the zeta function $\zeta(p,q)$ for $p = -1/2$ and $p = 1/2$, respectively. The value of $\zeta(-1/2,q)$ is negative and deceases monotonically for $q > 0.66$ as shown in the inset in (a). The value of $\zeta(1/2,q)$ diverges at $q = 0$ and change signs at $q \approx 0.3$. In (c) and (d), we substitute q to $q+N+1$ and take $N = 100$ for explaining the change of $\zeta(p,q) - \zeta(p,q+N+1)$. In (e) and (f) we compare the functions $S(p,q,N)$ and $Z(p,q,N)$. It is observed that the two functions exactly identical for $q = 0$ to 10.

It is noted that both the functions S and Z are continuous and do not explain the oscillatory behaviour of the thermodynamic potential in the dHvA effect. By changing the constant N to $10\lfloor q \rfloor$ for an example, the function $\zeta(p, q+N+1)$ shows step-like

Fig. A.2: fig/app/fig:Hurwitzf.eps
Fig. A.3: fig/app/fig:Hurwitzf2.eps

behaviour as shown in Fig. A.3(a) and (b) because of the nature of the function $\lfloor q \rfloor$. In (c) and (d), we compare the functions $S(p, q, N)$ and $Z(p, q, N)$ for $p = -1/2$ and $p = 1/2$, respectively. As in the previous case, the two functions match each other. Therefore, the analytical expressions of the thermodynamic potentials for doped a Dirac fermion is numerically verified.

Appendix B

Thermodynamic potential for hole-doped Dirac fermions

In the case of hole-doped system, we redefine ν_ξ as the highest unoccupied LLs in the valence bands, and we define $\Omega_-^{(h)}$ as potential from the unoccupied LLs. With the same procedure to derive $\Omega_+^{(e)}$, and by using $\epsilon_n^\xi = \xi\lambda/2 - \hbar\omega_c\sqrt{|n| + {\Gamma_\xi}^2}$ for $n \leqslant 0$, $\Omega_-^{(h)}$ is given as follows:

$$\begin{aligned}\Omega_-^{(h)} = \frac{2eB}{h}\sum_{\xi=\pm}\Bigg[&\frac{\Delta}{4} + |\mu|\Big(\nu_\xi + \frac{1}{2}\Big) + \frac{\xi\lambda}{2}\nu_\xi \\ &+ \hbar\omega_c\Bigg\{\zeta\Big(-\frac{1}{2}, {\Gamma_\xi}^2 + \nu_\xi + 1\Big) - \zeta\Big(-\frac{1}{2}, {\Gamma_\xi}^2\Big)\Bigg\}\Bigg] \\ &\times \Theta(|\mu| - \Delta_\xi/2).\end{aligned} \tag{B.1}$$

The total thermodynamic potential is given by $\Omega = \Omega_- - \Omega_-^{(h)}$. It is noted that the electron- and hole-doped Dirac systems give identical thermodynamic potentials in the case of $\lambda = 0$, because of the electron-hole symmetry.

It is noted that we should consider the spin magnetization for the hole-doping case when the chemical potential is located between $n = 0$ LLs for up- and down-spins, i.e. $-\Delta/2 - \lambda < \mu < -\Delta/2 + \lambda$. For example, in the case of Fig. 3.1(e) and (f), -0.905 eV $< \mu < -0.755$ eV. Here, the number of the spin-down electrons is larger than that of the spin-up electrons because of the occupancy of spin-down electrons in $n = 0$ LL at the K valley. The difference of the number of spin-up and spin-down electrons is one per degeneracy of the LL (eB/h). This means that the magnitude of induced spin magnetization is given by $|M_{\rm spin}| = (eB/h)\mu_B$, where $\mu_B = 9.274 \times 10^{-24}$ J/T is the Bohr magneton. Therefore, $M_{\rm spin}$ is proportional to B, which is similar to the conventional Zeeman effect. Nevertheless, the proportionality of B in the Zeeman effect comes from the energy splitting $g\mu_B B$ ($g \approx 2$ is the g-factor). The calculated value of $|M_{\rm spin}|$ for $B = 1$ T is 2.24×10^{-9} A, which is comparable to the orbital magnetization in MoS_2, $M \approx -6 \times 10^{-9}$ A (see Fig. 5.6). For such hole-doping, the slope of the magnetization as a function of B is modified from the orbital magnetization.

Appendix C

Calculation programs

The following programs are used to plot analytical results which are derived in Chapter 4 and 5. Here, we give brief descriptions for the programs, which are located in FLEX work station.

Faraday and Kerr rotations in Haldane model

This Fortran program calculates the optical conductivities of the Haldane model, the Faraday and the Kerr rotations, and other related quantities such as absorption probability. All input variables are defined in Chapters 2 and 4. An example of inputs and outputs of the program is given as follows:

Program location:

`~pratama/for/research/haldane_vc.f90`

Inputs:

1. `eF`

   The Fermi energy ϵ_F in the unit of eV.

2. `M,`

   On-site energy difference M in the unit of eV.

3. `t2,`

   Strength of next-nearest-neighbour hopping integral t_2 in the unit of eV.

4. `phi1, phi2`

   Phase angles ϕ of electron at the K and the K' valleys, respectively.

5. `psi`

   Angle of incidence for light ψ.

6. `epsiloni`

   Relative permittivity of medium for incident light ε_i.

7. `epsilont`
   Relative permittivity of medium for transmitted light ε_t.
8. `xii`
   The ration of s- to p- components of incident light ξ_i.
   Outputs:
9. `Ksxx.dat`
   Longitudinal conductivity $\sigma_{xx}(\omega)$ in the unit of $e^2/(4\hbar)$.
10. `Ksxy.dat`
    The Hall conductivity $\sigma_{xy}(\omega)$ in the unit of $e^2/(4\hbar)$.
11. `thetaK.dat`
    Angle of the Faraday rotation $\theta_F(\omega)$ in the unit of degree.
12. `thetaF.dat`
    Angle of the Kerr rotation $\theta_K(\omega)$ in the unit of degree.
13. `Absorb.dat`
    Absorption probability $A(\omega)$.

Magnetization and de Haas-van Alphen oscillation in 2D Dirac fermions

The following Python programs calculate thermodynamic potentials and magnetizations of the Dirac fermions. All input variables are defined in Chapters 3 and 5. An example of inputs and outputs of the program is given as follows:

`~pratama/for/research/landau3b.ipynb`

`~pratama/for/research/landau_tmd.ipynb`

Inputs:

1. `T`
   Temperature T in kelvin.
2. `D`
   Energy band gap Δ in joule.
3. `mu`
   Chemical potential μ in joule.
   Output:
4. `M.dat`
   Magnetization $M(B)$ in the unit of A/m.

Appendix D

Presentation

Publication list

Papers related to this thesis

1. **F. R. Pratama**, M. S. Ukhtary, and R. Saito, Circular dichroism and Faraday and Kerr rotation in two-dimensional materials with intrinsic Hall conductivities, Phys. Rev. B 101, 045426 (2020).

2. **F. R. Pratama**, M. S. Ukhtary, and R. Saito, Magnetizations and de Haas-van Alphen oscillations in massive Dirac fermions, Phys. Rev. B 103, 245408 (2021).

Other papers

1. **F. R. Pratama**, M. S. Ukhtary, and R. Saito, Non-vertical optical transition in near-field enhanced spectroscopy of graphene, J. Phys.: Condens. Matter 31, 265701 (2019) (during master course).

2. S. Wang, **F. R. Pratama**, M. S. Ukhtary, and R. Saito, Independent degrees of freedom in two-dimensional materials, Phys. Rev. B 101, 081414(R) (2020).

Conferences

Oral Presentations

1. **F. R. Pratama**, M. S. Ukhtary, and R. Saito: Simulation and principle of tip-enhanced Raman spectroscopy of graphene. Presented in ATI Zao-meeting, (August 9-10, 2017), Zao-Yamagata, Japan.

2. **F. R. Pratama**, M. S. Ukhtary, and R. Saito: Optical transition mechanism in tip-enhanced Raman spectroscopy of monolayer graphene. Presented in ATI Zao-meeting, (August 1-2, 2018), Zao-Yamagata, Japan.

3. **F. R. Pratama**, M. S. Ukhtary, and R. Saito: The Hall conductivity and circular dichroism. Presented in ATI Zao-meeting, (August 8-9, 2019), Zao-Yamagata, Japan.

Poster Presentations

1. **F. R. Pratama**, M. S. Ukhtary, and R. Saito: Near field electron-photon matrix element of monolayer graphene. Presented in The 54th Fullerenes-Nanotubes General Symposium (March 10-12, 2017), University of Tokyo, Tokyo, Japan.

2. **F. R. Pratama**, M. S. Ukhtary, and R. Saito: Near-field optical transition in graphene. Presented in The 55th Fullerenes-Nanotubes General Symposium (September 11-13, 2018), Tohoku University, Sendai, Japan.

3. **F. R. Pratama**, M.S. Ukhtary, and R. Saito: Optical conductivity of the Haldane model on honeycomb lattice. Presented in The 56th Fullerenes-Nanotubes General Symposium (March 2-4, 2019), University of Tokyo, Tokyo, Japan.

4. **F. R. Pratama**, M.S. Ukhtary, and R. Saito: Optical absorption in the two-dimensional hexagonal materials. Presented in The NT19 (July 21-26, 2019), University of Würzburg, Würzburg, Germany.

5. **F. R. Pratama**, M. S. Ukhtary, and R. Saito: Role of the Hall conductivity in the optical absorption of circularly polarized light. Presented in The 57th Fullerenes-Nanotubes General Symposium (September 3-5, 2019), Nagoya University, Nagoya, Japan.

6. **F. R. Pratama**, M. S. Ukhtary, and R. Saito: Magnetizations and De Haas-van Alphen oscillations in the Dirac fermions. Presented in The 60th Fullerenes-Nanotubes General Symposium (March 1-3, 2021), University of Tokyo, Tokyo, Japan (online).

7. **F. R. Pratama**, M.S. Ukhtary, and R. Saito: Magnetizations and de Haas van Alphen effects in Dirac fermions. Presented in The NT21 (July 6-12, 2021), Rice University, Houston, USA (online).

Bibliography

[1] V. S. Asadchy, M. S. Mirmoosa, A. Diaz-Rubio, S. Fan, and S. A. Tretyakov, Proc. IEEE **108**, 1684 (2020).

[2] E. Hecht, *Optics* (Pearson, Boston, 2017).

[3] P. N. Argyres, Phys. Rev. **97**, 334 (1955).

[4] H. S. Bennett and E. A. Stern, Phys. Rev. **137**, A448 (1965).

[5] J. L. Erskine and E. A. Stern, Phys. Rev. Lett. **30**, 1329 (1973).

[6] A. M. Shuvaev, G. V. Astakhov, A. Pimenov, C. Brüne, H. Buhmann, and L. W. Molenkamp, Phys. Rev. Lett. **106**, 107404 (2011).

[7] W.-K. Tse and A. H. MacDonald, Phys. Rev. Lett. **105**, 057401 (2010).

[8] K. N. Okada, Y. Takahashi, M. Mogi, R. Yoshimi, A. Tsukazaki, K. S. Takahashi, N. Ogawa, M. Kawasaki, and Y. Tokura, Nat. Commun. **7**, 1 (2016).

[9] R. Yu, W. Zhang, H. J. Zhang, S. C. Zhang, X. Dai, and Z. Fang, Science **329**, 61 (2010).

[10] C. X. Liu, S. C. Zhang, and X. L. Qi, Annu. Rev. Condens. Matter Phys. **7**, 301 (2016).

[11] C.-Z. Chang and M. Li, J. Phys.: Condens. Matter **28**, 123002 (2016).

[12] M. Nadeem, A. R. Hamilton, M. S. Fuhrer, and X. Wang, Small **16**, 1904322 (2020).

[13] K. von Klitzing, T. Chakraborty, P. Kim, V. Madhavan, X. Dai, J. McIver, Y. Tokura, L. Savary, D. Smirnova, A. M. Rey, and C. Felser, Nat. Rev. Phys. **2**, 397 (2020).

[14] R. Nandkishore and L. Levitov, Phys. Rev. Lett. **107**, 097402 (2011).

[15] G. Széchenyi, M. Vigh, A. Kormányos, and J. Cserti, J. Phys.: Condens. Matter **28** 375802 (2016).

[16] F. D. M. Haldane, Phys. Rev. Lett. **61**, 2015 (1988).

[17] S.-Q. Shen, *Topological Insulators* (Springer, Singapore, 2017).

[18] D. Vanderbilt, *Berry Phases in Electronic Structure Theory* (Cambridge University Press, Cambridge, 2018).

[19] N. R. Cooper, J. Dalibard, and I. B. Spielman, Rev. Mod. Phys **91**, 015005 (2019).

[20] M. D. Caio, N. R. Cooper, and M. J. Bhaseen, Phys. Rev. B **94**, 155104 (2016).

[21] Y. Ren, Z. Qiao, and Q. Niu, Rep. Prog. Phys. **79**, 066501 (2016).

[22] G. Jotzu, M. Messer, R. Desbuquois, M. Lebrat, T. Uehlinger, D. Greif, and T. Esslinger, Nature **515**, 237 (2014).

[23] H.-S. Kim and H.-Y. Kee, npj Quantum Mater. **2**, 1 (2017).

[24] J. W. McClure, Phys. Rev. **104**, 666 (1956).

[25] M. Sepioni, R. R. Nair, S. Rablen, J. Narayanan, F. Tuna, R. Winpenny, A. K. Geim, and I. V. Grigorieva, Phys. Rev. Lett., **105**, 207205 (2010).

[26] M. O. Goerbig, Rev. Mod. Phys. **83**, 1193 (2011).

[27] Y. Fuseya, M. Ogato, H. Fukuyama, J. Phys. Soc. Jpn. **84**, 012001 (2015).

[28] R. Saito and H. Kamimura, Phys. Rev. B **33**, 7218 (1986).

[29] A. Raoux, M. Morigi, J.-N. Fuchs, F. Piéchon, and G. Montambaux, Phys. Rev. Lett. **112**, 026402 (2014).

[30] A. Principi, M. Polini, and G. Vignale, Phys. Rev. B **80**, 075418 (2009).

[31] A. Principi and M. Polini, G. Vignale, and M. I. Katsnelson, Phys. Rev. Lett. **104**, 225503 (2010).

[32] H. Fukuyama, Y. Fuseya, M. Ogato, A. Kobayashi, and Y. Suzumura, Physica B **407**, 1943 (2012).

[33] M. Koshino and T. Ando, Phys. Rev. B **81**, 195431 (2010).

[34] M. Koshino and T. Ando, Solid State Commun. **151**, 1054 (2011).

[35] T. Cai, S. A. Yang, X. Li, F. Zhang, J. Shi, W. Yao, and Q. Niu, Phys. Rev. B **88**, 115140 (2013).

[36] M. Koshino and I. F. Hizbullah, Phys. Rev. B **93**, 045201 (2016).

[37] E. Elizalde, *Ten Physical Applications of Spectral Zeta Functions* (Springer, Heidelberg, 2012).

[38] H. B. Casimir, In Proc. Kon. Ned. Akad. Wet. **51**, 793 (1948).

[39] S. K. Lamoreaux, Phys. Rev. Lett. **78**, 5 (1997).

[40] H. B. Chan, Y. Bao, J. Zou, R. A. Cirelli, F. Klemens, W. M. Mansfield, and C. S. Pai, Phys. Rev. Lett., **101**, 030401 (2008).

[41] A. W. Rodriguez, F. Capasso, and S. G. Johnson, Nat. Photonics **5**, 211 (2011).

[42] A. Stange, D. K. Campbell, and D. J. Bishop, Phys. Today **74**, 42 (2021).

[43] O. Slezák, R. Yasuhara, A. Lucianetti, and T. Mocek, Opt. Mater. Express **6**, 3683 (2016).

[44] Y.-L. Li, T.-F. Li, Q.-Y. Wen, F. Fan, Q.-H. Yang, and S.-J. Chang, Opt. Express **28**, 21062 (2020).

[45] M. Fox, *Optical Properties of Solids* (Oxford University Press, New York, 2008).

[46] K. S. Novoselov, A. K. Geim, S. V. Morozov, D. Jiang, Y. Zhang, S. V. Dubonos, I. V. Grigorieva, and A. A. Firsov, Science **306**, 666 (2004).

[47] K. S. Novoselov, A. K. Geim, S. V. Morozov, D. Jiang, M. I. Katsnelson, I. V. Grigorieva, S. V. Dubonos, and A. A. Firsov, Nature **438**, 197 (2005).

[48] A. K. Geim and K. S. Novoselov, Nat. Mater. **6**, 183 (2007).

[49] A. H. Castro Neto, F. Guinea, N. M. R. Peres, K. S. Novoselov, and A. K. Geim, Rev. Mod. Phys. **81**, 109 (2009).

[50] K. S. Novoselov, V. I. Fal'ko, L. Colombo, P. R. Gellert, M. G. Schwab, and K. Kim, Nature **490**, 192 (2012).

[51] I. Crassee, J. Levallois, A. L. Walter, M. Ostler, A. Bostwick, E. Rotenberg, T. Seyller, D. van der Marel, and A. B. Kuzmenko, Nat. Phys. **7**, 48 (2011).

[52] R. Shimano, G. Yumoto, J. Y. Yoo, R. Matsunaga, S. Tanabe, H. Hibino, T. Morimoto, and H. Aoki, Nat. Commun. **4**, 1841 (2013).

[53] B. Huang, G. Clark, E. Navarro-Moratalla, D. R. Klein, R. Cheng, K. L. Seyler, D. Zhong, E. Schmidgall, M. A. McGuire, D. H. Cobden, W. Yao, D. Xiao, P. Jarillo-Herrero, and X. Xu, Nature **546**, 270 (2017).

[54] Y. Zhang, Y.-W. Tan, H. L. Stormer, and P. Kim, Nature **738**, 201 (2005).

[55] K. S. Novoselov, Z. Jiang, Y. Zhang, S. V. Morozov, H. L. Stormer, U. Zeitler, J. C. Maan, G. S. Boebinger, P. Kim, and A. K. Geim, Science, **315**, 1379 (2007).

[56] Z. Jiang, Y. Zhang, Y.-W. Tan, H. L. Stormer and P. Kim, Solid State Commun. **143**, 14 (2007).

[57] V. P. Gusynin and S. G. Sharapov, Phys. Rev. Lett. **95**, 146801 (2005).

[58] J. G. Checkelsky, L. Li, and N. P. Ong, Phys. Rev. Lett. **100**, 206801 (2008).

[59] J. Singleton, *Band Theory and Electronic Properties of Solids* (Oxford University Press, New York, 2014).

[60] K. von Klitzing, G. Dorda, and M. Pepper, Phys. Rev. Lett. **45**, 494 (1980).

[61] R. B. Laughlin, Phys. Rev. B, **23**, 5632 (1981).

[62] J. Weis and K. von Klitzing, Phil. T. R Soc. A **369**, 3954 (2011).

[63] K. von Klitzing, Annu. Rev. Condens. Matter Phys. **8**, 13 (2017).

[64] B. Jeckelmann and B. Jeanneret, Rep. Prog. Phys. **64**, 1603 (2001).

[65] N. Nagaosa, J. Sinova, S. Onoda, A. H. MacDonald, and N. P. Ong, Rev. Mod. Phys. **82** 1539 (2010).

[66] F. R. Pratama, M. S. Ukhtary, and R. Saito, Phys. Rev. B **101**, 045426 (2020).

[67] K. Ghalamkari, Y. Tatsumi, and R. Saito, J. Phys. Soc. Jpn. **87**, 063708 (2018).

[68] Y. Zhang, Z. Jiang, J. P. Small, M. S. Purewal, Y.-W. Tan, M. Fazlollahi, J. D. Chudow, J. A. Jaszczak, H. L. Stormer, and P. Kim, Phys. Rev. Lett. **96**, 136806 (2006).

[69] G. Li and E. Y. Andrei, Nat. Phys. **3**, 623 (2007).

[70] G. Li, A. Luican, and E. Y. Andrei, Phys. Rev. Lett. **102**, 176804 (2009).

[71] Z.-G. Chen, Z. Shi, W. Yang, X. Lu, Y. Lai, H. Yan, F. Wang, G. Zhang, and Z. Li, Nat. Commun. **5**, 4461 (2014).

[72] L.-J. Yin, S.-Y. Li, J.-B. Qiao, J.-C. Nie, and L. He, Phys. Rev. B **91**, 115405 (2015).

[73] J. Vallejo, N.J. Wu, C. Fermon, M. Pannetier-Lecoeur, T. Wakamura, K. Watanabe, T. Tanigushi, T. Pellegrin, A. Bernard, S. Daddinounou, V. Bouchiat, S. Guéron, M. Ferrier, G. Montambaux, and H. Bouchiat, arXiv:2012.05357 (2020).

[74] F. W. J. Olver, D. W. Lozier, R. F. Boisvert, and C. W. Clark (eds.), *NIST Handbook of Mathematical Functions* (Cambridge University Press, New York, 2010).

[75] L. Landau. Z. Phys. **64**, 629 (1930).

[76] B. Van Duppen and F. M. Peeters, Phys. Rev. B **88**, 245429 (2013).

[77] X.-Z. Yan and C. S. Ting, Phys. Rev. B **96**, 104403 (2017).

[78] Z. Li, L. Chen, S. Meng, L. Guo, J. Huang, Y. Liu, W. Wang, and X. Chen, Phys. Rev. B **91**, 094429 (2015).

[79] I. A. Luk'yanchuk and Y. Kopelevich, Phys. Rev. Lett. **93**, 166402 (2004).

[80] T. Champel and V. P. Mineev, Philos. Mag. B **81**, 55 (2001).

[81] K. Kishigi and Y. Hasegawa, Phys. Rev. B **65**, 205405 (2002).

[82] I. A. Luk'yanchuk, Low Temp. Phys. **37**, 45 (2011).

[83] A. R. Wright and R. H. McKenzie, Phys. Rev. B **87**, 085411 (2013).

[84] K. Kishigi and Y. Hasegawa, Phys. Rev. B **90**, 085427 (2014).

[85] I. M. Lifshitz and A. M. Kosevich, Zh. Eksp. Teor. Fiz. **29**, 730 (1955) [Sov. Phys. JETP **2**, 636 (1956)].

[86] L. Onsager, Phil. Mag. **43**, 1006 (1952).

[87] D. Cangemi and G. Dunne, Ann. Phys. (N.Y.) **249**, 582 (1996).

[88] A. Ghosal, P. Goswami, and S. Chakravarty. Phys. Rev. B **75**, 115123 (2007).

[89] S. Slizovskiy and J. J. Betouras. Phys. Rev. B **86**, 125440 (2012).

[90] H. Bruus and K. Flensberg, *Many-Body Quantum Theory in Condensed Matter Physics* (Oxford University Press, Oxford, 2016).

[91] R. A. Jishi, *Feynman Diagram Techniques in Condensed Matter Physics* (Cambridge University Press, Cambridge, 2014).

[92] L. A. Falkovsky and A. A. Varlamov, Eur. Phys. J. B **56** 281 (2007).

[93] M. Born and E. Wolf, *Principles of Optics* (Cambridge University Press, Cambridge, 2003).

[94] G.-B. Liu, W.-Y. Shan, Y. Yao, W. Yao, and D. Xiao, Phys. Rev. B. **88**, 085433 (2013).

[95] W.-K. Tse and A. H. MacDonald, Phys. Rev. B **84**, 205327 (2011).

[96] J. L. Lado and J. Fernández-Rossier, 2D Mater. **3**, 035023 (2016).

[97] C. J. Tabert and E. J. Nicol, Phys. Rev. Lett. **110**, 197402 (2013).

[98] F. Qu, A. C. Dias, J. Fu, L. Villegas-Lelovsky, and D. L. Azevedo, Sci. Rep. **7**, 41044 (2017).

[99] X. Li, F. Zhang and Q. Niu, Phys. Rev. Lett. **110**, 066803 (2013).

[100] D. Xiao, G.-B. Liu, W. Feng, X. Xu, and W. Yao, Phys. Rev. Lett. **108**, 196802 (2012).

[101] F. R. Pratama, M. S. Ukhtary, and R. Saito, Phys. Rev. B **103**, 245408 (2021).

[102] S. G. Sharapov, V. P. Gusynin, and H. Beck, Phys. Rev. B. **69**, 075104 (2004).

[103] M. Koshino and T. Ando, Phys. Rev. B. **75**, 235333 (2007).

[104] M. Nakamura, Phys. Rev. B. **76**, 113301 (2007).

[105] M. Nakamura and L. Hirasawa, Phys. Rev. B. **77**, 045429 (2008).

[106] C. J. Tabert, J. P. Carbotte, and E. J. Nicol, Phys. Rev. B. **91**, 035423 (2015).

[107] T. Stauber, N. M. R. Peres, and A. K. Geim, Phys. Rev. B **78**, 085432 (2008).

[108] M. S. Ukhtary, E. H. Hasdeo, A. R. T. Nugraha, and R. Saito, APEX **8**, 055102 (2012).

[109] Y. Harada, M. S. Ukhtary, M. Wang, S. K. Srinivasan, E. H. Hasdeo, A. R. T. Nugraha, G. T. Noe, II, Y. Sakai, R. Vajtai, P. M. Ajayan, R. Saito, and J. Kono, ACS Photonics **4**, 121 (2017).

[110] A. B. Khanikaev, N. Arju, Z. Fan, D. Purtseladze, F. Lu, J. Lee, P. Sarriugarte, M. Schnell, R. Hillenbrand, M. A. Belkin, G. Shvets, Nat. Commun. **7**, 12045 (2016).

[111] C.-C. Liu, W. Feng, and Y. Yao, Phys. Rev. Lett. **107**, 076802 (2011).

[112] C.-C. Liu, H. Jiang, and Y. Yao, Phys. Rev. B **84** 195430 (2011).

[113] M. Ezawa, Phys. Rev. B. **86**, 161407(R) (2012).

[114] M. Ezawa, Phys. Rev. Lett. **109**, 055502 (2012).

[115] C. L. Kane and E. J. Mele, Phys. Rev. Lett. **95**, 226801 (2005).

[116] A. R. Wright, Sci. Rep. **3**, 2736 (2013).

[117] K. F. Mak, K. He, J. Shan, and T. F. Heinz, Nat. Nanotechnol. **7**, 494 (2012).

[118] T. Cao, G. Wang, W. Han, H. Ye, C. Zhu, J. Shi, Q. Niu, P. Tan, E. Wang, B. Liu, and J. Feng, Nat. Commun. **3**, 887 (2012).

[119] Z. Li and J. P. Carbotte, Phys. Rev. B **86**, 205425 (2012).

[120] M. Ezawa, Eur. Phys. J. B **85**, 363 (2012).

[121] S. Y. Zhou, G.-H. Gweon, A. V. Fedorov, P. N. First, W. A. de Heer, D.-H. Lee, F. Guinea, A. H. Castro Neto, and A. Lanzara, Nat. Mater. **6** 770 (2007).

[122] F. Escudero, J. S. Ardenghi, and P. Jasen, J. Phys. Condens. Matter **31**, 285804 (2019).

[123] F. Escudero, J. S. Ardenghi, and P. Jasen, Eur. Phys. J. B **93**, 93 (2020).

[124] C. H. Yang, F. M. Peeters, and W. Xu, Phys. Rev. B **82** 075401 (2010).

[125] H. Funk, A. Knorr, F. Wendler, and E. Malic, Phys. Rev. B **92** 205428 (2015).

[126] O. O. Sobol, P. K. Pyatkovskiy, E. V. Gorbar, and V. P. Gusynin, Phys. Rev. B **94** 115409 (2016).

[127] J. Knolle and N. R. Cooper, Phys. Rev. Lett **115**, 146401 (2015).

[128] S. Becker and M. Zworski, Commun. Math. Phys. **367** 941 (2019).

[129] Y. Kubota, K. Watanabe, O. Tsuda, and T. Taniguchi, Science **17**, 932 (2007).

[130] K. K. Kim, A. Hsu, X. Jia, S. M. Kim, Y. Shi, M. Hofmann, D. Nezich, J. F. Rodriguez-Nieva, M. Dresselhaus, T. Palacios, and J. Kong, Nano Lett. **12**, 161 (2011).

[131] G. Cassabois, P. Valvin, and B. Gil, Nat. Photonics **10**, 262 (2016).